THREE - DIMENSIONAL GEOMETRIC NONLINEAR CONTACT STRESS ANALYSIS OF RIVETED JOINTS

Final Report

Submitted to

NASA Langley Research Center

Hampton, VA

NASA Grant No. NAG1-1754

September 18, 1995 through September 30,1998

By

Dr. Kunigal N. Shivakumar and Vivek Ramanujapuram

Center for Composite Materials Research

Department of Mechanical Engineering

North Carolina A & T State University

Greensboro, North Carolina

1998

TABLE OF CONTENTS

LIST OF FIGURES

Figure Page

LIST OF TABLES

1. INTRODUCTION

1.1 Introduction

The problems associated with fatigue were brought into the forefront of research by the explosive decompression and structural failure of the Aloha Airlines Flight 243 in 1988. The structural failure of this airplane has been attributed to debonding and multiple cracking along the longitudinal lap splice riveted joint in the fuselage. This crash created what may be termed as a minor "Structural Integrity Revolution" in the commercial transport industry. Major steps have been taken by the manufacturers, operators and authorities to improve the structural airworthiness of the aging fleet of airplanes. Notwithstanding this considerable effort there are still outstanding issues and concerns related to the formulation of Widespread Fatigue Damage which is believed to have been a contributing factor in the probable cause of the Aloha accident. The lesson from this accident was that Multiple-Site Damage (MSD) in "aging" aircraft can lead to extensive aircraft damage. A strong candidate in which MSD is highly probable to occur is the riveted lap joint.

1.2 Background

Riveted lap joints are used in an aircraft fuselage to join large skin sections. Among the many different types of joints, the single lap riveted joint is commonly used in aircraft construction. Joining introduces discontinuities (stress raisers) in the form of holes, changes in the load path due to lapping, and additional loads such as rivet bearing and bending moments. Because of these changes at the joint, local stresses are elevated in the structural component. Accurate estimations of these local stresses are needed to predict joint strength and fatigue life.

Exhaustive studies on stress-concentration factors (SCF's) for holes and notches in two-dimensional bodies subjected to a wide variety of loadings have been reported in the

literature [1, 2]. Studies have also been made on three-dimensional stress-concentrations at circular holes in plates subjected to remote tension loads [3-6]. A paper by Folias and Wang [6] provided a review of these previous solutions and presents a new series solution. The Folias and Wang solution covers a wide range of ratios of hole radius to plate thickness. The stress concentration at a hole in a plate subjected to bending was first presented by Neuber [4] using the Love-Kirchhoff thin plate theory [7]. Reissner [8] rederived the plate solution including the effect of shear deformation and showed that Neuber's solution was unconservative. Reissner's SCF solution for bending loads is presented in terms of the Bessel function. Naghdi [9] extended Reissner's analysis to elliptical holes using Mathieu's functions. Rubayi and Sosropartono [10] conducted 3-D photoelastic measurements to verify Reissner's circular hole and Naghdi's elliptical hole solutions. Other analytical solutions are given in references [11, 12]. Information on the fatigue behavior of riveted joints has been derived mainly from investigations associated directly or indirectly with aircraft. Experimental tests are usually performed on single lap or butt type joints, made with aluminum alloy plate and rivets, and loaded in repeated tension [13-15]. Results are reported in literature for remote loading, but very few papers considered [16, 17] 3-D effects for rivet loading in the hole.

A wealth of data on stress concentration at cut-outs in plates subjected to remote tension, remote bending, or simulated pin loading have been reported in the literature. Shivakumar and Newman conducted exhaustive 3-D finite element analysis of plates with holes and developed 3-D stress concentration solutions. Results were reported in the form of simple equations and a computer program [16]. The SCF along with the S-N diagram of the material may be adequate for designing riveted joints. This design is conservative, because a high factor of safety has to be used to account for the various unknowns.

With the advent of powerful computers, it became possible to explore this field by using the finite element method to simulate real situations. The work of Ekvall [18] is one

example. He developed a simple finite element model for the stress analysis of a joint to determine the local stress and strain at the fatigue critical location of a riveted lap or splice joint. Then, fatigue life predictions based on the local stress at the critical point were made using the effective stress-life law and the predicted fatigue and experimental lives were compared. In the simple finite element model he developed, the rivets were only modeled by three spring constants corresponding to the stiffness due to axial load, a shear load and bending moment applied to the rivet. The contact between the rivet and the plates was ignored.

A numerical and experimental fatigue analysis of cold worked holes with clearance fit and interference fit fasteners was made by Rich and Impellizzeri [19]. the equivalent strain amplitudes were computed from an equation developed by the authors and then entered on a strain amplitude-life plot of constant-amplitude data from smooth specimens and a fatigue life determined. The total life predictions were in reasonable agreement with the test data. However, both the analytical model and the test specimen simulating a fighter aircraft wing skin, where it would attached to a spar cap, were designed as a single piece and the load transfer through fasteners was ignored. Swenson et al. [20] developed a finite element model to simulate crack growth in the spanwise lap joints of an aircraft wing, where the primary loading is parallel to the joint. In their model, each layer of the riveted joint was represented by a separate 2-D finite element mesh and the layers were connected by rivet elements which were modeled as springs. It was found that the predicted crack growth rate was much higher than the test data at the start of the crack growth, although the predicted crack growth rate approached the experimental result as
the crack length approached half the joint overlap.

One major unknown is the load transfer mechanism at the joint. The load transfer mechanism is much more complex than the simple superposition of various loadings that can be used. Further more such a problem has not been solved. The complexities are

surface-to-surface contact between the rivet and the plates, the joint rotation due to non-axiality of loading and nonsymmetry of the configuration, and rivet clamp-up and interference. Because the problem is 3-D, the complexity is increased by one order of magnitude. Furthermore, the contact deformation is nonlinear, hence requires the solution of a variable BVP (boundary value problem). Analysis of riveted joints including these factors is important for the efficient design of joints, establishing the true factor of safety, and to verify the adequacy of the present design guidelines.

1.3 Total Fatigue Life Prediction Models

In the riveting process, a head on the protruding end of the shank is formed and the shank is deformed and expanded laterally to fill the rivet hole. In doing so it naturally grips the plate together. When such riveted joints are subjected to frequently repeated cyclical loads during service, the stress concentration effect may produce a fatigue crack and finally the riveted joints will fail from fatigue cracking even though the maximum applied stress is still within the range of the elastic behavior of the body.

There are two philosophically different approaches to predict the total life of a component. The difference in these methods lies in the definition of a crack. In approach one, the total life is defined as the sum of fatigue crack initiation life and crack propagation life. The second approach is called the small crack theory[21, 22]. This method assumes all materials have cracks either as a physical crack or as a defect. Defects causes cracks in the very first load cycle. So the crack is formed. Therefore, the total life is total number of load cycles required to make these micro-cracks to cause the fracture. The size of the micro-cracks is same as the material defect caused by material processing. Although the first approach has been used in the industry for a long time, the small crack theory is becoming attractive because the total could be predicted from computer models. The small crack theory requires a computed description of the stress field at critical locations. The

crack growth is calculated under those stress field. The micro-crack propagation is calculated under the influence of stress concentration. When the crack becomes one-tenth of a millimeter, the complete stress field will be used for crack propagation. Therefore, stress analysis of a joint including all joint complexities is critical to successful prediction of the total life of the joint using small crack theory.

1.4 Rivet Clampup and Interference

The riveting process consists of inserting the rivet in matching holes of the pieces to be joined and subsequently forming a head on the protruding end of the shank. the holes are generally 1/16 in. greater than the nominal diameter of undriven rivet. The head is formed by rapid forging with a pneumatic hammer or by continuous squeezing with a pressure riveter. The latter process is confined to use in shop practice, whereas pneumatic hammers are used in both shop and field riveting. In addition to forming the head, the diameter of the rivet is increased, resulting in a decreased hole clearance or the expansion of the hole (interference) [23].

Most rivets are installed as hot rivets, but some shop rivets are driven cold. Both processes introduces clampup force and interference to the joint.

During the riveting process the enclosed plies are drawn together with installation bolts and by the rivet equipment. As the rivet cools, it shrinks and squeezes the connected plies together. A residual clamping force or internal tension results in the rivet. The magnitude of the residual clamping force depends on the joint stiffness, critical installation conditions such as driving and finishing temperature, as well as driving pressure. Measurements have shown that hot driven rivets can develop clamping forces that approach the yield load of the rivet. Residual clamping forces are also observed in cold driven rivets. This results mainly from the elastic recovery of the gripped plies after the riveter, which squeezed the plies together during the riveting process, is removed. Generally, the clamping

force in cold-formed rivets is small when compared with the clamping force in similar hot-driven rivets. The clamping force in the rivet is difficult to control, however a range of clampup force as a percentage of the rivet yield load can be assumed for analysis.

The critical joint component in a lap joint subjected to repeated loading is not the fastener but the plate material. A severe decrease in the plate fatigue strength is apparent in unrestrained lap joints. The inherent bending deformations cause large stress ranges to occur at the discontinuities of the joint. The bending stress combines with the normal stress and results in high local stresses that reduce the fatigue strength of the lap joint.

1.5 Problem Definition

Two joint problems were considered; one is a classical pin joint (see Figure 1.1) to establish the basic solutions and the other is a two rivet single lap joint (see Figure 1.2). All the dimensions are in millimeters. The lap joint is an idealized version of a riveted panel tested by Hartman [24], see Figure 1.3. The total life of this panel was measured [24] and it was predicted by the small crack theory by Newman et al [21,22]. Newman used the results presented in this thesis for the prediction of the total life of the panel.

The pin joint configuration is almost the same as the lap joint, but the out-of-plane load eccentricity is eliminated. Therefore, effect of clampup, interference, and friction should be same as the lap joint.

The lap joint solutions should demonstrate the load eccentricity effects. A detailed finite element analysis of the joints are conducted and the results are presented in the thesis.

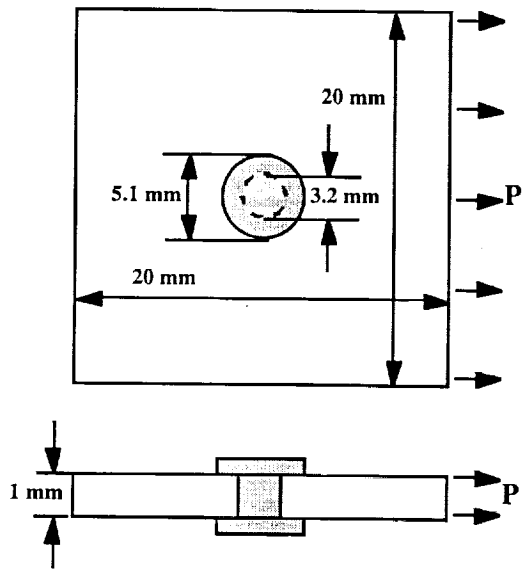

Figure 1.1. Pin joint.

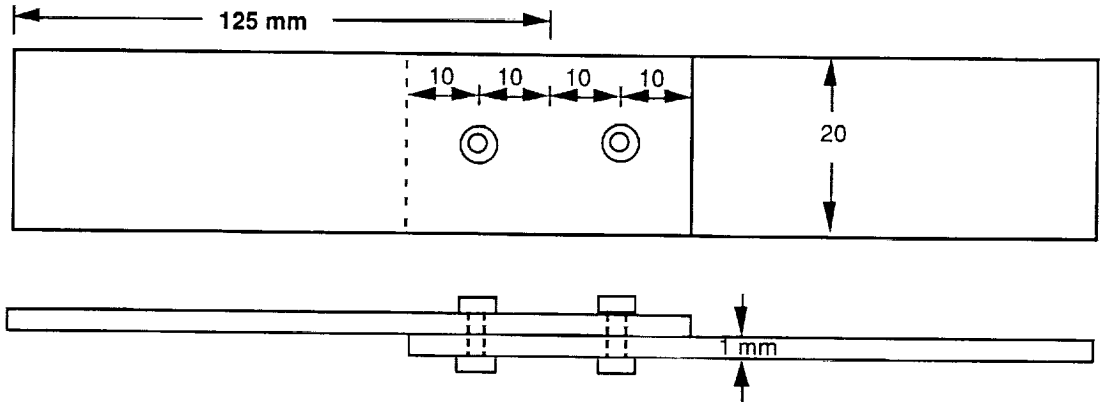

Figure 1.2. Two rivet single lap joint.

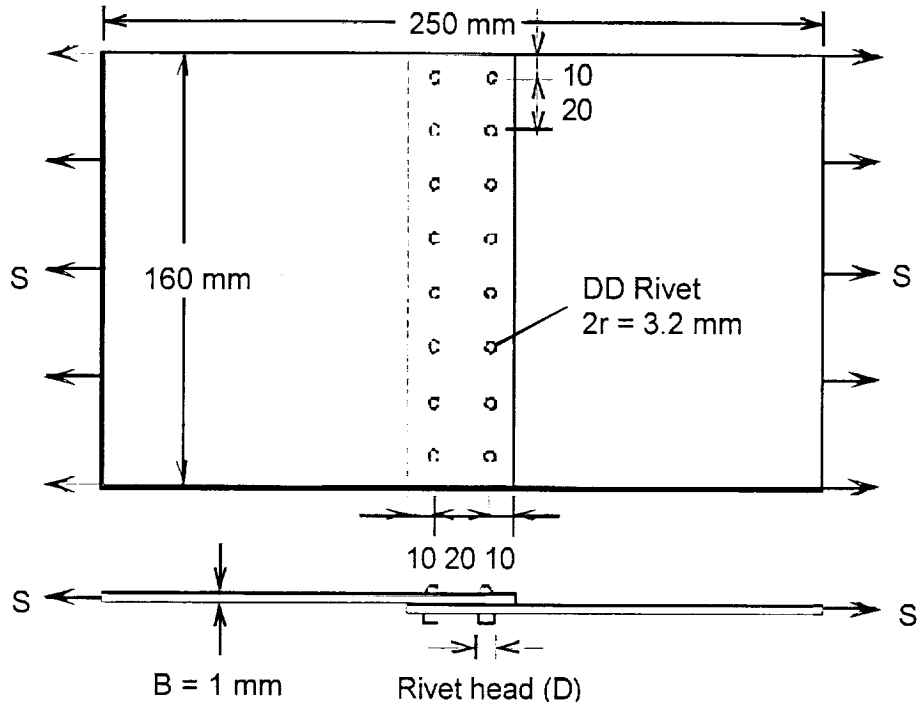

Figure 1.3. Experimental panel.

1.6 Objectives of the Research

Objectives of this research are as follows:

1. Conduct a detailed 3-D stress analysis of the pin joint and double row single lap rivet joint including nonlinear contact and large deformation.
2. Identify the regions of contact and high stresses, and then establish stress concentration factors.
3. Assess the effect of rivet clamp-up, rivet interference and friction on the local stress.

1.7 Scope

The report is presented in six sections. The first section presents introduction, background, definition of the problem and objectives of research. Section 2 presents the

description of finite element modeling of the two joints and modeling rivet clampup and interference effect. Also discussed in this section is the convergence criteria used for the non-linear analysis. Section 3 details the pin joint analysis for the neat fit, friction, clampup, interference and the combined case. The combined case is a combination of the rivet clampup, interference and friction. Section 4 covers the two rivet single lap joint analysis. In section 5 the neat fit case has been extended to elastic - plastic analysis to simulate a more realistic condition and the local stresses in the two rivet joint. Conclusions from the study are summarized in section 6..

2. FINITE ELEMENT MODELING OF RIVETED JOINT

2.1 Introduction

This section describes the finite element modeling of the rivet joint, contact, friction, clampup and interference. The general analysis procedure and convergence criteria are presented.

2.2 Finite Element Analysis

A stress analysis problem involves the differential equations of equilibrium and compatibility, together with the stress strain relationships and the boundary conditions. Analytical solutions to real life problems are seldom possible, and it is necessary, therefore, to employ a numerical method.

A number of numerical stress analysis techniques are currently available, and their implementation is being greatly facilitated by the increasingly widespread availability of computers. The essential common feature of these methods is that the original problem, posed in terms of differential equations in the unknown continuous functions, is replaced by a formulation involving a set of algebraic equations in the discrete values of the unknowns at a finite number of points in the solid. In other words, the continuum model of the problem is approximated by a discrete model having a finite number of degrees of freedom.

Of the numerical methods available the finite element method is the most widely used. The finite element method is a numerical procedure for obtaining solutions to many of the problems encountered in engineering analysis. It is impossible to document the exact origin of the finite element method because the basic concepts have evolved over a period of 150 or more years. The method as we know it today is an outgrowth of several papers published in the 1950s that extended the matrix analysis of structures to continuum bodies. The space exploration of the 1960s provided money for basic research, which placed the

method on a firm mathematical foundation and stimulated the development of multiple-purpose computer programs that implemented the method. The design of airplanes, missiles, space vehicles, and the like, provided application areas. Although the origin of the method is vague, its advantages are clear. The method is easily applied to irregular shaped objects composed of several different materials and having mixed boundary conditions. It is applicable to steady-state and time dependent problems as well as problems involving both geometric and material nonlinearity.

The finite element method combines several mathematical concepts to produce a system of linear or nonlinear equations. The number of equations is usually very large, running to several thousand depending on the problem that is being solved, and requires the computational power of the computer. The method has little practical value if modern computers are not available. The basis of the method is the representation of a structure by an assemblage of subdivisions or finite elements as shown in Figure 2.1. These finite elements are considered to be connected at joints, called nodes or nodal points, at which the values of the unknowns (usually the displacements) are to be approximated. Successive finer discretization of the structure would lead to the exact solution. Therefore, it is likely that a moderately fine subdivision will provide a solution of acceptable accuracy. The computational effort required to obtain a solution will depend upon the number of degrees of freedom in the finite element model. In engineering practice a limit will be imposed on the degree of subdivision of the structure by the need to strike a balance between computing costs and solution accuracy.

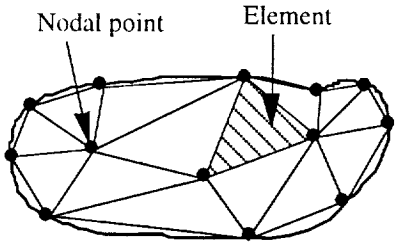

Figure 2.1. Representation of a two-dimensional solid as an assemblage of triangular finite elements.

Numerous commercial finite element analysis software packages are now available for simulating and solving complex engineering problems. One such code is ANSYS [25]. One of the advantage of ANSYS is its capability for geometric modeling and post-processing. Geometric modeling, analysis and results visualizations are all in the package. The analysis options include static, dynamic, material and geometric nonlinear analysis. In addition to having standard 1-D, 2-D, 3-D elements, it has line to line and surface to surface contact elements. These elements are needed for the present analysis of riveted joint.

2.3 Finite Element Modeling of Rivet Joint

The finite element model of the rivet joint (refer to Figure 1.1 and 1.2) consists of three main components namely the top plate, bottom plate and the rivet.

The plates and rivet are discretized using the SOLID45 3-D 8-Node Structural Solid element. The element is defined by 8 nodes having three degrees of freedom per node (translations in the nodal x, y, and z directions). The element may have any spatial orientation. The element has plasticity, stress stiffening, large deflection, and large strain capabilities. It can tolerate irregular shapes without much loss of accuracy. SOLID45 element has compatible displacement shapes and are well suited to model curved boundaries.

Contact occurs between the top plate and the bottom plate, the rivet and the plate holes, the rivet head and the plate. In the ANSYS program general contact is a boundary nonlinearity feature that permits surface-to-surface contact analysis with large deformations, contact and separation, coulomb friction sliding, and heat transfer. General contact is represented in the ANSYS program by following the position of points on one surface (the contact surface) relative to lines or areas of another surface (the target surface). The program uses contact elements to track the relative positions of the two surfaces. Contact elements are triangles, tetrahedron or pyramids, where the base is made up of nodes from the second surface (the target surface) and the remaining vertex is a node from the 1st surface, the contact surface. An analysis that incorporates general contact surfaces can easily require the use of hundreds or even thousands of contact elements. Fortunately, special features have been included in the ANSYS program to make generating and using these elements as efficient as possible. During solution, the program identifies those relatively few contact elements that are expected to affect the solution (i.e. those approaching contact or in contact). The remaining elements are temporarily ignored, producing null element stiffness matrices. As a result, an increase in the number of contact elements that are not in contact will not degrade run times as severely as would a similar increase involving other element types. The contact element used for the present problem is CONTAC49 3-D Point to Surface Contact.

2.3.1 CONTAC49 Element Description

CONTAC49 is a 5 node element that is intended for general contact analysis. In a general contact analysis, the area of contact between two or more bodies is generally not known in advance. In addition the finite element models of the contacting bodies are generated in such a way that precise node-to-node contact is neither achievable nor desirable when contact is established. The CONTAC49 element has the capability to represent

general contact of models that are generated with arbitrary meshes. In other words, its use is not limited to known contact or node-to-node configurations.

CONTAC49 is applicable to 3-D geometry. It may be applied to the contact of solid bodies or shells, to static or dynamic analyses, to problems with or without friction, and to flexible-to-flexible or rigid-to-flexible body contact.

Contact Kinematics

Contact kinematics is concerned with the precise tracking of contact nodes and surfaces in order to define clear and unambiguous contact conditions. The primary aim is to delineate between open (i.e., not in contact) and closed (in contact) contact situations. This task is accomplished by various algorithms embedded in the CONTAC49 element.

Contact and target definition

With reference to the Figure 2.2, two potential contact surfaces are referred to as either the "target surface" or the "contact surface". The target surface is represented by target nodes I, J, K and L, and the contact surface is represented by the contact node M. It is usually the case that many CONTAC49 elements will be needed to fully represent a realistic contact problem.

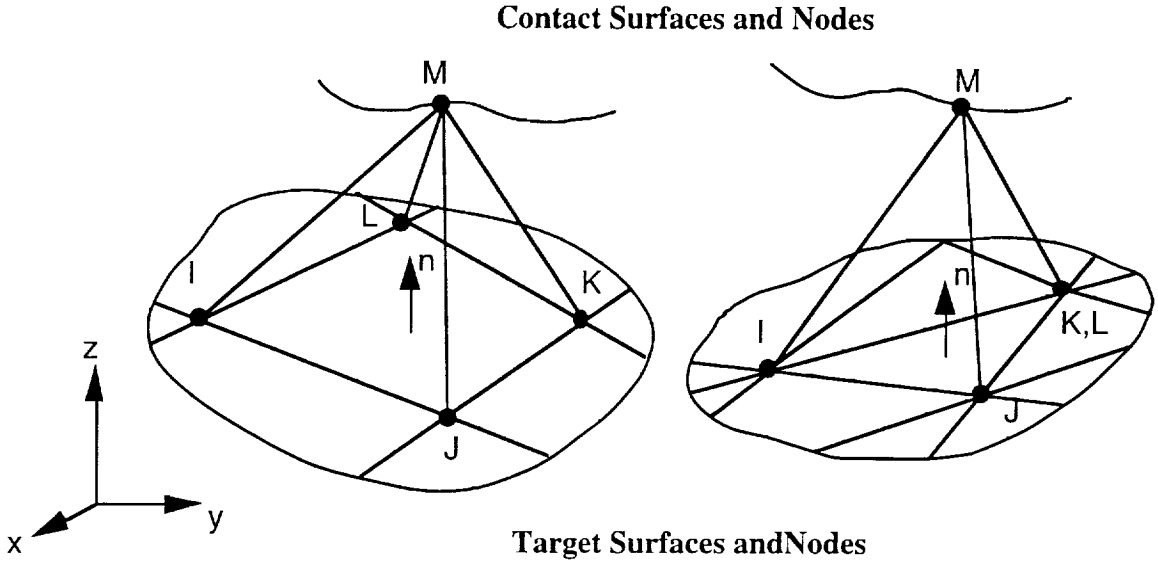

Figure 2.2. The CONTAC49 element configuration.

Pinball Algorithm

In simple terms, contact occurs whenever the contact node M penetrates the target surface (I, J, K, L). The first step in the determination of contact penetration is to make a distinction between near-field and far-field contact. Referring to 2-D transverse plane view for simplicity, (see Figure 2.3) shows several positions of a contact node with respect to the target surface. For CONTAC49 in 3-D the delimiting region is a sphere which is referred to as the "pinball". When a contact node is outside the pinball an open contact condition is assumed, irrespective of whether or not the contact node is above or below the target. penetration can only occur once the contact node is inside the pinball. The radius of the pinball is internally fixed to be 50% greater than the two target surface diagonals.

Pseudo Element Algorithm

The next step in the determination of contact is to associate a single target to each contact node depending upon the position of the contact node in space. This is accomplished by establishing solid "pseudo elements" for each target surface as shown in

Figure 2.4. A unique association is formed whenever contact node M is found within a target's pseudo element. If a clear distinction is not made it is possible that contact "voids" or "overlaps" can appear. These voids and overlaps are unavoidable and are due to piecewise discretization of surfaces that are actually curved. These solid elements are temporarily formed each equilibrium iteration and provide a continuous mapping for each contact node that is in or nearly in contact with a target. The kinematic information that is needed to build these pseudo elements is stored in a global contact data base that is updated each equilibrium iteration.

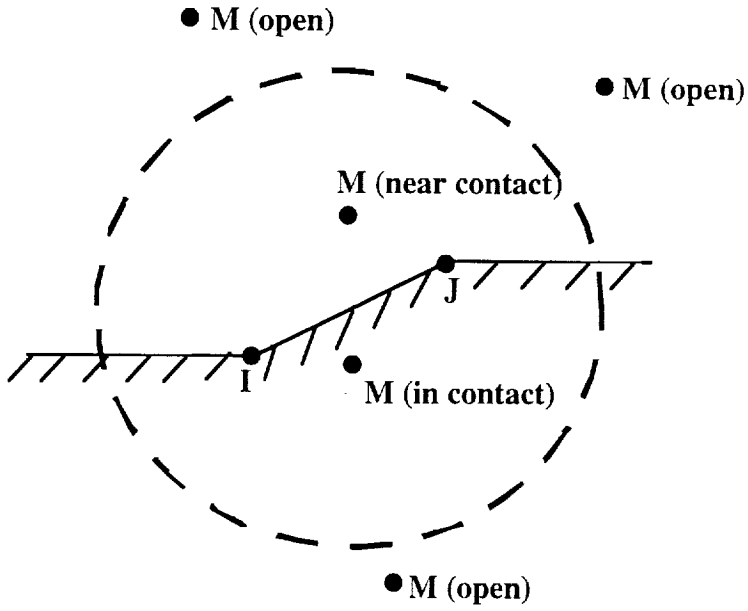

Figure 2.3. Definition of Near-Field and Far-Field Contact.

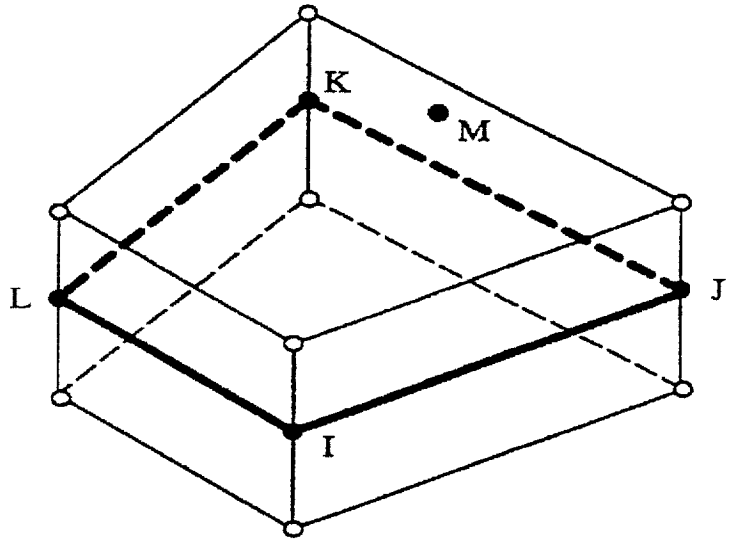

Figure 2.4. Pseudo Element.

Contact Gap And Projection

The pinball and pseudo-element algorithms provide a one-to-one mapping between a contact node and a target. The final kinematic step is to determine the open gap or the gap penetration of the contact node on the target plane, along with the point of projection of the contact node. This is achieved by first modifying the target surface nodes to lie in a plane if they do not already, simplifying tangential surface calculations. In other words the warping of the target surface is ignored. In Figure 2.5 several coordinate systems are indicated. The global system is the usual X-Y-Z system. The next system is the natural s-t-n system of the planar target surface. Another coordinate system x-y-z is constructed from the natural s-t-n system in such a way that n and z directions are parallel. This enables straightforward tracking of the tangential contact motions. Finally a second Cartesian x_e, y_e, z_e system is defined for the element. Having defined the modified (unwarped) target surface and the various coordinate systems, the contact kinematics of gap and location are left to be defined.

With reference to Figure 2.5, the contact location (s*, t*) is computed by Newton's iterative method based upon a normal projection of the contact node to the target plane. At the projected contact point a value of gap (g) is determined by the contact node's location with respect to the target plane. Contact penetration is assumed to occur if the value of g is found to be negative, and the s* and t* projections are found to be in the natural space bounds of the target. For the later condition, the target surface is internally expanded based on the tolerance specified, thereby increasing the chances that a contact node will come into contact with the target plane. A positive gap value indicates an open contact condition.

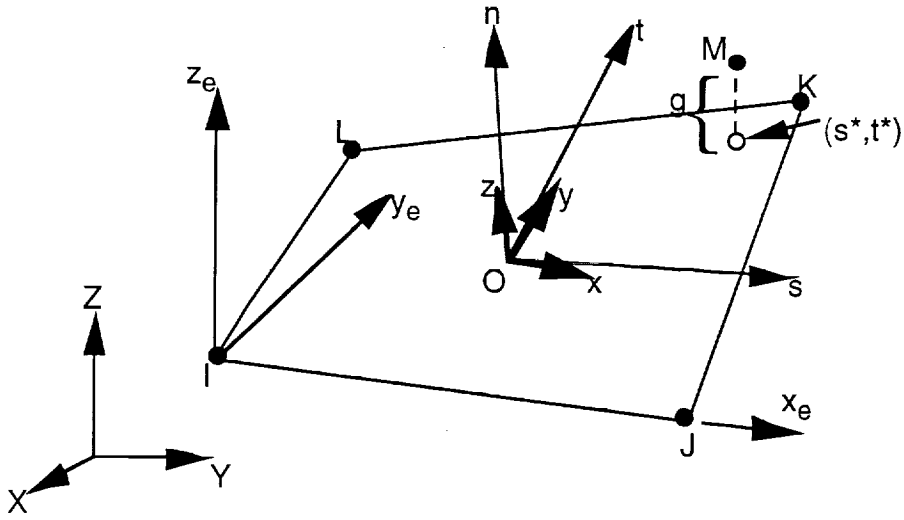

Figure 2.5. Target Co-ordinate Systems.

Contact Forces

As explained above, contact is indicated when the contact node M penetrates the target surface defined by target nodes I, J, K, and L. This penetration is represented by the magnitude of the gap (g) and is a violation of compatibility. In order to satisfy contact compatibility, forces are developed in a direction normal (n-direction) to the target that will tend to reduce the penetration to an acceptable numerical level. In addition to compatibility forces, friction forces are developed in directions that are tangent to the target plane. The

normal and tangential friction forces that are described here are referenced to the local x-y-z system shown in Figure 2.5.

Normal forces

Two methods of satisfying contact compatibility are available for CONTAC49: a penalty method and combined penalty plus lagrange multiplier method. The penalty method approximately enforces compatibility by means of a contact stiffness (i.e., the penalty parameter). The combined approach satisfies compatibility to a user defined precision by the generation of additional contact forces (i.e., Lagrange forces).

For the penalty method,

$$f_n = \begin{cases} K_n g & \text{if } g \le 0 \\ 0 & \text{if } g > 0 \end{cases}$$

where K_n is the contact stiffness (real constant KN).

For the combined method, the Lagrange multiplier component of force is computed locally (for each element) and iteratively. It is expressed as

$$f_n = \min (0, K_n g + \lambda_{i+1})$$

Where : λ_{i+1} = Lagrange multiplier force at iteration i + 1

$$= \begin{cases} \lambda_i + \alpha K_n g & \text{if } |g| \ge \varepsilon \\ \lambda_i & \text{if } |g| < \varepsilon \end{cases}$$

ε = user - defined compatibility tolerance (Input quantity TOLN on R command

α = an internally computed factor ($\alpha < 1$)

Friction forces

The CONTAC49 element considers three friction models: frictionless, elastic coulomb friction, and rigid coulomb friction. The Coulomb friction representations require

the input of the coefficient of sliding friction (μ). Friction causes the tangential forces, as the contact nodes meets and moves along the target surface.

For the frictionless case the tangential force is merely:

$$f_x = f_y = 0$$

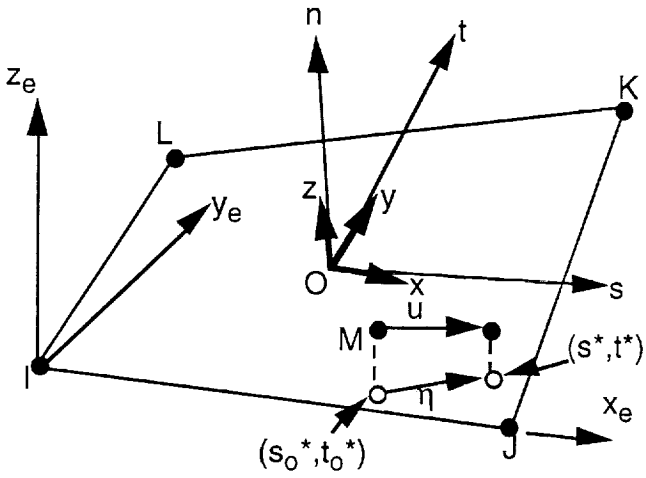

Figure 2.6. Location of contact node on the target plane.

For elastic Coulomb friction it is necessary to calculate the tangential deformation of the contact node relative to the target. Figure 2.6 shows the total motion (u) of the contact node M along the target plane. It is seen that the total tangential displacement (η) is represented by the projection of the total contact node motion to the unwarped plane of the target. Two projection points are mapped in the natural coordinates (s, t). The point (s*, t*) is the current projection position, and the tangential deformation is tracked from the point (s_o^*, t_o^*) that is associated with the previous converged solution (i.e., the previous time point). The deformation is first separated into x and y components, such that

$$\eta = \left(\eta_x^2 + \eta_y^2\right)^{1/2}$$

where: η_x = component of η in the local x direction

η_y = component of η in the local y direction

Next, the deformation is decomposed into elastic (or sticking) and sliding (or inelastic) components.

$$\eta_x = \eta_x^e + \eta_x^s$$
$$\eta_y = \eta_y^e + \eta_y^s$$

Related tangential forces are:

$$f_x = K_t \eta_x^e$$
$$f_y = K_t \eta_y^e$$

where: K_t = sticking stiffness

It follows that the magnitude of the tangential forces is

$$f_s = \left(f_x^2 + f_y^2\right)^{1/2}$$

The stiffness and the load vector for the CONTAC49 element is given below

$$\{N_n\}^T = [0\ 0\ q_1\ 0\ 0\ q_2\ 0\ 0\ q_3\ 0\ 0\ q_4\ 0\ 0\ 1]$$
$$\{N_x\}^T = [q_1\ 0\ 0\ q_2\ 0\ 0\ q_3\ 0\ 0\ q_4\ 0\ 0\ 1\ 0\ 0]$$
$$\{N_y\}^T = [0\ q_1\ 0\ 0\ q_2\ 0\ 0\ q_3\ 0\ 0\ q_4\ 0\ 0\ 1\ 0]$$

For the 4-node target, individual interpolates are

$$q_1 = -\frac{1}{4}(1-s^*)(1-t^*)$$
$$q_2 = -\frac{1}{4}(1+s^*)(1-t^*)$$
$$q_3 = -\frac{1}{4}(1+s^*)(1+t^*)$$
$$q_4 = -\frac{1}{4}(1-s^*)(1+t^*)$$

In the normal direction, the force applied to the contact node (M) is balanced by opposite forces applied to the target nodes; that is,

$$f_{n,M} = f_{n,I} + f_{n,J} + f_{n,K} + f_{n,L} = f_n$$

Similarly, in the tangential directions,

$$f_{x,M} = f_{x,I} + f_{x,J} + f_{x,K} + f_{x,L} = f_x$$
$$f_{y,M} = f_{y,I} + f_{y,J} + f_{y,K} + f_{y,L} = f_y$$

Using the interpolation vector above, the element load vector (i.e., the Newton-Raphson restoring forces) is:

$$\{F_I^{ne}\} = f_n\{N_n\} + f_x\{N_x\} + f_y\{N_y\}$$

and the stiffness matrix is given by

$$[K_I] = \begin{cases} K_n\{N_n\}\{N_n\}^T + K_s\{N_x\}\{N_x\}^T + \{N_y\}\{N_y\}^T & \text{if sticking contact} \\ K_n\{N_n\}\{N_n\}^T & \text{if sliding or frictionless contact} \\ [0] & \text{if open contact} \end{cases}$$

2.4 Modeling of Clampup

There are two ways of modeling the clampup of the rivet. One is to shrink the rivet by applying a differential temperature (cooling the rivet) to the rivet and giving it only an axial thermal coefficient of expansion/contraction. The other method is to make the rivet shank length (T_{rs}) smaller than the thickness (T_p) of the plate. The differential dimensions induces a clampup pressure by the rivet head (see Figure 2.7). Magnitude of clampup force depends on the value of (T_p - T_{rs}). Larger the value of (T_p - T_{rs}) larger the clampup force. A calibration study was conducted to obtain the relationship between the clampup force and the rivet shortening. For the current problem the second method was used because it offers

a better control over the axial force on the rivet. The practical range of clampup force varies between 10% to 35% of the rivet yield load.

Clampup Simulation ($T_{rs} < T_p$): Clampup force = 10% to 35% of yield load of the rivet

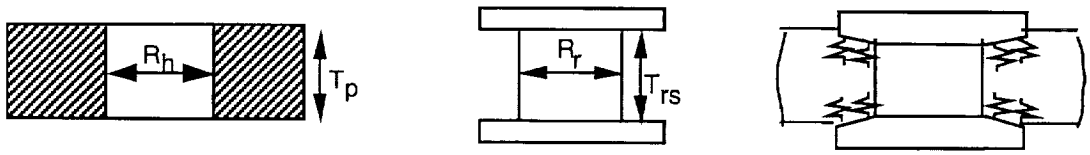

Figure 2.7. Schematic of the clampup procedure.

2.5 Modeling of Interference

The rivet interference was modeled using a larger diameter rivet to fit the joint. Figure 2.8 describes the mechanics of the modeling. The rivet hole diameter is R_h and the rivet diameter is R_r. When the rivet is inserted in the hole, the differential (R_r - R_h) introduces the interference stresses. If the value is negative, there is no interference. Magnitude of interference depends on the value of (R_r - R_h). Practical values of interference ranged from 0.00635 to 0.019 mm.

Interference Simulation ($R_h < R_r$): Interference (R_r-R_h) = 0.00635, 0.0127, 0.019 mm

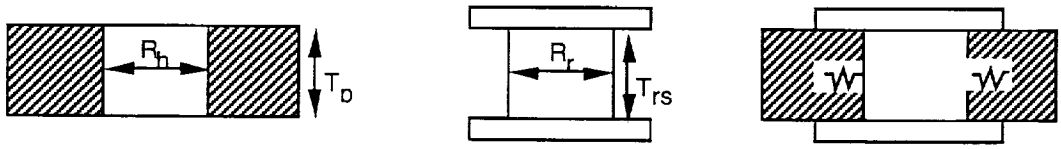

Figure 2.8. Schematic of the interference procedure.

2.6 Modeling of The Combined Case

The combined case was modeled by simultaneously making the rivet shank height less than the thickness of the plate and by making the rivet shank diameter to be larger than

the plate hole diameter.

2.7 Analysis Procedure

The commercial finite element code 'ANSYS' was used. The displacement method of analysis was used. The linear solution was obtained by the frontal solver. Before solution, ANSYS automatically reorders the elements for a smaller wavefront (smaller the wavefront less the CPU time required for solution). The nonlinear solutions are obtained from the Newton-Raphson iterative algorithm. The analysis was conducted by incrementing the displacement and calculating the equilibrium condition and the associated stress-strain field. The analysis was continued till desired stress state or the loading was attained.

2.8 Convergence Criteria

The force convergence criteria was used to solve the problem. This is the most efficient convergence criteria for nonlinear finite element problems. Since both nonlinear geometry and changing status elements were used in the model the convergence criteria was slackened to avoid convergence difficulties. The convergence criteria was arrived at in an iterative manner, slackening the convergence criteria whenever convergence problems were encountered.

The finite element discretization process yields a set of simultaneous equations:

$$[K]\{u\} = \{F^a\}$$

where:

$[K]$ = coefficient matrix

$\{u\}$ = vector of unknown degree of freedom values

$\{F^a\}$ = vector of applied loads

If the coefficient matrix is itself a function of the unknown DOF values (or their derivatives) then the above equation is nonlinear. The Newton-Raphson method is an iterative process of solving the nonlinear equations and can be written as:

$$\left[K_i^T\right]\{\Delta u_i\} = \left\{F^a\right\} - \left\{F_i^{nr}\right\}$$

where:

$\left[K_i^T\right]$ = Jacobian matrix (tangent matrix)

i = subscript representing the current equilibrium iteration

$\left\{F_i^{nr}\right\}$ = vector of restoring loads corresponding to the element internal loads.

$\left\{F^a\right\} - \left\{F_i^{nr}\right\}$ = residual or out of balance load vector.

In a structural analysis, $\left[K_i^T\right]$ is the tangent stiffness matrix, $\{u_i\}$ is the displacement vector and $\left\{F_i^{nr}\right\}$ is the restoring force vector calculated from element stresses.

The iteration process described continues until convergence is achieved. Convergence is assumed when:

$$\|\{R\}\| < \varepsilon_R R_{ref}$$

where $\{R\}$ is the residual vector:

$$\{R\} = \left\{F^a\right\} - \left\{F_i^{nr}\right\}$$

$\|\{R\}\| = \left(\sum R_i^2\right)^{\frac{1}{2}}$ (Euclidean norm)

ε_R = tolerance value

Convergence, therefore, is obtained when size of the residual (disequilibrium) is less than a tolerance times a reference value. The default out of balance reference value

R_{ref} is $\|F^a\|$.

2.9 Summary

With the advent of modern day computers and their ability to crunch numbers, finite element analysis has gained favor in the industry as an essential tool in their design process. ANSYS finite element code was used in this research project. The main reason being its capability to simulate contact between two bodies and its capability to do nonlinear analysis. Also a method of introducing rivet clampup and interference to the rivet joint was developed.

3. PIN JOINT ANALYSIS

3.1 Introduction

In this section a classical pin joint was modeled using 3-D finite elements. This joint is loaded by remote tension and is restrained by a pin. The effects of clampup and interference on the stress distribution in the hole boundary is presented in this section.

3.2 Joint Configuration

Figure 3.1 shows the geometry i.e. configuration of the pin joint. The plate was square with the edge being 20 mm and thickness being 2 mm. The hole was located in the center of the plate with a radius R_h of 1.6 mm. The pin head had a diameter ($d_h = 3.2R_h$)of 5.1 mm and thickness of 1.0 mm ($0.6R_h$). The radius to width and radius to edge distance is greater than 6, hence the joint configuration represents the infinite plate configuration. The global Cartesian coordinate system is represented by x, y, z. The pin is fixed at its center line and the plate is pulled by a uniform displacement u_o in the x direction. The pin bearing load (P) is the integral of x- directional reaction at the edge x = 10 mm. The geometry and the loading are symmetric about y = 0 and z = 0 planes. Hence, only one-quarter of the joint (shown by the shaded region) was modeled by finite elements.

3.3 Analysis Model

The joint symmetry was exploited to reduce computational time. Figure 3.2 shows the one - quarter geometry of the joint. The plate was loaded at x = 10 mm with a uniform displacement u_x and the axis of the pin was fixed in the x and y direction (that is $u_x = u_y = 0$ for the axis of the pin). The plate and the pin was modeled using 8-noded brick elements, SOLID45 in the ANSYS code. The 3-D surface to surface contact elements were used to simulate contact between the pin and the plate hole and pinhead and the plate surface. The

finite element model had 6912 SOLID45 elements (3456 elements each in plate and pin) and 1920 CONTAC49 elements. Figure 3.3 shows the finite element mesh.

The other boundary conditions imposed on the model were $u_y = 0$ on $y = 0$ plane and $u_z = 0$ on $z = 0$ plane. These two boundary conditions simulate symmetric deformation of the joint.

3.4 Analysis Cases

There are two types of non-linearities that are expected in the model, viz., nonlinear contact boundary and large rotation. Therefore, large deformation and non-linear contact strategies are used in the analysis. A commercial code ANSYS 5.3 was used. The non-linearities were solved by a modified Newton-Raphson iteration algorithm. The Lagrange multiplier and penalty methods are used for contact modeling. The defined maximum gap/penetrations and contact stiffnesses are 0.01Hs and 2000 N/mm^2 (about 3% of the elastic modulus of the plate material, which was within the recommended range) respectively. The parameter Hs is the smallest element size in the model, which was 1/6 mm. The residual force convergence criteria was used at every node to establish the convergence of the non-linear solution. The relative error in the nodal residual forces was less than 0.1% of total applied force as a convergence criteria.

The analysis was conducted for four different cases that occur in the joint: neatfit, clampup, friction and interference, and a selected combined case. The neatfit represents the baseline solution. This case represents no surface - surface friction, no clampup and no interference. Analytical modeling of each of these parameters are explained in section 2 and is summarized in the following sections. The analysis was conducted by incrementally loading the joint to an applied remote stress of about 150 MPa or about $U_o = 0.1$ mm.

3.4.1 Elastic Friction

Elastic friction values of 0.1, 0.2, 0.3 and 0.8 were chosen. The stress analysis was conducted for all four values. Interestingly, both location and magnitude of local stresses were unaltered. Hence, it was concluded that friction has no effect on local stresses.

3.4.2 Pin Clamp-up

As explained in the section 2.3 the pin clamp-up was introduced by changing the length of the pin shank. By shortening the pin's shank length compared to the thickness of the plate introduces clamp-up force in the joint. A separate stress analysis was conducted to establish a relation between clamp-up force and pin shortening. This relationship was found to be linear (refer to Figure 3.4). The clampup equation was given by

Clampup force, $F_c = 64{,}054 * \Delta L$

where ΔL is the rivet shortening ($T_{rs} - T_p$) in mm.

The amount of pin shortening for clamp-up force of 10%, 25%, 35% the pin yield force was calculated. These values were 7.64, 19.1 and 26.7 μm respectively. The analysis was repeated for all three values of pin shortening.

3.4.3 Pin Interference

Pin interference was introduced by increasing the radius of the pin (R_r) in relation to the hole radius (R_h). Three values of interference $2(R_r-R_h)$ were chosen, namely, 12.7, 25.4 and 38.1 μm. These values bound the real values experienced in the aircraft industry.

3.4.4 Combined Case

The combined case is a combination of rivet clampup, interference and friction between contacting surfaces acting simultaneously. For the combined case a clampup of 25% , an interference of 12.7 μm, and a coefficient of friction of 0.3 was used.

3.5 Results

Results of the analysis conducted for various cases are represented in the following subsections. First, neat fit (zero surface-surface friction) results are presented. Then the effects of clamp-up and interference on local stresses are examined. The primary focus was on the maximum hoop stress on the hole boundary and the hoop stress at 90° to the z-axis. The 2nd case represents location of maximum hoop stress for open hole problems. All local stresses are normalized by the remote stress (σ_∞) as much as possible. The remote stress was calculated by dividing the total reaction at x = 10 mm edge by the area of cross-section (10x1 mm^2).

3.5.1 Neat Fit Results

3.5.1.1 Deformed Shapes

Figure 3.5 show the global and local to pin deformed shapes of the joint at a load level of 156 MPa. As can be seen, the pin looses contact with the plate from $\theta = 0°$ to 90° and then it maintains contact and the hole is deformed into an elliptic shape.

3.5.1.2 Contact Non-linearity

The effect of contact non-linearity on local stresses was examined by analyzing the hoop stress at $\theta = 90°$ on the hole boundary of the plates. Figure 3.6 shows the variation of σ_θ with remote applied stress (σ_∞) at various values of 'z' at $\theta = 90°$. As can be seen σ_θ varies linearly with σ_∞. The same results are plotted as stress concentration factor (SCF = $\sigma_\theta / \sigma_\infty$) in Figure 3.7. The SCF is maximum for the bottom plate at Z = 0 (about 7.36) and lowest at z/t =0.5 (6.2) at the top surface of the plate.

Figure 3.8 shows a linear variation of membrane and bending stresses with σ_∞. Membrane stress is the average stress through the thickness and bending stress is half the difference between the top and bottom surfaces of the bottom plate at $\theta = 90°$. As can be seen the bending component is negligible compared to the membrane stress. The

membrane SCF was 6.78 and bending SCF was 0.57. Therefore, for a smooth fit rivet joint, the local stress field varies linearly with the applied remote stress.

3.5.1.3 Radial Stress Distribution at the Hole Boundary

Figures 3.9 and 3.10 shows the contact (radial) stress distribution on the hole boundary for remote applied stress of 29 and 156 MPa respectively. Radial stress is maximum at $\theta = 180^{\circ}$ for the plate. The radial stress can be approximated by cosine function as shown in Figure 3.11 (see thick solid curves). These cosine functions can be represented in the form of

$$\frac{\sigma_r}{\sigma_\infty} = a\cos^n \theta$$

Values of 'a' and 'n' for various levels are given by the following table.

Table 3.1 Values of '*a*' and '*n*' for various remote stresses

σ_∞, MPa	z/t	a	n
29	0.00	-9.40	0.88
	0.25	-7.40	0.87
60	0.00	-7.30	0.77
	0.25	-7.20	0.90
92	0.00	-6.80	0.83
	0.25	-7.70	1.00
124	0.00	-6.60	0.92
	0.25	-7.70	1.12
156	0.00	-7.20	1.02
	0.25	-8.10	1.19

The rivet contact angle is defined as the angle over which the radial compressive. This angle was found to be nearly 90° for $-3t/8<z<3t/8$. Note that contact stress is zero at $\theta = 90^{\circ}$ for most of the locations through the thickness. Results at $z = t_p/2$ (corner location) may not be accurate because they are being affected by rivet head contacts.

3.5.1.4 Hoop Stress Distribution

Figures 3.12 to 3.13 show the hoop stress distribution around the hole boundary for various remote loads. Hoop stress is compressive for $\theta < 30^{\circ}$ and tensile for $\theta > 30^{\circ}$. Hoop stress is maximum at $\theta = 90^{\circ}$, for all values of z. The major maximum σ_{θ} occurred at z = 0 (mid-plane). The maximum hoop stress occurs at $\theta = 90^{\circ}$ for all loads. Also the curves are almost invariant showing a linear relationship between the remote and local hoop stress.

3.5.1.5 Hoop Stress Contour Plots

Figure 3.14 shows the contours of hoop stress on z = 0 plane. As it was shown in Figures 3.12 and 3.13, the hoop stress is maximum at $\theta = 90^{\circ}$. The maximum hoop stress location is valid all through thickness of the plate, except at the outer surfaces of the plate.

3.5.2 Clampup Force

Stress analysis was conducted for three values of clampup force, namely, 10%, 25% and 35% of the yield load of the rivet. Both hoop and radial stresses on the hole boundaries were examined. The important findings are presented. Maximum hoop stress occurred at the hole boundary at $\theta = 90^{\circ}$.

Figure 3.15 shows the variation of the hoop stress at $\theta = 90^{\circ}$ and z = 0 mm on the hole boundary for various clampup forces. The Figure clearly demonstrates that the hoop stress at the hole boundary decreases with increase of clampup force. However the magnitude of decrease is not significant. It is of the order of 15, 30 and 45 MPa from the neatfit case for 10, 25, 35% clampup forces. Compared to the magnitude of local stresses, these values are not significant. Therefore, clampup effect can be ignored at high remote loads.

Figure 3.16 shows the variation of normalized hoop stress at $\theta = 90^{\circ}$ and z = 0 for neatfit and three values of clampup forces. At low remote stresses, clampup has very

pronounced effect, but at higher loads, the clampup effect is not significant. A similar conclusion can be derived for combined clampup and friction (see Figure 3.17).

3.5.3 Interference

Figure 3.18 shows variation of σ_θ at $\theta = 90^\circ$ and $z = 0$ with remote stress for three values of interference. The interference introduces high initial tensile stress on the hole boundary. Because of this the hoop stresses for interference cases is larger than neat fit case. With increase in remote stress, the local hoop stress increases at a slower rate than the neat fit case. Finally at higher loads rate of increase of hoop stress is same for both neat fit and interference cases. Therefore, interference results show two slopes with a transition region. The transition stress is unique for unique values of the interference.

3.5.4 Combined Case

Figure 3.19 shows a comparison of neat fit, 10% clampup, 25.4 mm interference and combined case hoop stress distribution. Combined case is 10% clampup, 25.4 μm interference and a surface to surface friction $\mu = 0.3$. The comparison show that the effect of friction and clampup is very small compared to the interference. Hence they can be neglected. The interference effect is large and it has to be properly accounted to predict fracture and/or life of a single rivet (pin) joint.

3.6 Summary

Conducted detailed 3-D stress analysis of single pin joint with friction, clampup, and interference. Practical ranges of clampup force (0 to 35 % of axial yield load of rivet) and interference (0 to 38.1 μm) were used in the parametric study. Results concluded that

(1) Maximum stress was the hoop stress on the hole boundary and occurred at 90° to the load axis. The hoop stress was maximum at mid-thickness of the plate.

(2) The contact angle was found to be nearly 180^0.

(3) Elastic friction had negligible effect on local stresses (hoop) and hence it can be ignored.

(4) Clampup effect was dominant at low applied loads. Clampup decreases the local hoop stresses. But at high applied loads, clampup effect is small.

(5) Interference was a major factor that impacted the local stresses (hoop stress) around the rivet hole. Interference introduces local tensile hoop stress at the rivet hole. This initial stress reduces the rate of increase of local stresses with remote loads. This causes the local hoop stresses to be lower than the neat fit results at high load levels.

(6) Contact, friction and rivet clampup nonlinearities were confined to low axial loads. At high loads, the response is nearly linear.

Table 3.1 Values of '*a*' and '*n*' for various remote stresses

σ_∞, MPa	z/t	a	n
29	0.00	-9.40	0.88
	0.25	-7.40	0.87
60	0.00	-7.30	0.77
	0.25	-7.20	0.90
92	0.00	-6.80	0.83
	0.25	-7.70	1.00
124	0.00	-6.60	0.92
	0.25	-7.70	1.12
156	0.00	-7.20	1.02
	0.25	-8.10	1.19

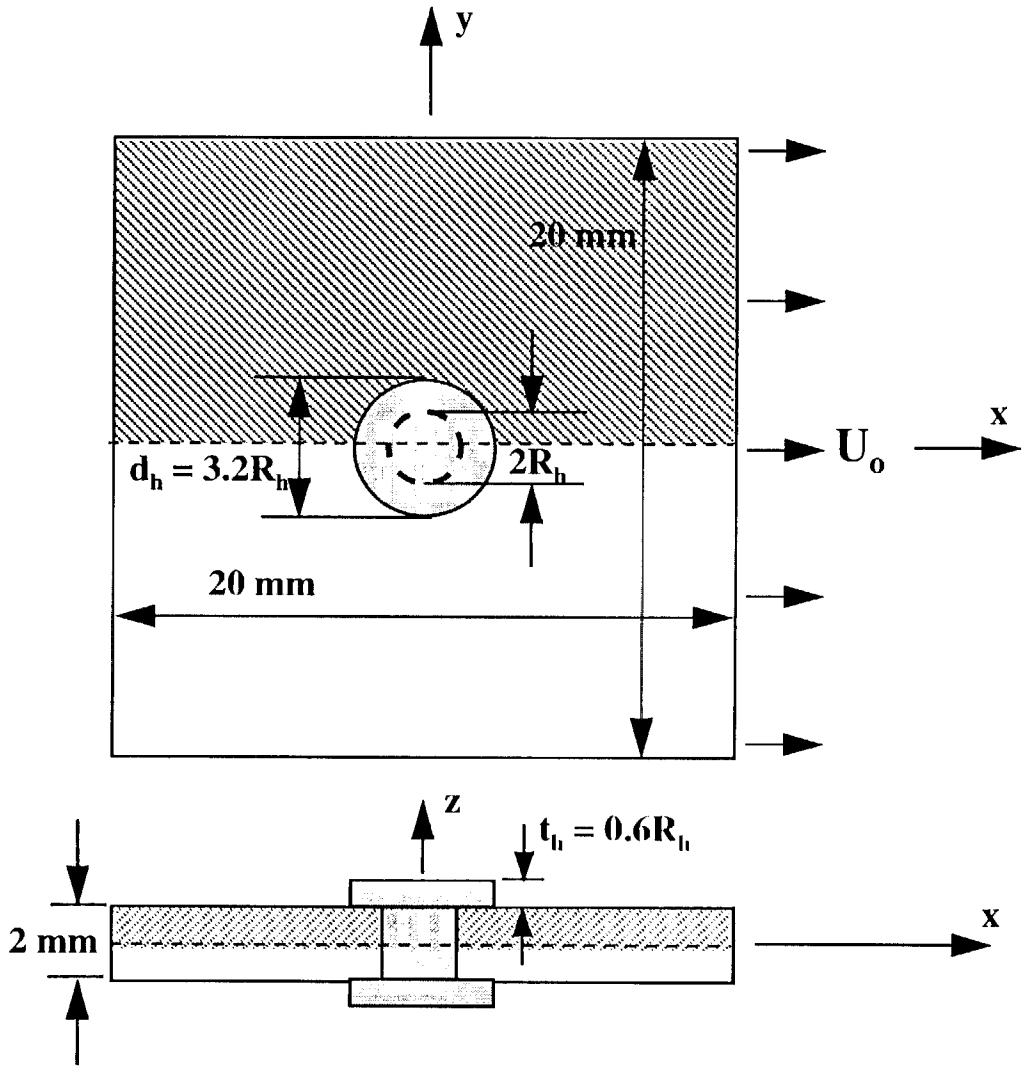

Figure 3.1. Joint configuration.

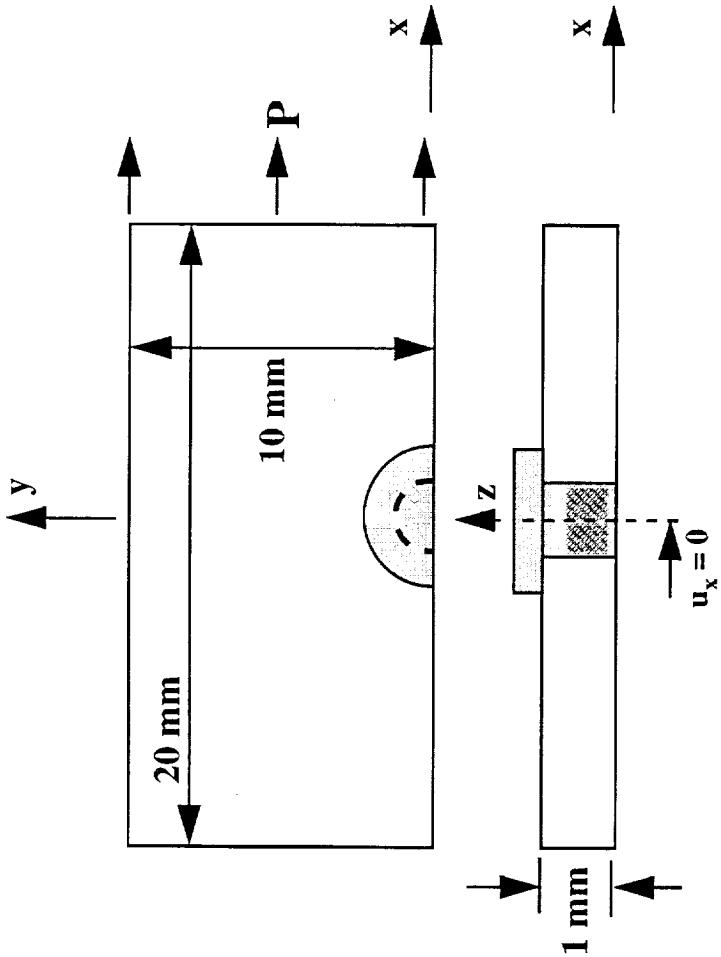

Figure 3.2. One - quarter of the joint model.

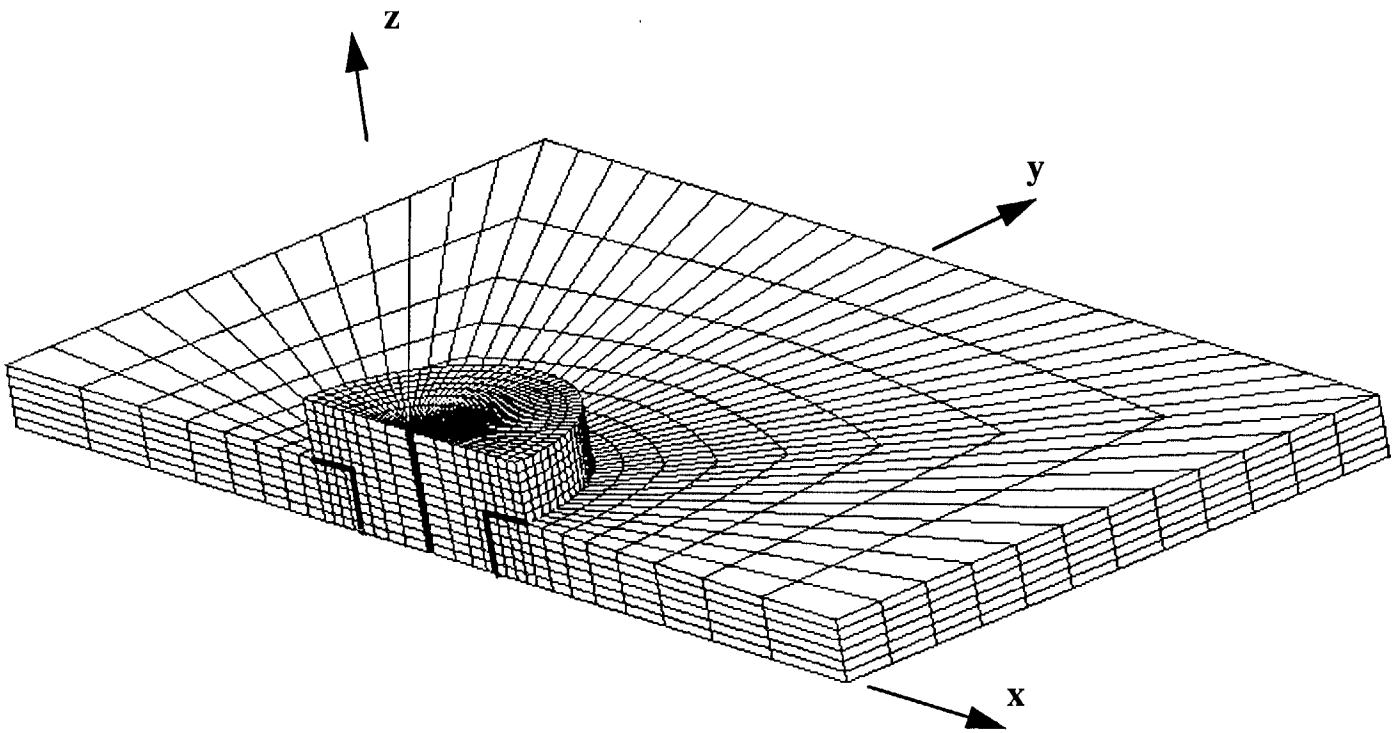

Figure 3.3. Finite element model of the pin joint.

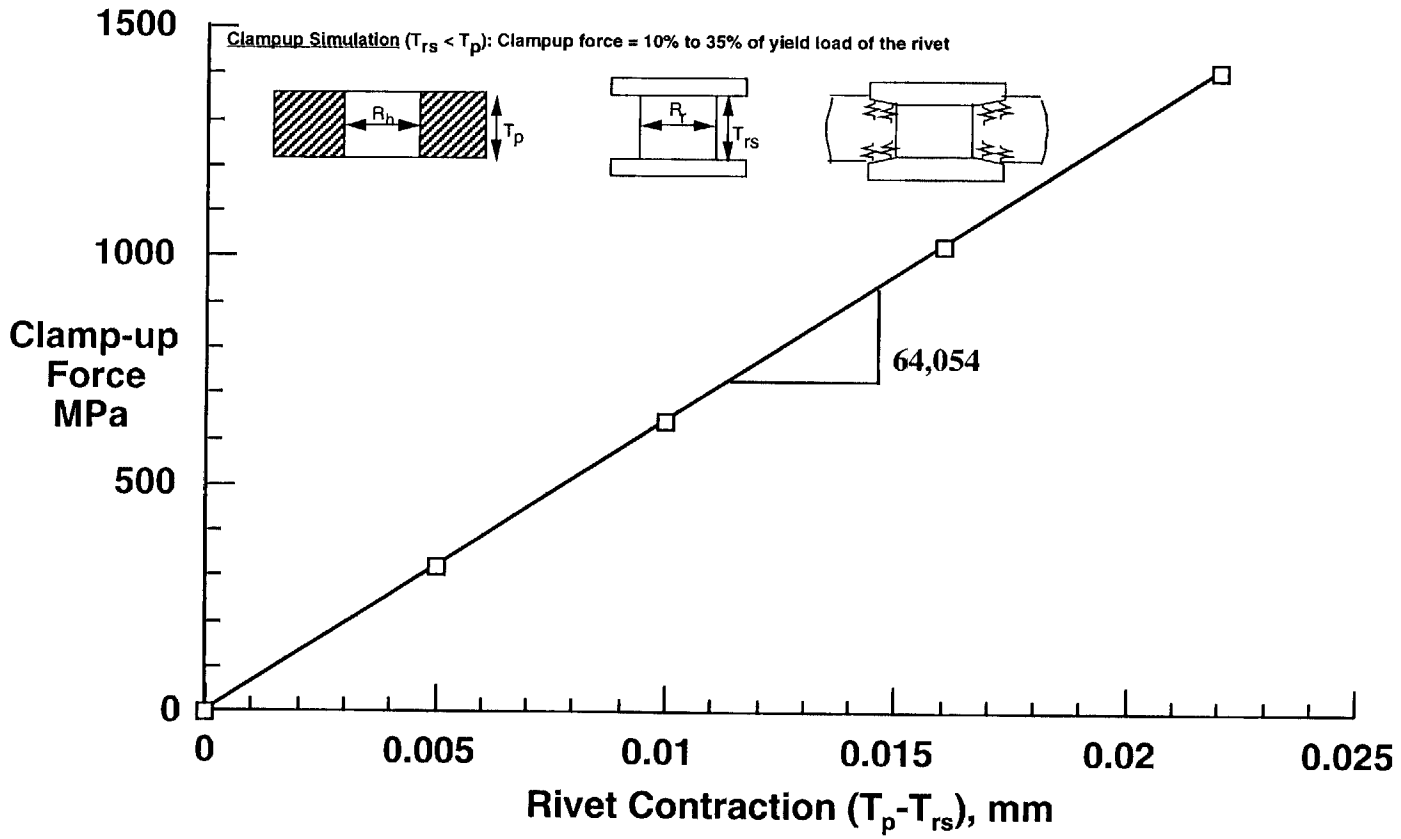

Figure 3.4. Variation of Clamp-up force with rivet contraction.

(a) Global deformation

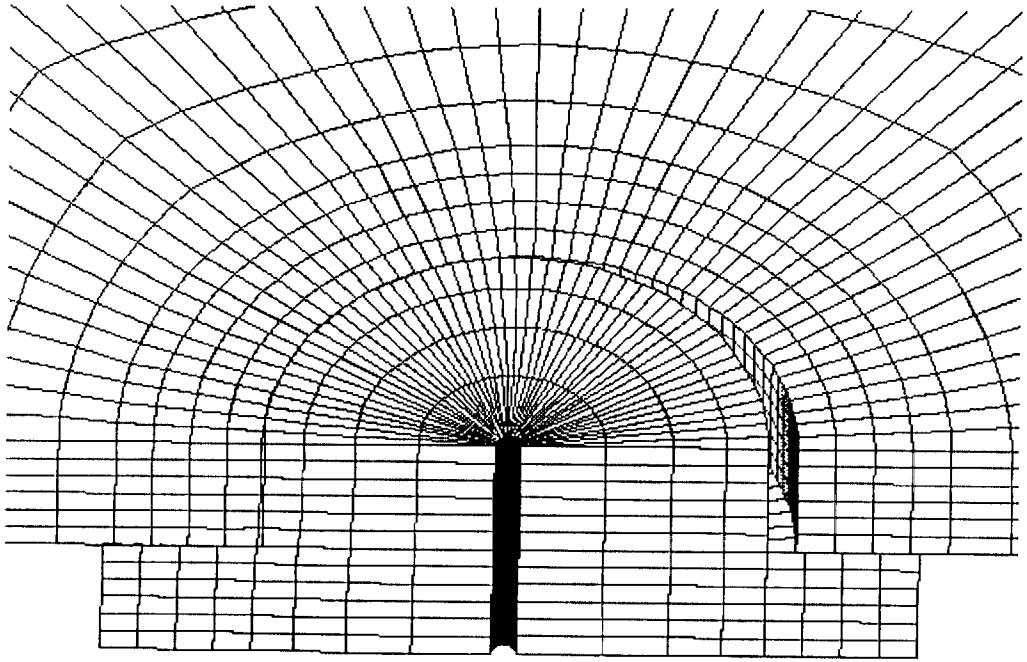

(b) Local to the pin

Figure 3.5. Deformed shape at the pin-hole boundary.

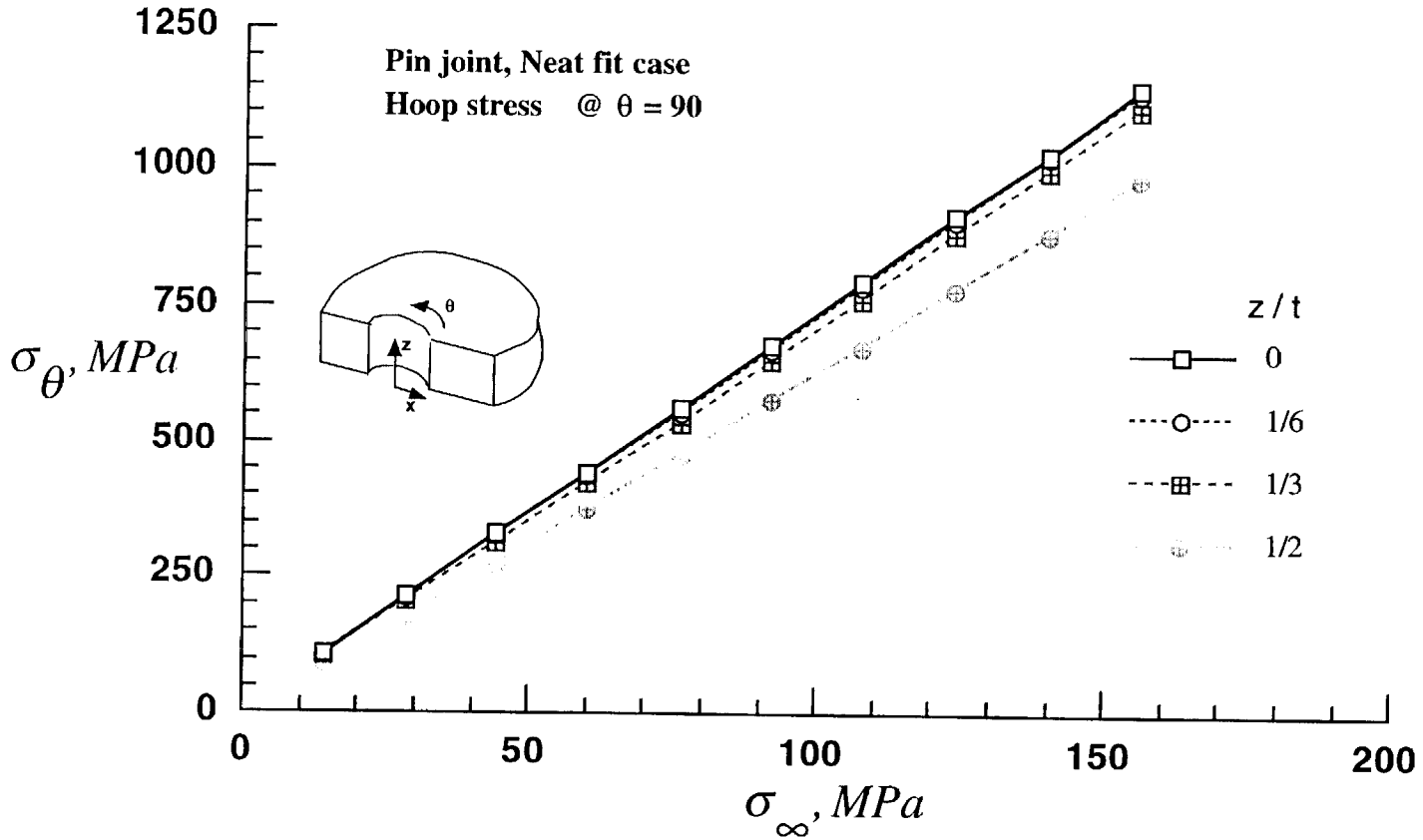

Figure 3.6. Variation of hoop stress with remote stress at various z values

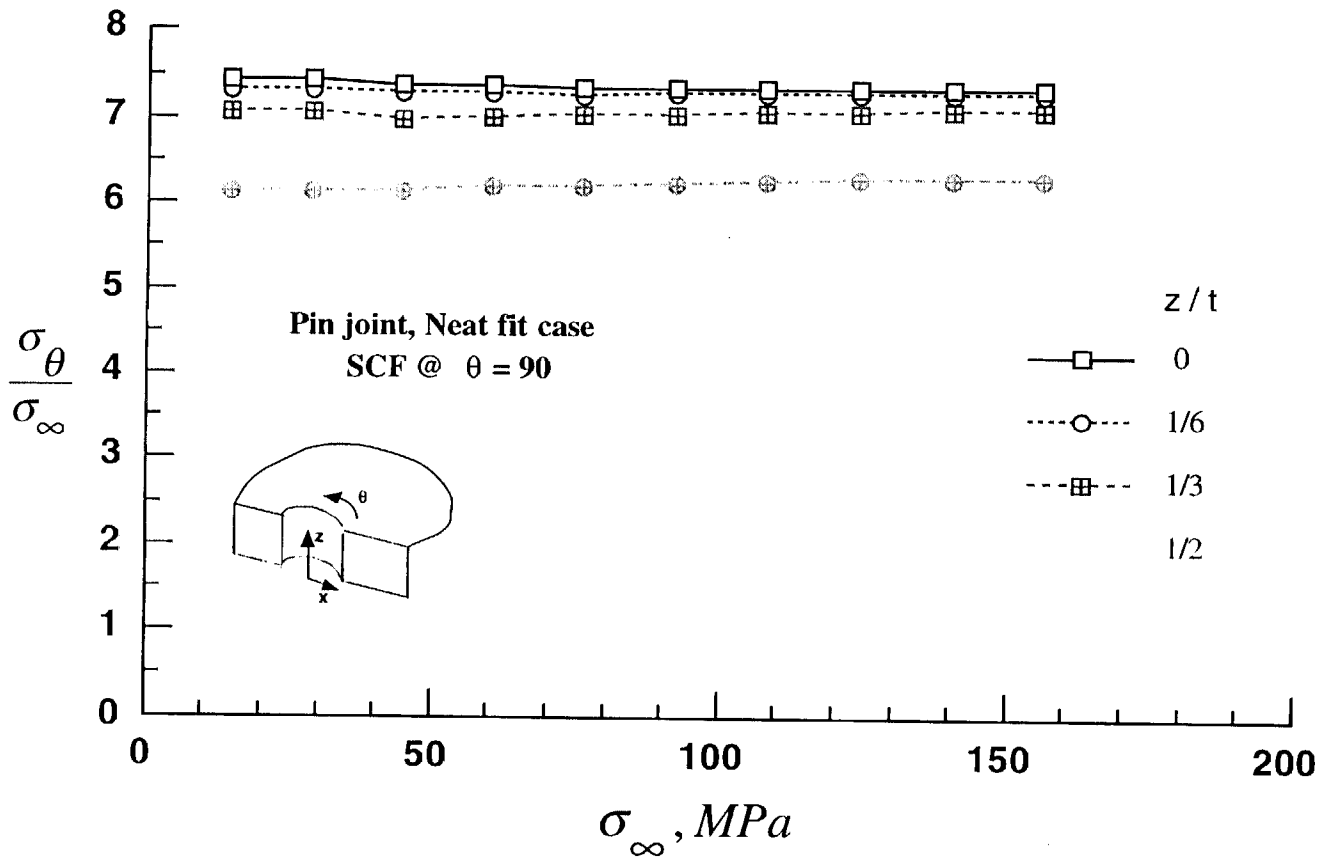

Figure 3.7. Stress concentration versus remote average stress for various z values.

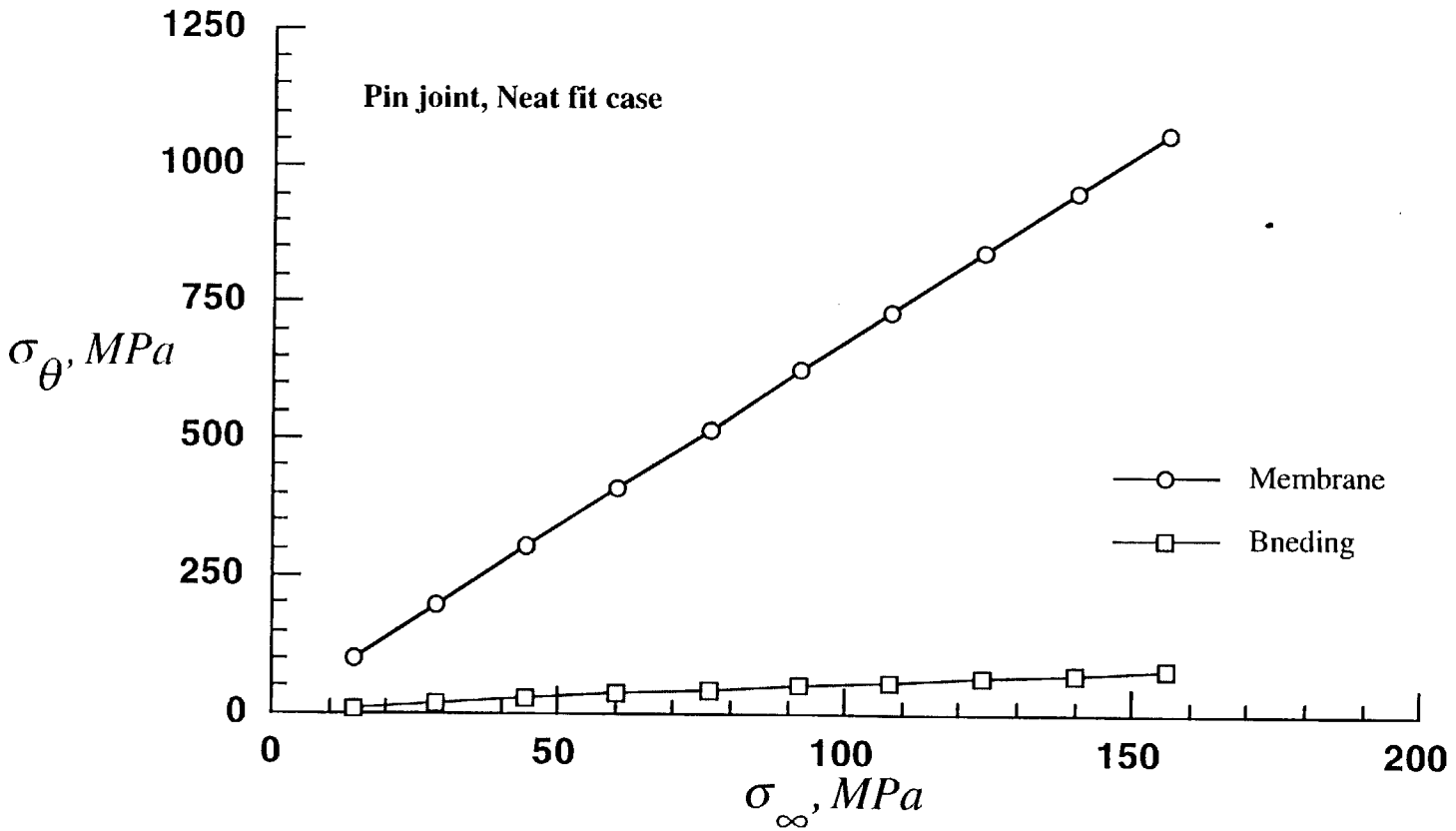

Figure 3.8. Variation of membrane and bending stress components with remote stress.

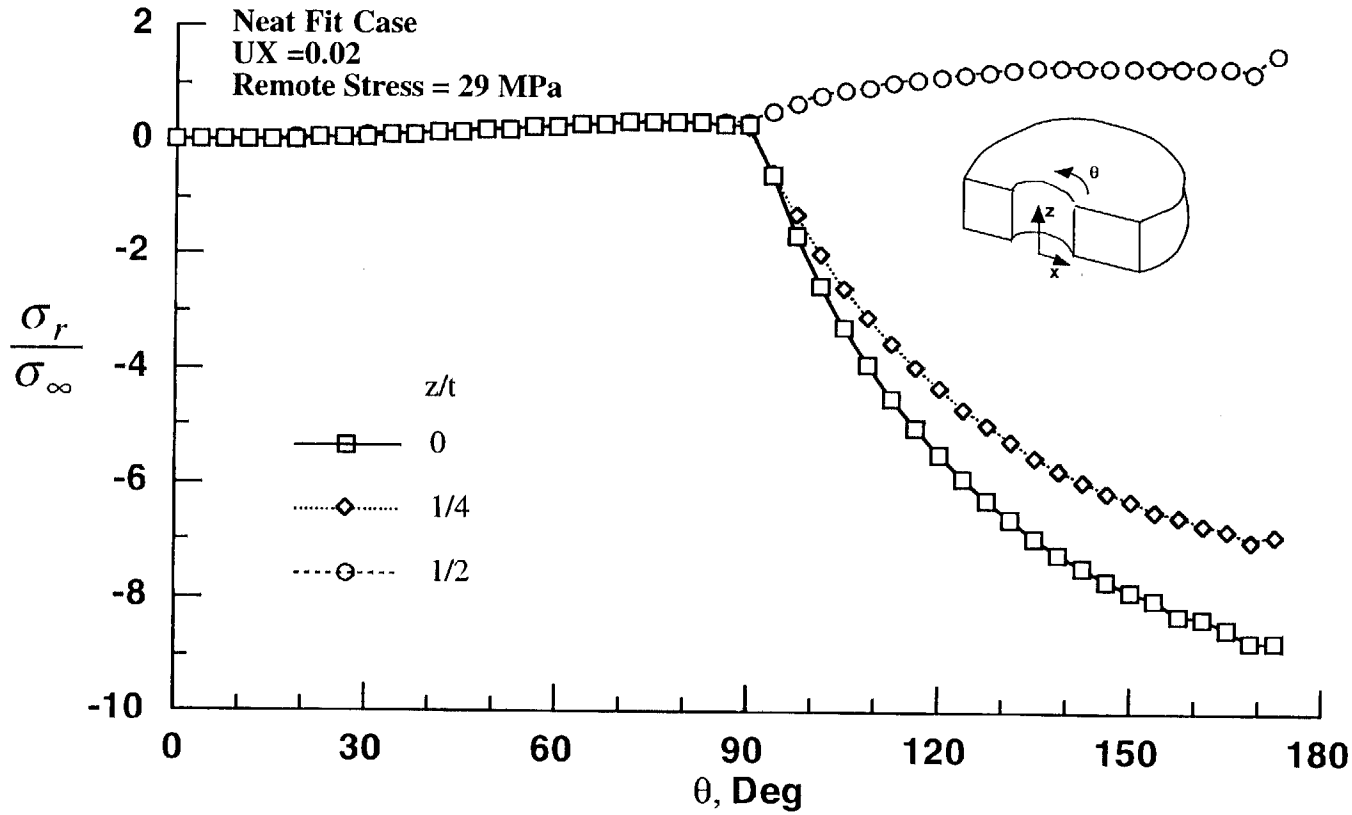

Figure 3.9. Radial stress distribution around the hole boundary (σ_∞ = 29 MPa).

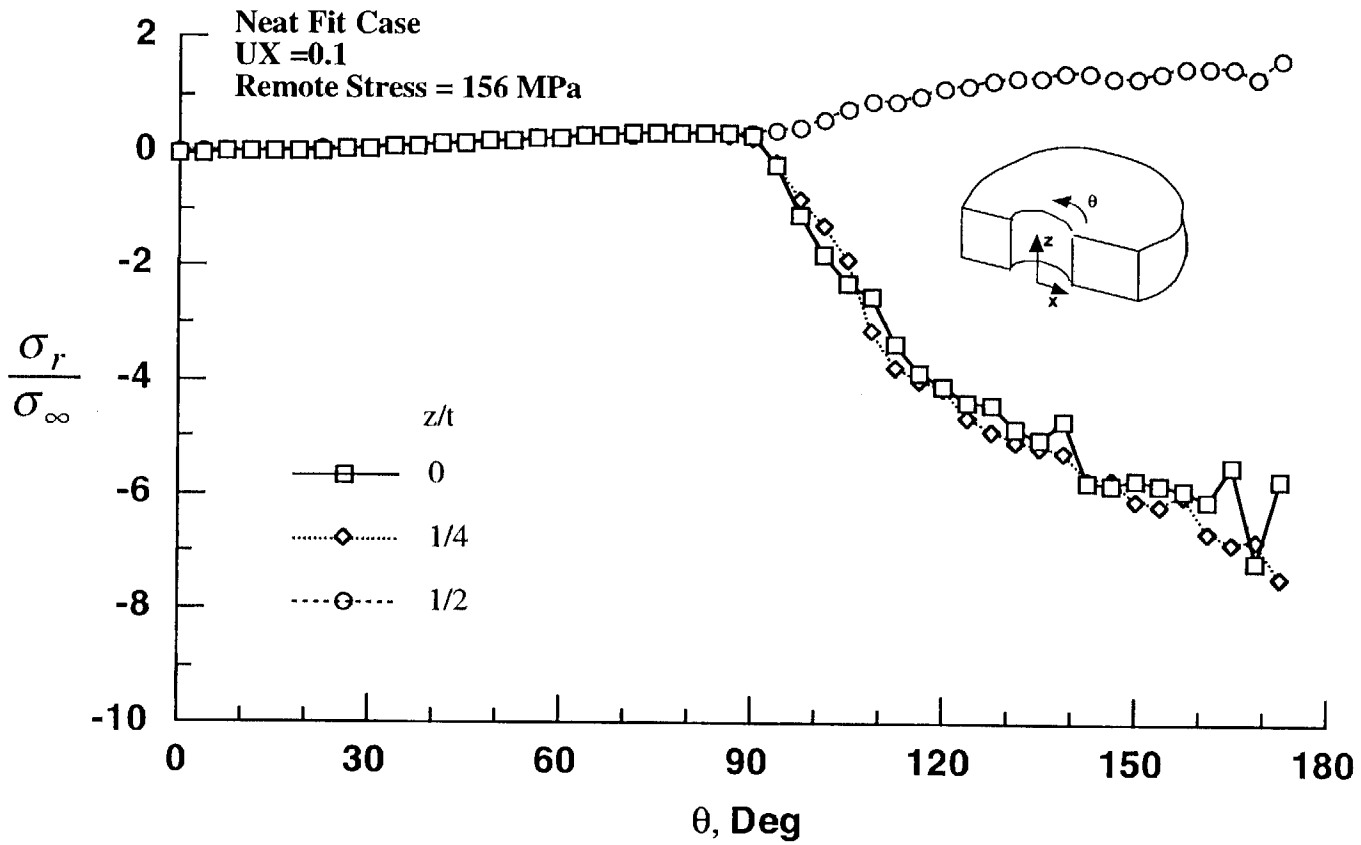

Figure 3.10. Radial stress distribution around the hole boundary (σ_∞ = 156 MPa).

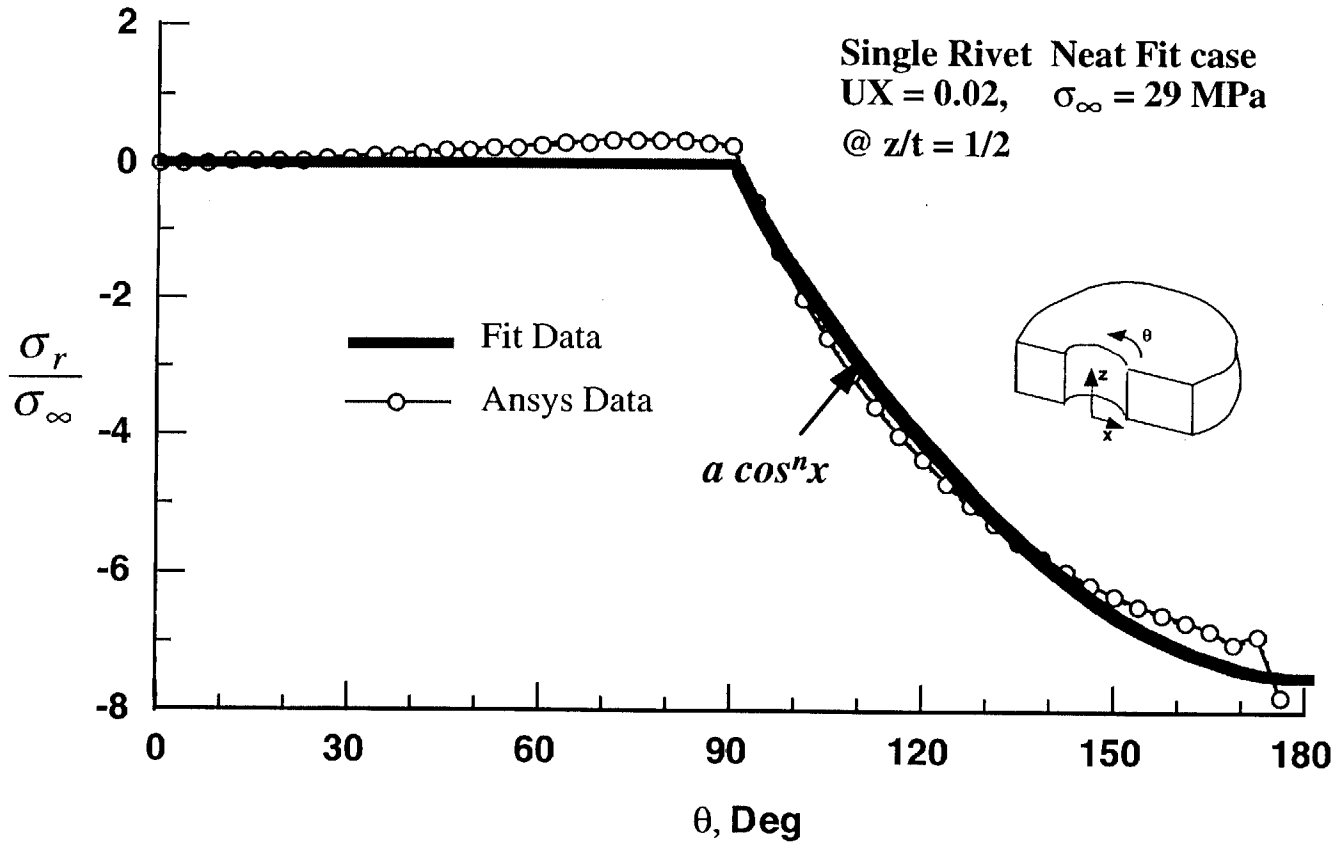

Figure 3.11. Cosine fit for radial stress distribution around the hole boundary (σ_∞ = 29 MPa).

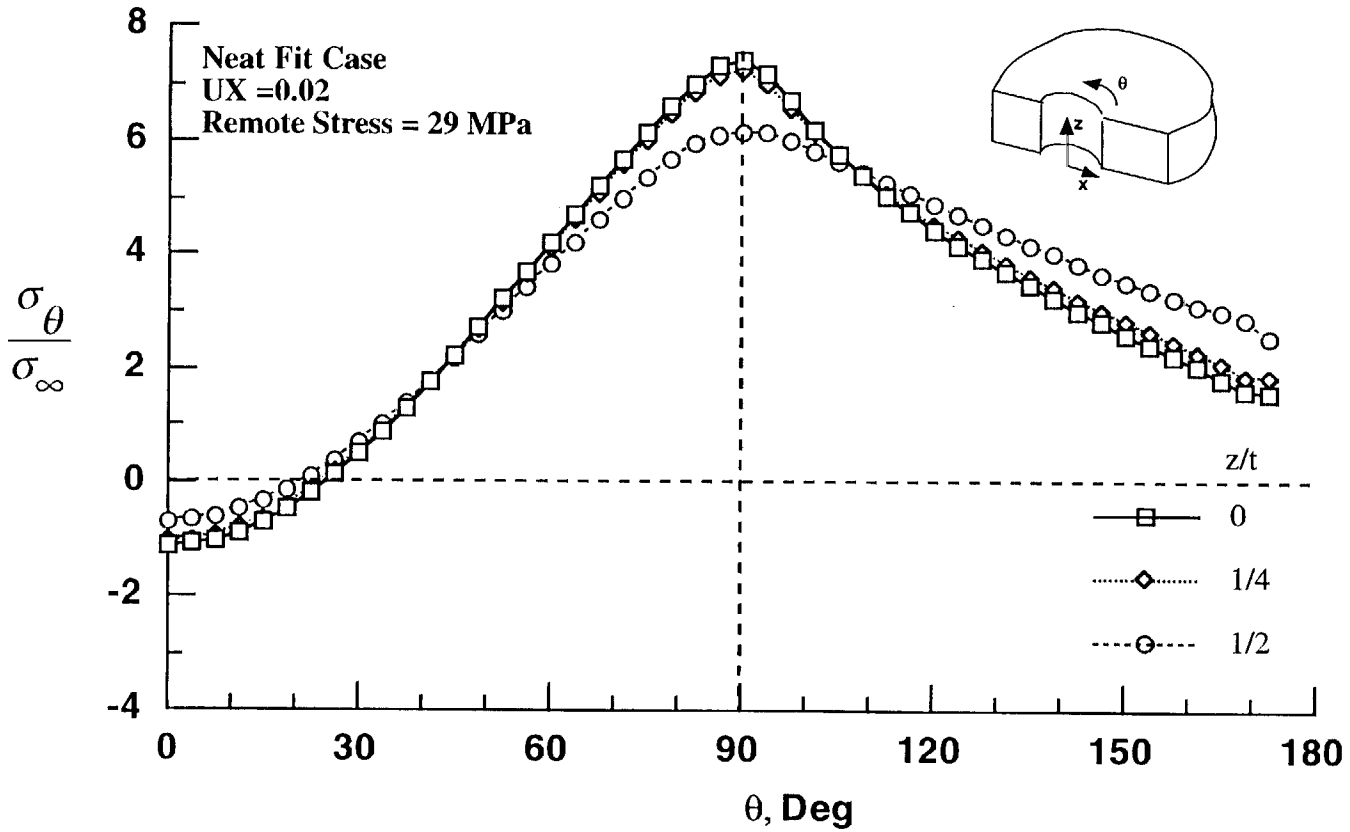

Figure 3.12. Hoop stress distribution around the hole boundary (σ_∞ = 29 MPa).

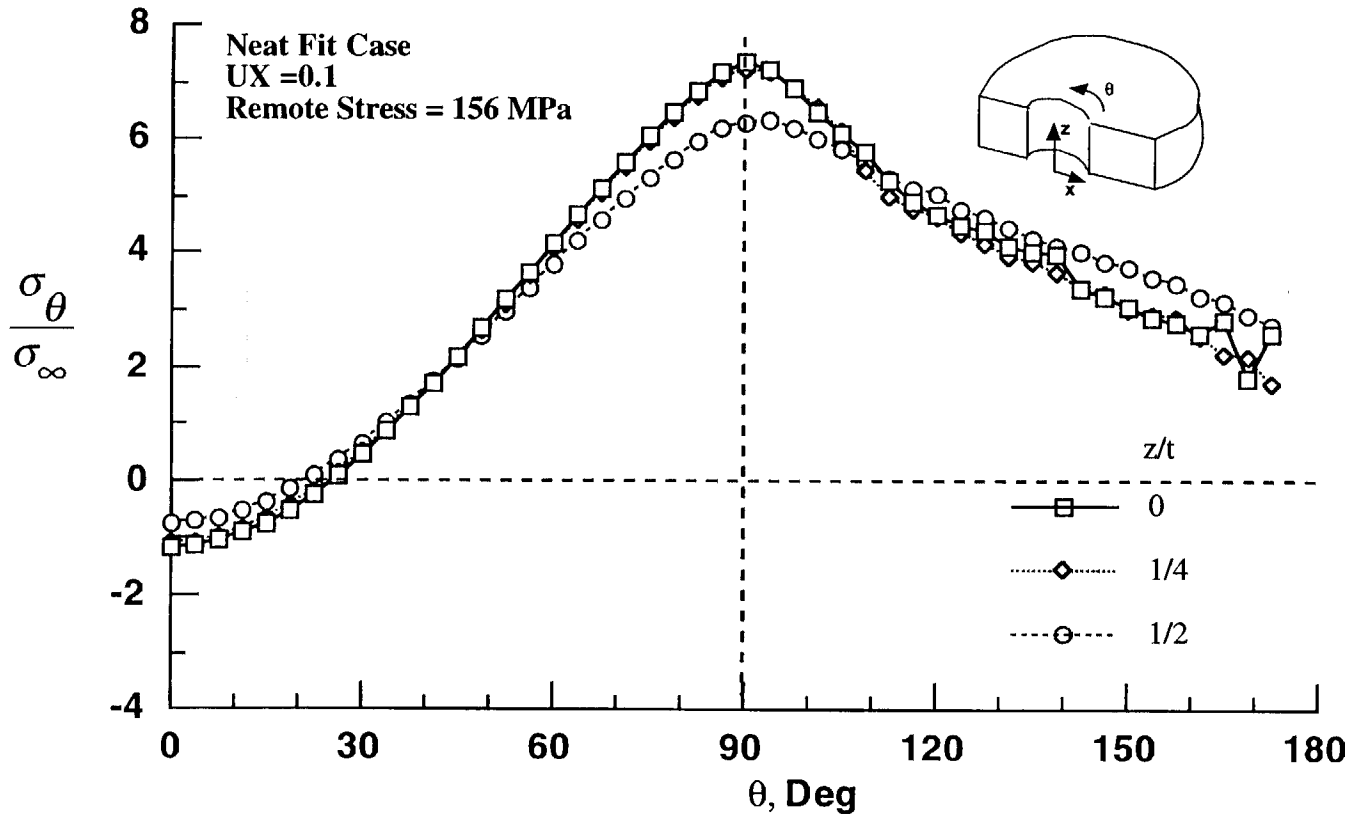

Figure 3.13. Hoop stress distribution around the hole boundary (σ_∞ = 156 MPa).

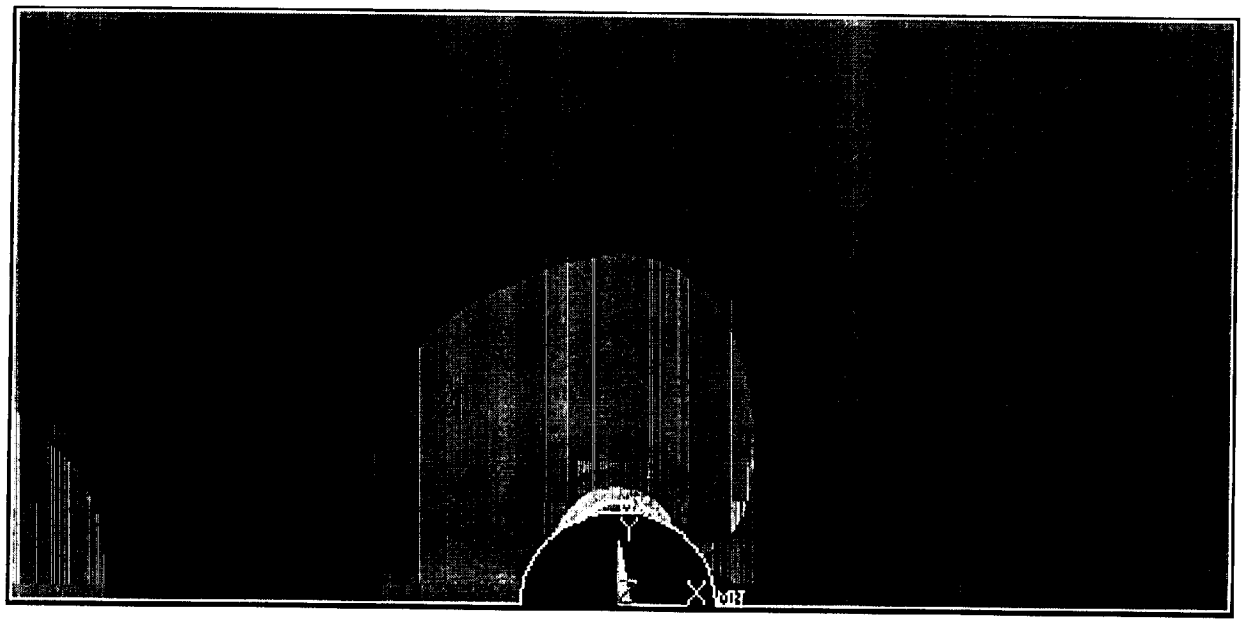

Figure 3.14. Contour plot of the hoop stress in the plate (s_∞ = 156.04 Mpa)

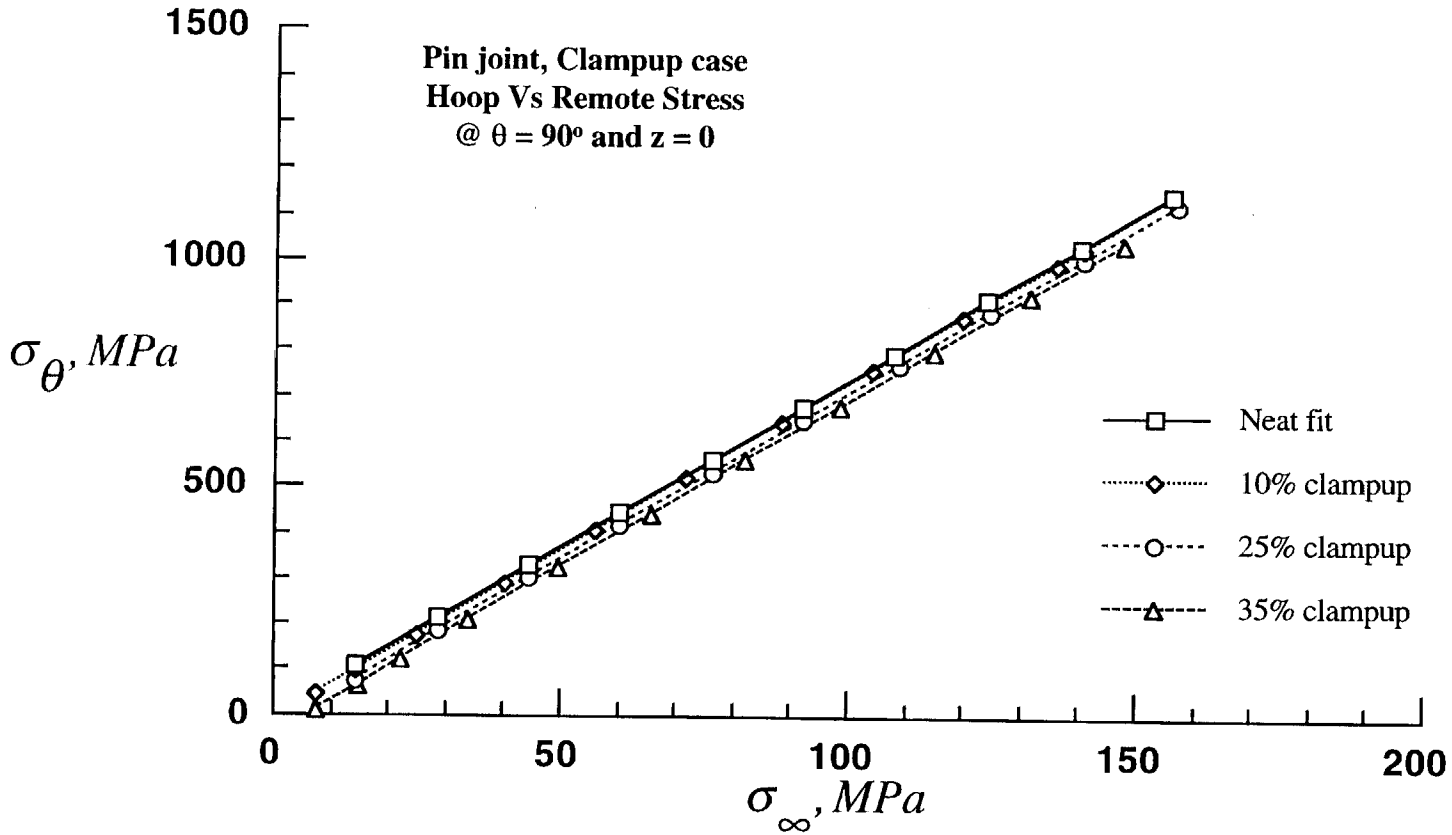

Figure 3.15. Hoop stress vs remote stress at z = 0 and θ = 90° for different clampup.

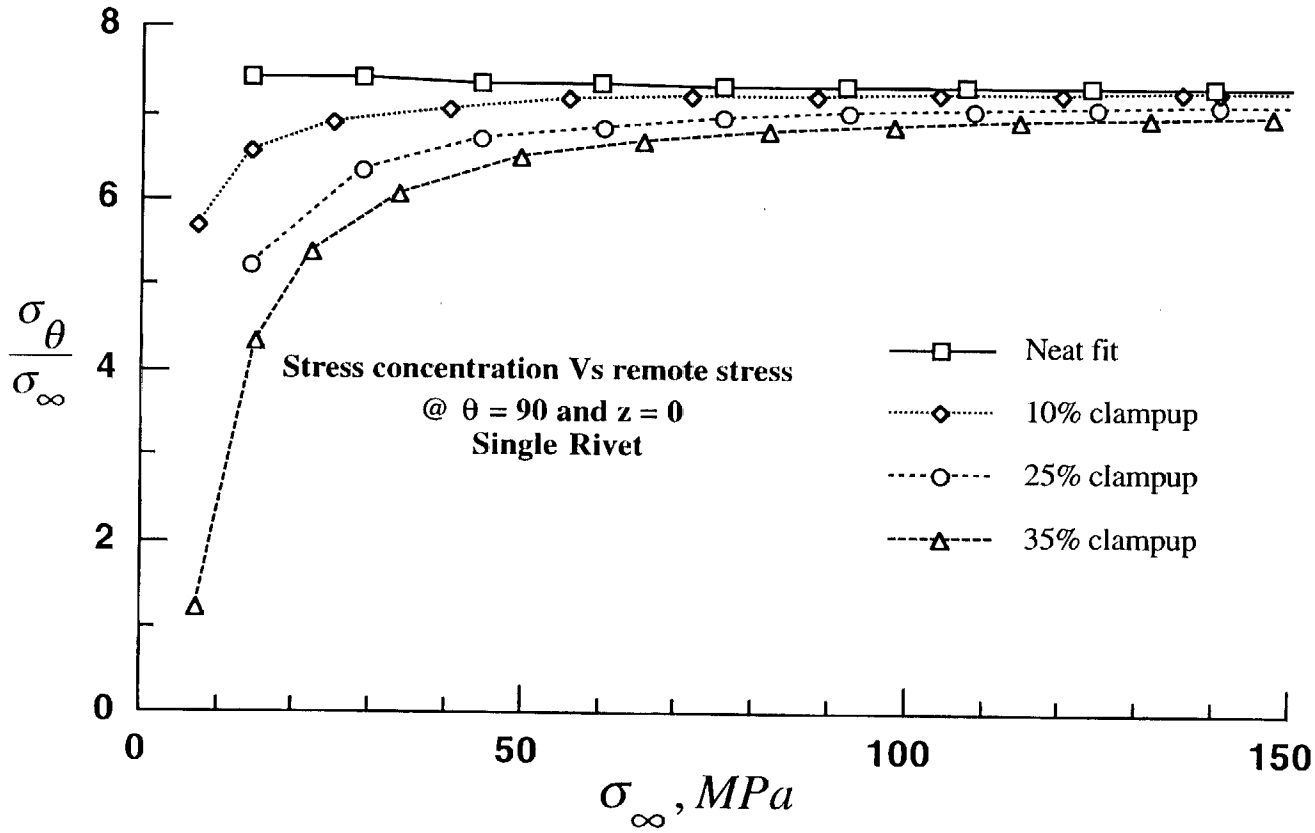

Figure 3.16. Stress concentration factors Vs remote stress for various clampup forces.

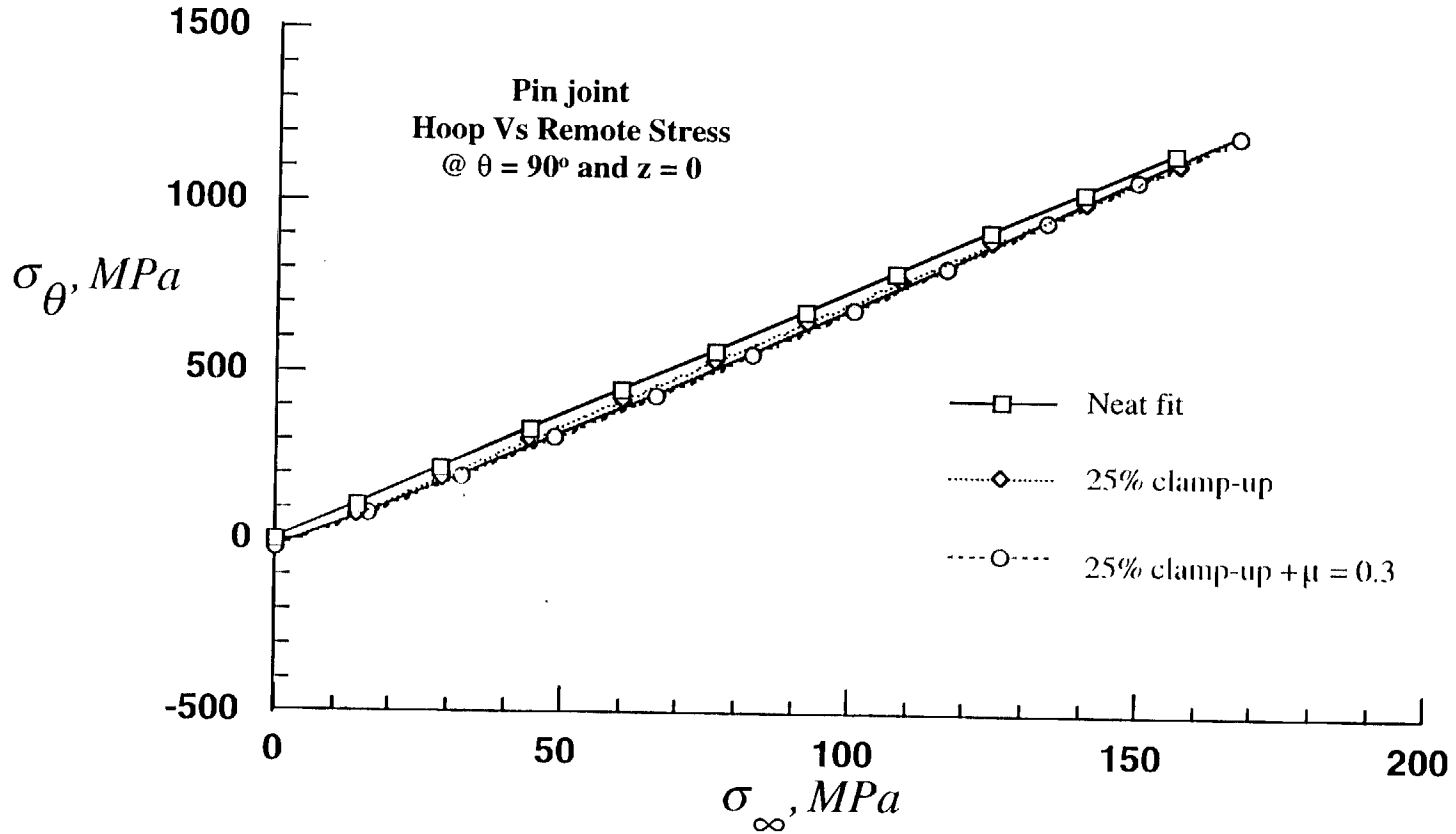

Figure 3.17. Hoop stress vs remote stress at z = 0 and θ = 90° for elastic friction and clampup.

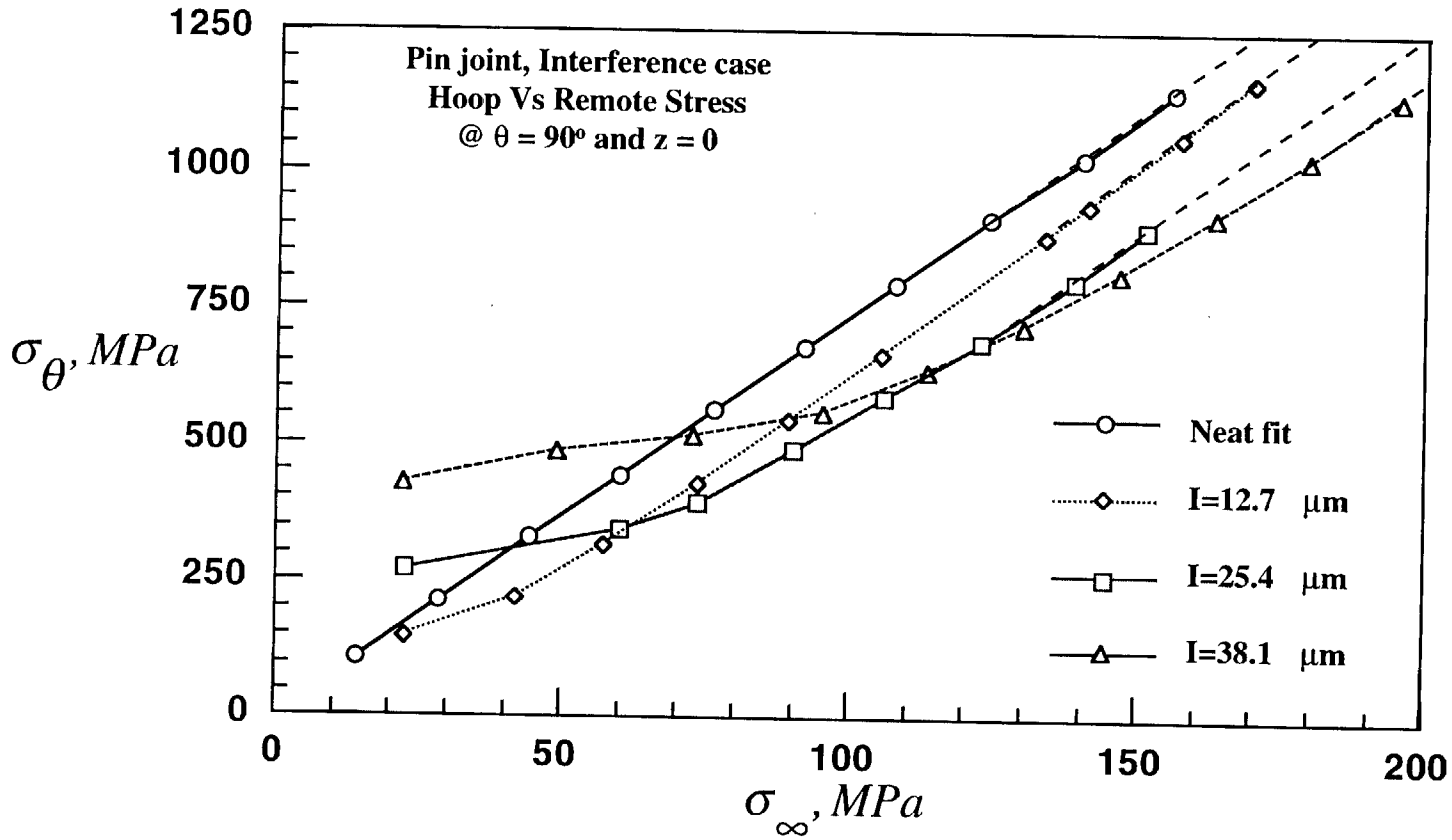

Figure 3.18. Hoop stress vs remote stress at z= 0 and θ = 90° for various interference values.

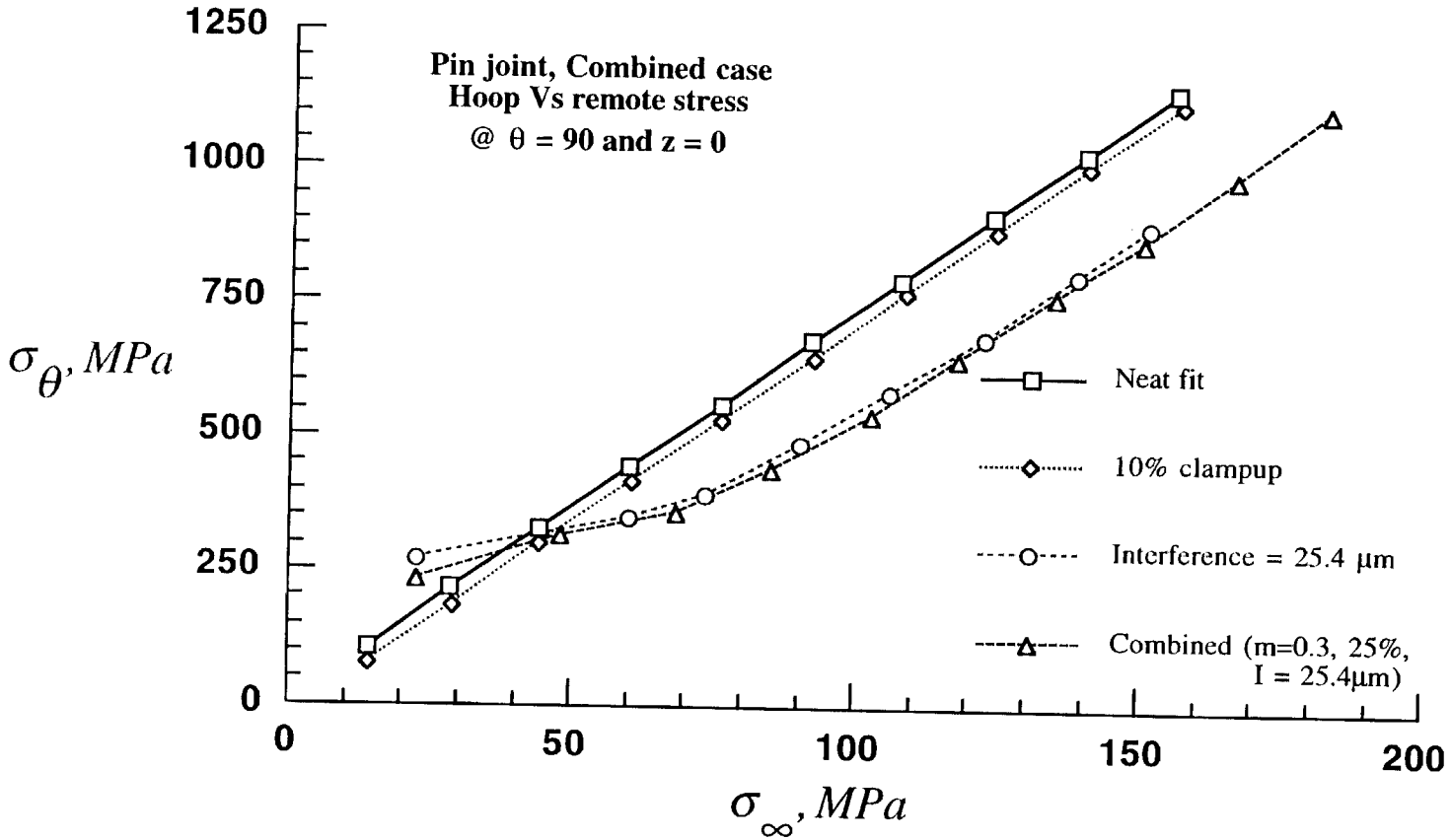

Figure 3.19. Comparison for the combined case

4. TWO RIVET SINGLE LAP JOINT

4.1 Introduction

In this section a single lap joint with two rows of rivets was modeled using 3-D finite elements. This joint is loaded by remote tension and is restrained by using anti-symmetric boundary conditions as explained in the following sections. The effects of clampup and interference on the stress distribution in the hole boundary is presented in this section.

4.2 Joint Configuration

The two-rivet plate joint configuration with all the geometrical parameters are shown in the Figure 4.1. This geometry represents a test configuration used in reference [31]. The plan and sectional view of a two rivet, single lap joint shown in Figure 4.2 was analyzed. The rivet shank was straight with 1.6 mm radius R_r and 2 mm height. The rivet has two button heads. The head radius and depth were 2.55 mm and 1 mm respectively. The two plates, top and bottom were 145 mm long, 20 mm wide (w) and 1 mm thickness (t). The spacing (s) between the rivet centers was 20 mm. The edge distance was (E_d) 10 mm and the length L was 125 mm.

The joint was loaded in tension with an uniform displacement U_o. The average remote stress was σ_∞. The two ends of the joint were supported laterally, to simulate the experimental condition, as shown in Figure 4.2. The Cartesian co-ordinate system selected in modeling is also shown in Figures 4.1 and 4.2. The X, Y, Z represents the global co-ordinate system and *x, y, z* represents the local co-ordinate system used for plotting results.

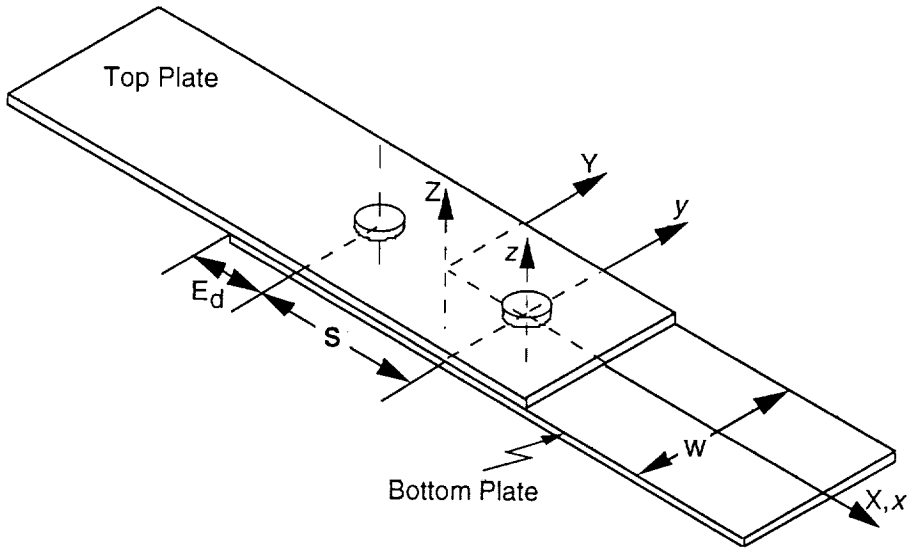

Figure 4.1. Isometric view of the geometric model.

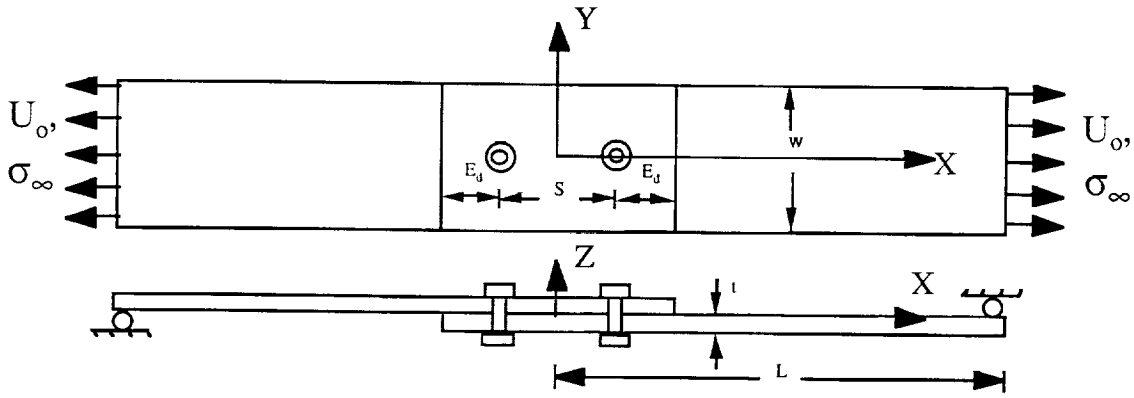

Figure 4.2. Joint configuration of double rivet single lap joint.

4.3 Analysis Model

The rivet joint problem was symmetric about y = 0 plane, hence only one half of the joint was modeled (Figure 4.3). To further reduce the size of the problem, only one quarter of the joint was modeled. This involved imposition of complex constraint condition on X = 0 plane. This constraint condition simulates the mirror image of deformation in the two quarters (left and right). The deformation boundary condition on x = 0 plane is a

combination of anti-symmetry and skew symmetry. The boundary conditions can be expressed by the following constraint equations:

$$U(0, y, -z) = -U(0, y, z)$$

$$V(0, y, -z) = V(0, y, z)$$

$$W(0, y, -z) = -W(0, y, z)$$

These boundary conditions reduce the finite element model to one quarter of the joint (see Figure 4.4).

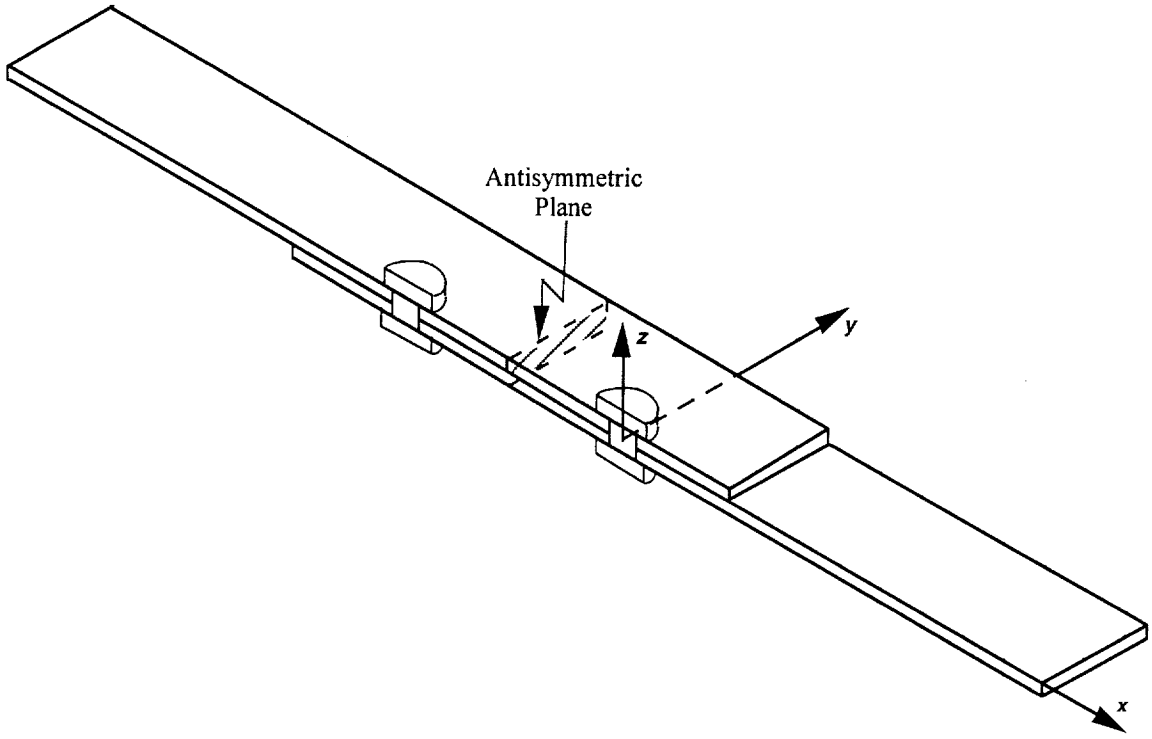

Figure 4.3. Sectional 3-D view showing cyclic anti-symmetry.

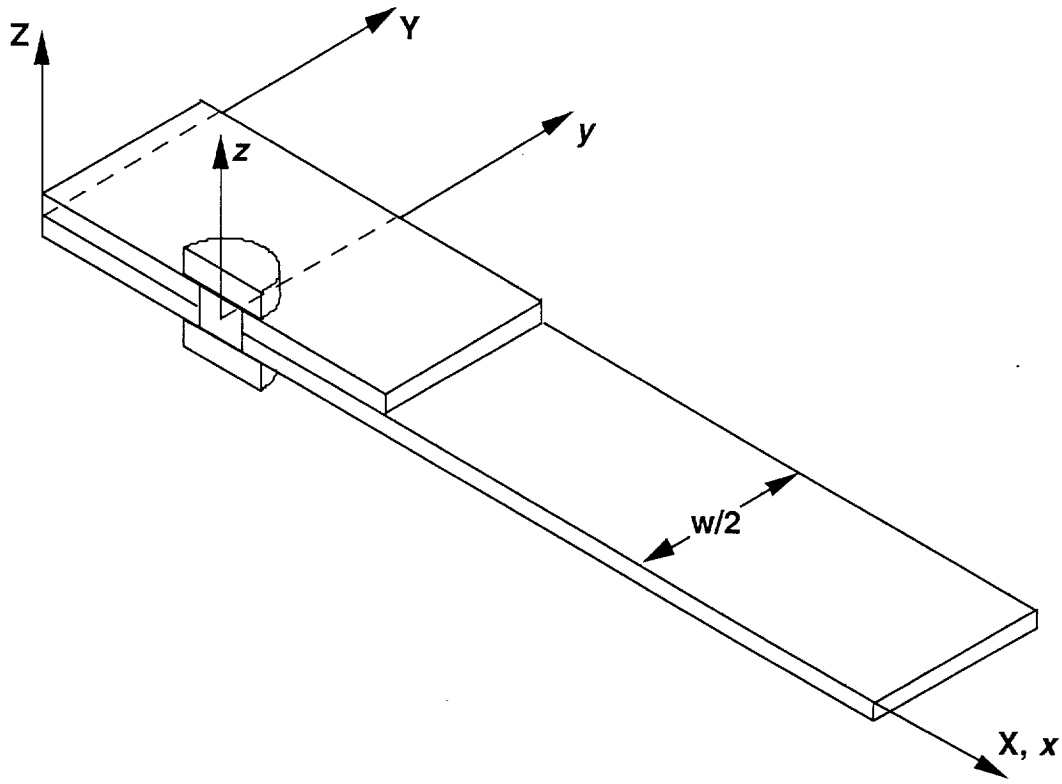

Figure 4.4. One fourth of the model.

Both the plates and the rivet are modeled with 8 noded solid elements (SOLID45 in ANSYS). Finer idealization was used at high stress gradient regions. Various views of the finite element idealization are shown in Figure 4.5. The hole region was divided into segments of 7.5° and the plate thickness was divided into four layers. The rivet shank and head are idealized to match the rivet hole and plate (although the mesh matching was not required for the analysis). Global, local, plan, and sectional views of rivet and plate models are shown in Figure 4.5. The model had 4776 elements and 6650 nodes. The possible contact surfaces in this model were:

1) Between the rivet shank and top and bottom plate's hole.

2) Between the inner surfaces of rivet head and plates.

3) Between the bottom surface of top plate and top surface of bottom plate.

These contact surfaces were modeled using 5-noded 3-D surface to surface contact elements represented by CONTAC49 in ANSYS code. Each target node has the possibility of contacting four elements. The model contained 2588 contact elements.

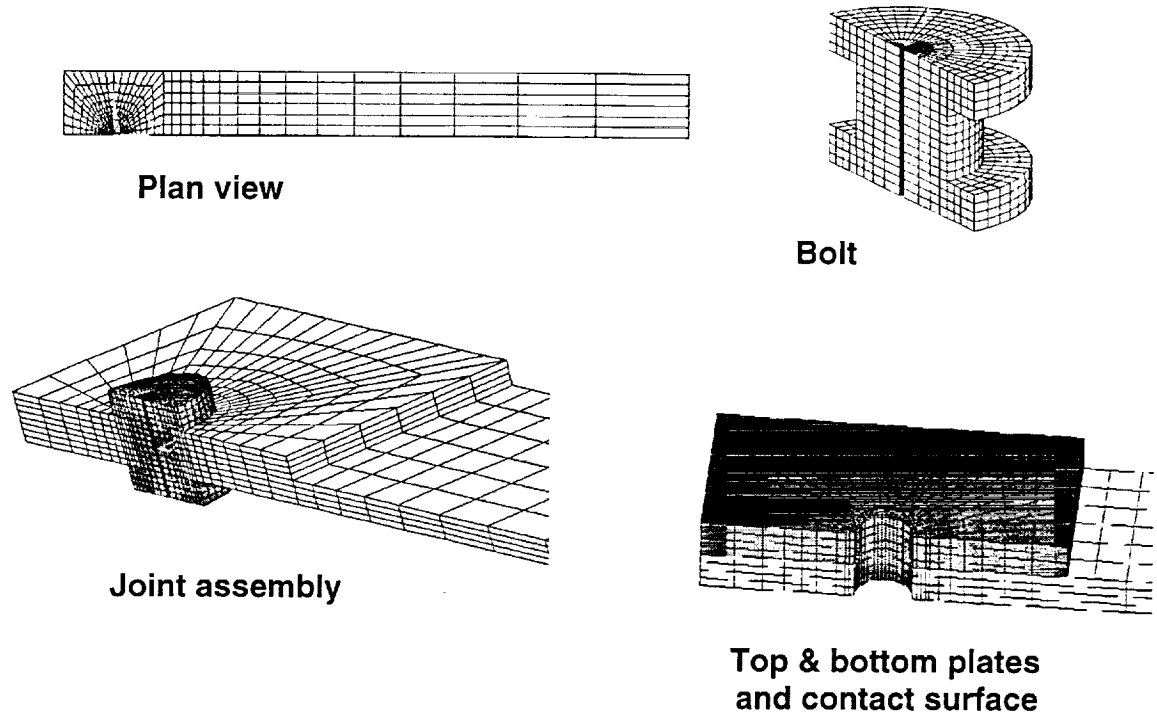

Figure 4.5. Various views of the rivet joint finite element model.

The loading imposed on the model was a uniform displacement 'U_o' at X = L. In summary, the following boundary conditions are applied on the model:

(1) Symmetry on y=0 plane.

(2) Constraint equations on nodes at x=0 plane.

(3) Uy = 0 at x = L, y = 0 and z = 0 (for restricting rigid body motion).

(4) The loading (displacement) u = u_0 was imposed at x = L (125 mm) plane.

Aluminum alloy 2024-T3 Alclad properties were used in the analysis. The rivets are 2024 (type DD) aluminum. The elastic modulus E = 68,950 MPa, Poisson's ratio ν = 0.3, yield strength of 270 MPa and ultimate strength of 270 MPa.

4.4 Analysis Cases

Two types of non-linearities were expected in the model, viz., nonlinear contact boundary and large rotation. Therefore, large deformation and non-linear contact strategy were used in the analysis. A commercial code ANSYS 5.3 was used. The nonlinearities were modeled by modified Newton-Raphson iteration algorithm. The Lagrange multiplier and penalty method were used for contact modeling. The defined gap/penetrations and contact stiffnesses are about 0.01Hs and 2000 N/mm^2 (about 3% of the elastic modulus of the plate material, which was within the recommended range) respectively. But for interference cases gap/penetration value used was 0.025Hs. Where Hs was the smallest element size in the model, which was 0.25 mm. The residual force convergence criteria was used at every node to establish the convergence of the non-linear solution. Relative error in the nodal residual forces was less than 0.1% to 1% of total applied ***force*** as a convergence criteria .

The analysis was conducted for three different complexities that occur in the joint. They are friction between contacting surfaces, rivet clamp-up, and rivet interference. Analytical modeling of each of these parameters is explained in section 2 and is summarized in the following sections. The analysis was conducted by incrementally loading the joint to an applied remote load of about 130 MPa or about U_o = 0.3 mm.

4.4.1 Friction

Friction between the contact surface was modeled as elastic coulomb friction. The surface tangent stiffness KT was selected to be KN/100, where KN was the normal contact stiffness. The tangential friction force at the contacted nodes was the product of friction coefficients and the normal force. The sliding friction coefficients used in the analysis were 0, 0.3 and 0.8. The friction coefficient value of zero represents the smooth contact.

4.4.2 Rivet Clamp-up

As explained in section 2.3 the rivet clamp-up was introduced by changing the length of the rivet shank. By shortening the rivet length compared to the thickness of the two plates clamp-up force was introduced. A separate stress analysis was conducted to establish a relation between clamp-up force and rivet shortening. This relationship was found to be linear (refer to Figure 3.4). The clampup equation was given by

Clampup force, $F_c = 64{,}054 * \Delta L$

where ΔL is the rivet shortening ($T_{rs} - T_p$) in mm

The amount of rivet shortening for clamp-up force of 10%, 25%, 35% rivet yield force was calculated. These values were 7.64, 19.1 and 26.7 μm respectively. The analysis was conducted for all these values of rivet shortening.

4.4.3 Rivet Interference

Rivet interference was introduced by increasing the radius of the rivet (R_r) in relation to the hole radius (R_h). Three values of interference $2(R_r-R_h)$ chosen were 12.7, 25.4 and 38.1 μm. These values bound the real values experienced in the aircraft industry.

4.5 Results

Results of the analysis conducted for various cases are represented in this section. First, neat fit (zero surface-surface friction) results are presented. Then the effects of

friction, clamp-up and interference on local stresses were examined. The primary focus was on the maximum hoop stress on the hole boundary and the hoop stress at 90° to the x-axis. The second case is where the hoop stress is maximum for open hole problems.

4.5.1 Neat Fit Results

4.5.1.1 Deformed Shapes

Figure 4.7 shows the sectional view of the deformed shape of the model. Notice that the two plates slided one past the other at the left end of the model. This is the true deformation expected if the complete half model was analyzed. This deformation pattern confirms the approximation of the boundary conditions imposed on X = 0 plane. The close-up view of the model at the rivet is shown in Figure 4.8. Notice that the rivet is in contact with top plate on the right side and bottom plate left side. The right side of bottom plate and the left side of top plate are separated from the rivet shank. The two plates are separated from each other on the loaded side. In the 3-D model like this problem, all separation and contact are only partial and they change along the polar (θ) direction of the rivet. Figure 4.9 shows the superposed view of the two quarters of the model. This depicts the local joint rotation and deformation.

4.5.1.2 Contact Nonlinearity

The effect of contact nonlinearity on local stresses was examined by analyzing the hoop stress at $\theta = 90°$ on the hole boundary of the plates. Figure 4.10 shows the variation of σ_θ with remote applied stress (σ_∞) at various values of 'z' at $\theta = 90°$. Except at low values of applied stress, $\sigma_\infty < 30$ MPa, σ_θ varies linearly with σ_∞. The same results are plotted as stress concentration factor (SCF = $\sigma_\theta / \sigma_\infty$) in Figure 4.11. Again, the SCF is maximum for the bottom plate at Z = 0, which is about 5.7.

Figure 4.12 shows almost linear variation of membrane and bending stresses with σ_∞. Membrane stress is the average stress through the thickness and bending stress is half

the difference between the top and bottom surfaces of the bottom plate at θ = 90°. Both membrane and bending stresses vary linearly through the thickness. The membrane SCFs were 4.75 and 3.4 for the bottom and top plates whereas the bending SCF were 1.2 and 0.6 for the bottom and top plates respectively.

4.5.1.3 Radial Stress Distribution at the Hole Boundary

Figures 4.13 and 4.14 shows the contact (radial) stress distribution on the hole boundary for remote applied stress of 45 and 84 MPa respectively. Radial stress is maximum at θ = 180° for the bottom plate and θ = 0° for the top plate (not shown). The radial stress can be approximated by cosine function (see thick solid curves). These cosine functions are of the form shown below:

$$\frac{\sigma_r}{\sigma_\infty} = a\cos^n \theta$$

Note that contact stress is zero at θ = 90° for most of the locations through the thickness. Results at z = -1.0 (corner location) may not be accurate because they are being affected by rivet head contacts.

4.5.1.4 Hoop Stress Distribution at the Hole Boundary

Figures 4.15 and 4.16 shows hoop stress distribution on the hole boundary for the applied stress of 45 and 84 MPa respectively. The hoop stress peaks at θ = 90° for values of z through the thickness. The maximum stress is at z = 0.0, which is about 5.7 times that of the remote stress.

4.5.1.5 Hoop Stress Contour Plots

Figure 4.17 shows the hoop stress contour plots on both top and bottom plates. The plate is sectioned at x = 0 plane to examine the location of maximum sq through the width. Results on Figure 4.17 concludes that for a smooth fit case, the location of the maximum hoop stress is on the hole boundary and at z = 0.0.

In all the results presented so far, hoop stress on the hole boundary is highest and it occurs in the bottom plate at the interface between the two plates.

4.5.2 Elastic Friction

Stress analysis was conducted for elastic friction values of 0.3 and 0.8 for applied remote stress varying from 0 to about 140 MPa. Both radial and hoop stress distribution along the hole surface and through the thickness were examined for all cases and compared with neatfit results. Comparison of results showed very little effect of friction on magnitude and location of peak values. Tensile stresses in the bottom plate were higher than that in the top plate. Therefore, only results for the bottom plate are presented for this case and all other remaining cases. Figure 4.18 and 4.19 shows hoop stress variation along the hole surface at various plate thickness locations for $\mu = 0.3$ and $\mu = 0.8$ respectively. For both cases σ_θ is maximum at $\theta = 90^\circ$ and $z = 0$.

Figure 4.20 shows variation of σ_θ at $\theta = 90^\circ$ with remote stress (σ_∞) for $\mu = 0$, 0.3 and 0.8. Results of $\mu = 0$ and $\mu = 0.3$ were almost identical and at low values of σ_∞,, $\mu =$ 0.8 stresses were smaller than $\mu = 0$ case, but for $\sigma_\infty > 55$ MPa, all three curves merged. Therefore, elastic friction alone has very little effect or no effect on joint stresses.

4.5.3 Clampup Force

Stress analysis was conducted for three values of clampup force, namely, 10%, 25% and 35% of the yield load of the rivet. Both hoop and radial stresses on the hole boundaries were examined. The important findings are presented. Maximum hoop stress occurred at the hole boundary except for very small value of remote applied stress. At very low applied stress, the maximum hoop stress occurred in the interior of the plate, this may be because of pinching effect caused by clamping.

Figures 4.21 to 4.23 shows the σ_θ stress distribution on the hole boundary for 10% clampup force at remote stresses of 45.7, 94.5 and 143.7 MPa respectively. Maximum hoop stress location changed from 75° at low load levels to 90° at high loads. Again the two plate's interface location was highly stressed region in the plates. Table 4.1 summarizes the magnitude and location of maximum hoop stress for all three clampup forces and various applied stress values. The location of maximum stress is at 75° for both 25% and 35% clampup force for higher values of applied stress.

The table also lists the hoop stress values at $z = 0$ and $\theta = 90°$, and the difference compared to the maximum stress. The difference increases with increased clampup force but decreases with increase of applied stress. For 10% clampup force, one can neglect the difference for $\sigma_\infty > 50$MPa. Knowing σ_θ at $\theta = 90°$ and $z = 0$, for any condition, one can calculate back the maximum value of the hoop stress and its location using the table 4.1 results.

Figure 4.24 shows variation of σ_θ at $\theta = 90°$ and $z = 0$ for the three values of clampup forces and for various σ_∞ loads. The Figure clearly demonstrates that, as expected the hoop stress at the hole boundary also decreases with increase of clampup force. The relationship between the clampup force and the hoop stress can be expressed by a simple equation:

$$(\sigma_\theta)_{\text{Clampup}} = (\sigma_\theta)_{\text{Neatfit}} - 31C_\sigma$$

where C_σ is the clampup stress, defined as clampup force divided by clamping area of the plate. In the equation, all stresses are expressed in N/mm^2 (MPa). At low applied stresses, clampup has nonlinear effect on the local stresses.

Figures 4.25 and 4.26 show the effects of clampup on membrane and bending components of the stress on the hole boundary at $\theta = 90°$. Membrane stresses decreases with increase in clampup, where as the bending stresses increases.

Figure 4.27 shows the variation of $\sigma_\theta/\sigma_\infty$ with radial distance from the hole boundary. The clampup effect is confined to clamped region, beyond that the hoop stress are unaffected by the clampup; particularly for higher remote stress (σ_∞ = 140 MPa). However at lower load levels, say 65 MPa, the influence of clampup goes slightly beyond the clampup region. The magnitude of change is minimal. Hence it terms of crack initiation and crack growth, clampup can increase the crack initiation life but once the crack has grown beyond the rivet head, clampup has no effect on crack growth.

4.5.4 Clampup and Elastic Friction

This analysis was conducted with the intention that the clampup force would increase the normal force between the plate surfaces and hence the friction effect (the tangential friction force is equal to the product of the normal force and the coefficient friction). Figure 4.28 shows that friction still does not have any effect on the hoop stress distribution on the hole boundary. Hence we can conclude that friction has no effect on stress distribution in the joint.

4.5.5 Interference

Figure 4.29 and 4.30 show the hoop stress distribution around the hole boundary for an interference value of 12.7 mm and remote stress value of 48.7 and 78.7 MPa respectively. As can be seen from Figure 4.29 the maximum hoop stress occurs at $\theta = 67.5^\circ$ and as the remote load increases the location of maximum hoop stress shifts to $\theta = 75^\circ$ at remote load of 78.7 MPa (Figure 4.30). This trend can be also be inferred from table 4.2 which lists location of maximum hoop stress for all interference values. The maximum hoop stress location varies from 135° (for low load levels) to about 75° for high load levels.

Figure 4.31 and 4.32 show the radial stress distribution around the hole boundary. As can be observed the radial stress became negative before 90° for all values of z. This is because of the interference effect. Since the rivet shank diameter is greater than that of the

plate hole, the rivet is in contact with more than quarter of the hole boundary and this induces compressive radial stresses on the plate hole even for $\theta < 90°$.

The effect of interference on hoop stress at $z = 0$ and $\theta = 90°$ is shown in Figure 4.33 and the results are compared with neatfit case. Notice there are three distinct regions behaving differently. At low applied stresses, the local hoop stresses (σ_θ) increases with increase in interference value and it is larger than the neat fit case. At very large applied stress, local σ_θ for the neat fit case is larger than all the interference cases. In between these two regions, the results cross each other. However, interference introduces initial tensile stress on the hole boundary and the rate of increase of σ_θ decreases with the amount interference. The slope of σ_θ curve decreases from neatfit to 12.7, 25.4, and 38.1 μm. All four curves cross each other at different applied stress values. The trend of the curves indicate that eventually (at large σ_∞) they will all be parallel to each other with neatfit case having highest σ_θ and the largest interference having the lowest σ_θ. From these results we can conclude:

1. Because interference case introduces initial tensile stresses at $\sigma_\infty = 0$, the alternating component of the local stress due to alternating σ_∞ is lower than the neat fit results.

2. Slope of the σ_θ vs σ_∞ is smaller with increased interference. This in effect reduces the alternating component of the local stress σ_θ.

4.6 Summary

Conducted detailed 3-D stress analysis of single lap joint with two rows of rivet including the effect of friction, clampup, and interference. Practical ranges of clampup force (0 to 35 % of axial yield load of rivet) and interference (0 to 38.1 μm) were used in the parametric study. Results concluded that:

(1) For the neat fit case hoop stress on the hole boundary was the highest and it occurred in the bottom plate at the interface between the top and bottom plates at 90° to the load axis. The maximum stress concentration factor was found to be 5.7. Contact nonlinearity was confined to low levels of applied load (σ_∞.< 30 MPa). At higher applied loads the response is almost linear. The radial stress distribution on the hole boundary can be represented by a cosine function of type $\frac{\sigma_r}{\sigma_\infty} = a\cos^n\theta$. Values of 'a' and 'n' depend on the through the thickness location on the hole boundary.

(3) Elastic friction has negligible effect on local stresses (hoop) and hence it can be ignored.

(4) For the clampup case, again the maximum stresses occurred on the hole boundary and in the bottom plate. The clampup force did decrease the stresses at the critical location and its effect can be summarized in the form of a simple linear equation. For 10% clampup level, maximum hoop stress location changed from 75° at low load levels to 90° for high load levels. But for 25% and 35% clampup it remains at 75° for almost all load levels. The Clampup effect was confined to the region under the rivet head. Beyond the rivet head it's effects were significantly reduced.

(5) Interference is major factor that impacts the local stresses (hoop stress) around the rivet hole. Interference reduces the rate of increase of local stresses with remote loads. This causes the local (hoop) stresses to be lower than the neat fit results at high load levels.

Table 4.1. Maximum hoop stress location in bottom plate for different clampup forces

Remote Stress	Maximum Hoop stress	Coordinates r	q	z	Stress At z=0,q=90	%difference
10% Clamp-up						
21.9	118.5	1.6	67.5	0.0	101.4	16.8
65.1	348.4	1.6	75.0	0.0	337.8	3.1
94.5	496.6	1.6	90.0	0.0	496.6	0.0
119.0	631.9	1.6	90.0	0.0	631.9	0.0
143.7	768.9	1.6	90.0	0.0	768.9	0.0
25% Clamp-up						
21.7	127.2	1.6	67.5	0.0	58.1	118.8
63.9	364.4	1.6	75.0	0.0	288.3	26.4
94.2	504.9	1.6	75.0	0.0	454.1	11.2
119.0	624.6	1.6	75.0	0.0	584.2	6.9
143.6	737.1	1.6	75.0	0.0	716.4	2.9
35% Clamp-up						
26.3	187.3	1.6	60.0	0.0	67.7	176.5
64.7	335.7	1.6	75.0	0.0	264.2	27.1
94.1	467.7	1.6	75.0	0.0	407.8	14.7
117.6	572.6	1.6	75.0	0.0	535.9	6.9
143.4	705.6	1.6	82.5	0.0	676.4	4.3

Table 4.2. Maximum hoop stress location in bottom plate for different interference

Remote Stress	Maximum Hoop stress	Coordinates r	q	z	Stress at z=0,q=90	%difference
Interference = 12.7 mm						
28.68	178.87	1.60	105.00	-0.75	175.57	1.88
48.70	251.33	1.60	67.50	0.00	232.10	8.29
58.85	296.57	1.60	75.00	0.00	268.38	10.50
68.67	346.88	1.60	75.00	0.00	311.45	11.38
78.71	388.03	1.60	75.00	0.00	358.42	8.26
Interference = 25.4 mm						
28.03	317.68	1.60	112.50	0.00	292.12	8.75
38.42	332.18	1.60	105.00	0.00	308.50	7.68
59.21	363.32	1.60	105.00	0.00	345.49	5.16
99.77	484.54	1.60	67.50	0.00	451.23	7.38
110.14	525.37	1.60	67.50	0.00	481.78	9.05
Interference = 38.1 mm						
27.29	455.83	1.60	112.50	-0.75	411.75	10.71
57.47	498.18	1.60	105.00	-0.75	457.50	8.89
94.91	555.58	1.60	105.00	-0.75	522.80	6.27
106.36	574.80	1.60	105.00	-0.75	546.96	5.09
118.10	600.45	1.60	82.50	0.00	552.93	8.59

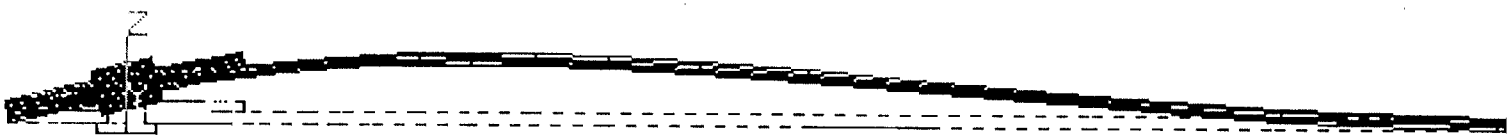

Figure 4.7. Deformed shape of the joint (full view).

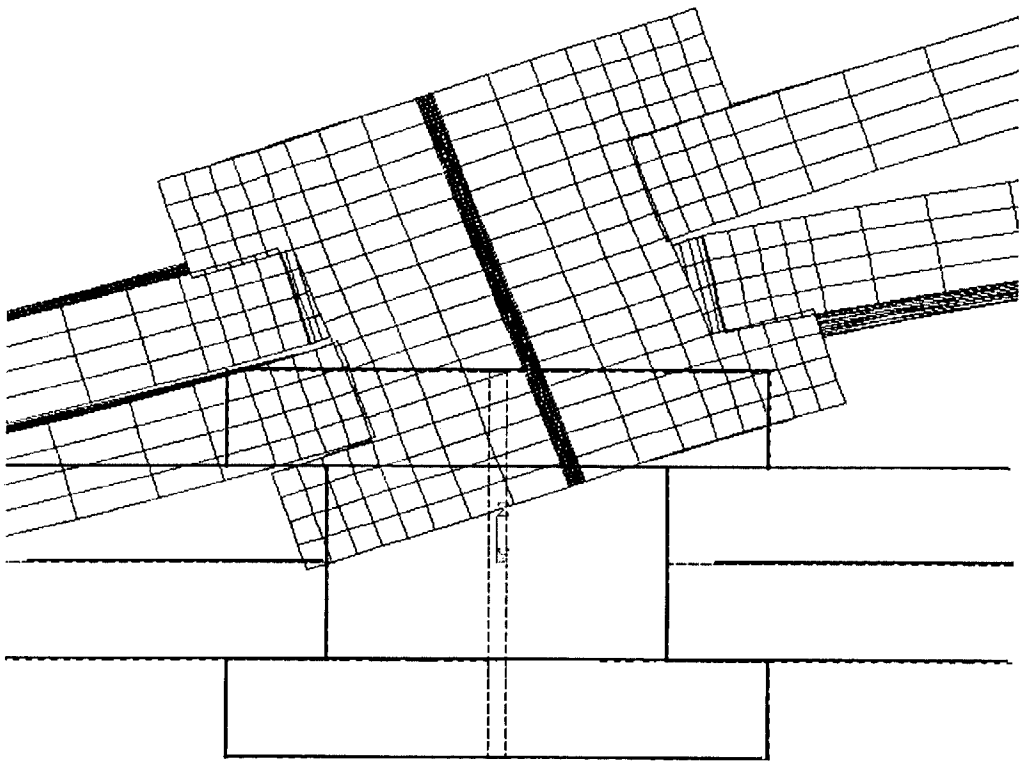

Figure 4.8. Deformed shape of the joint (close-up view).

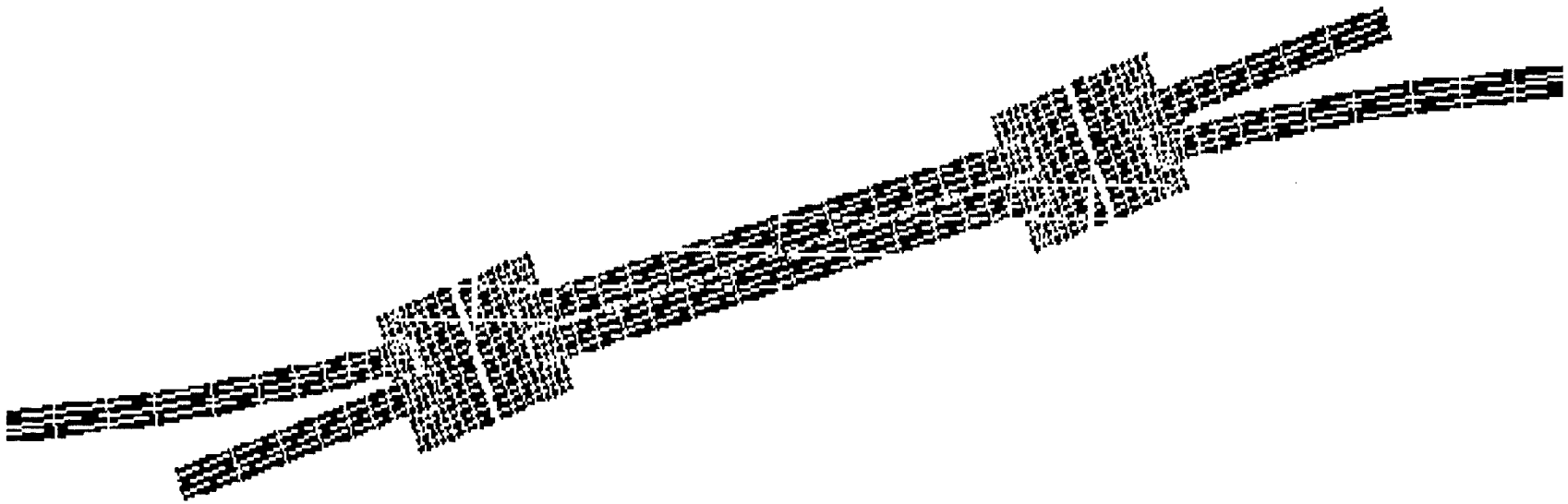

Figure 3.9. Deformed shape of the joint (super imposed image).

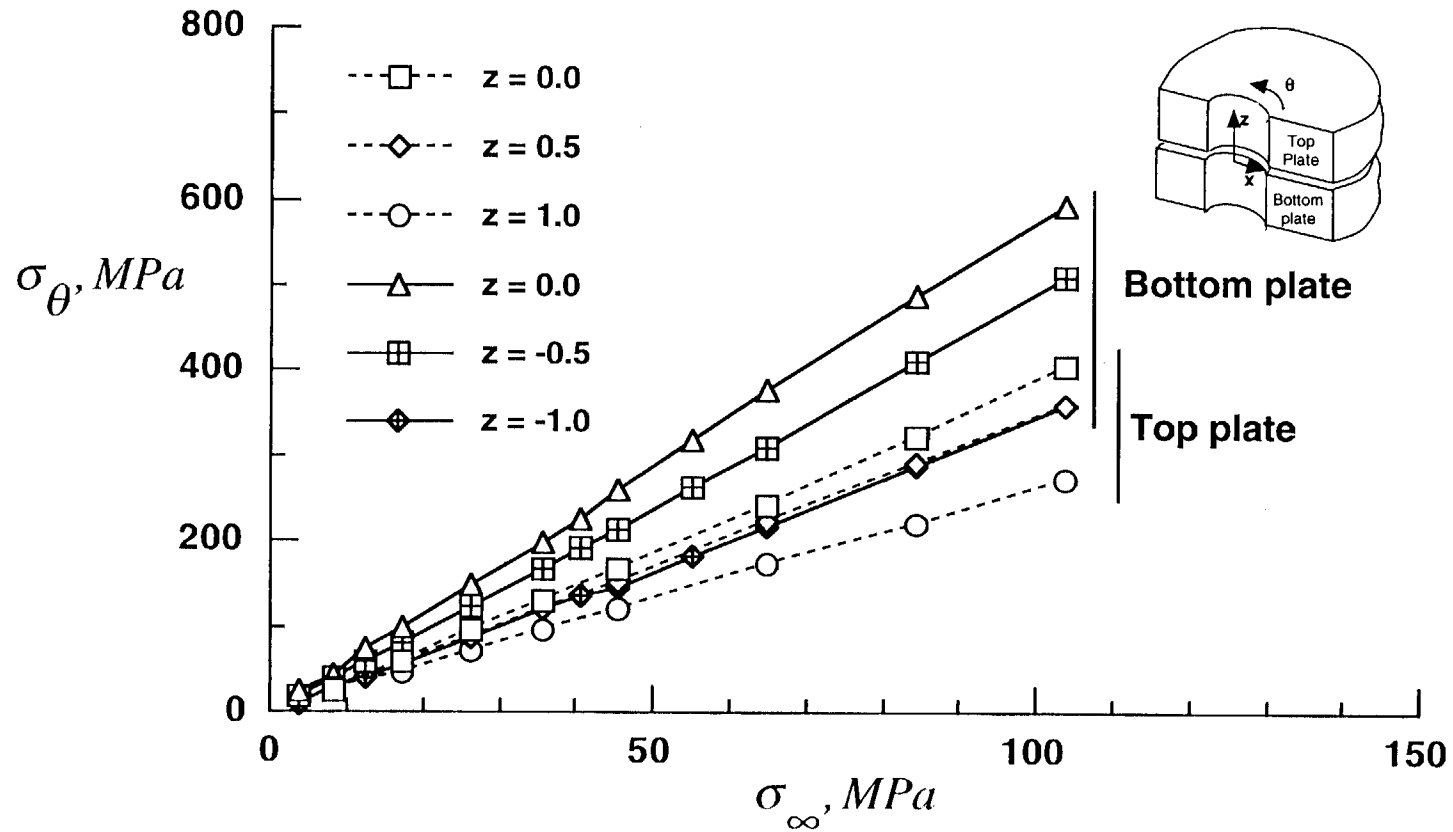

Figure 4.10. Hoop stress vs remote stress for various z values at θ = 90°.

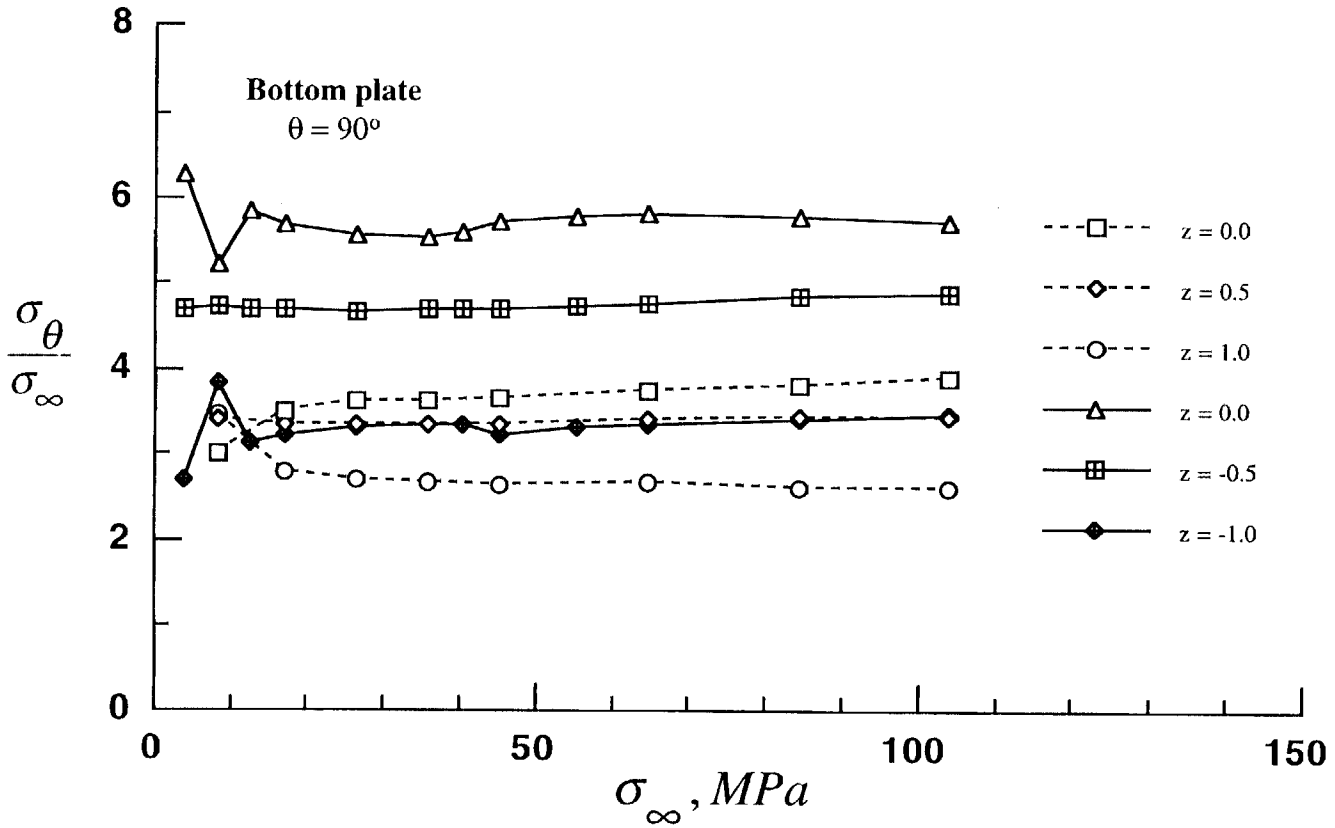

Figure 4.11. Stress concentration vs remote stress for various z values.

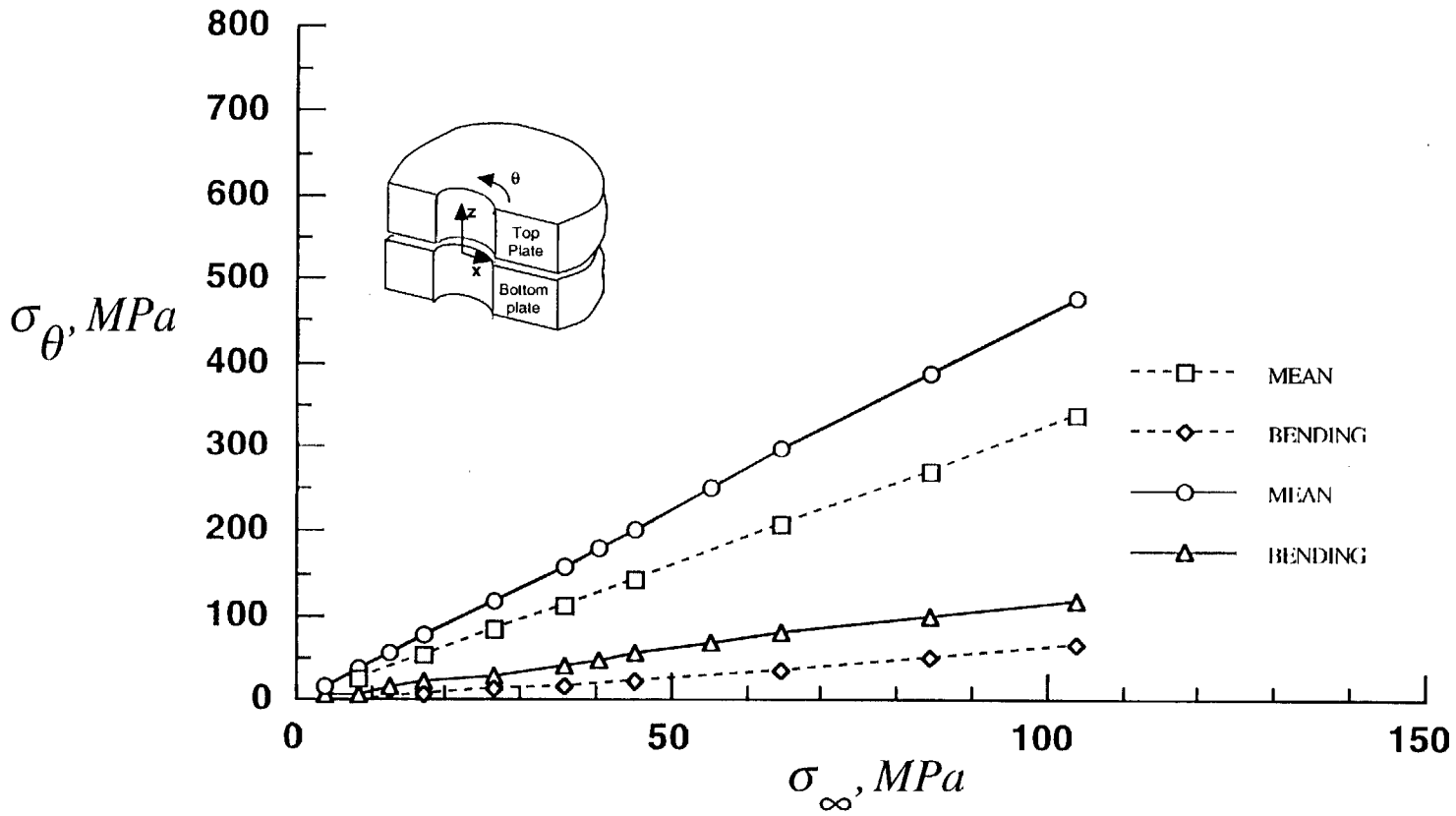

Figure 4.12. Mean and bending stress for bottom plate.

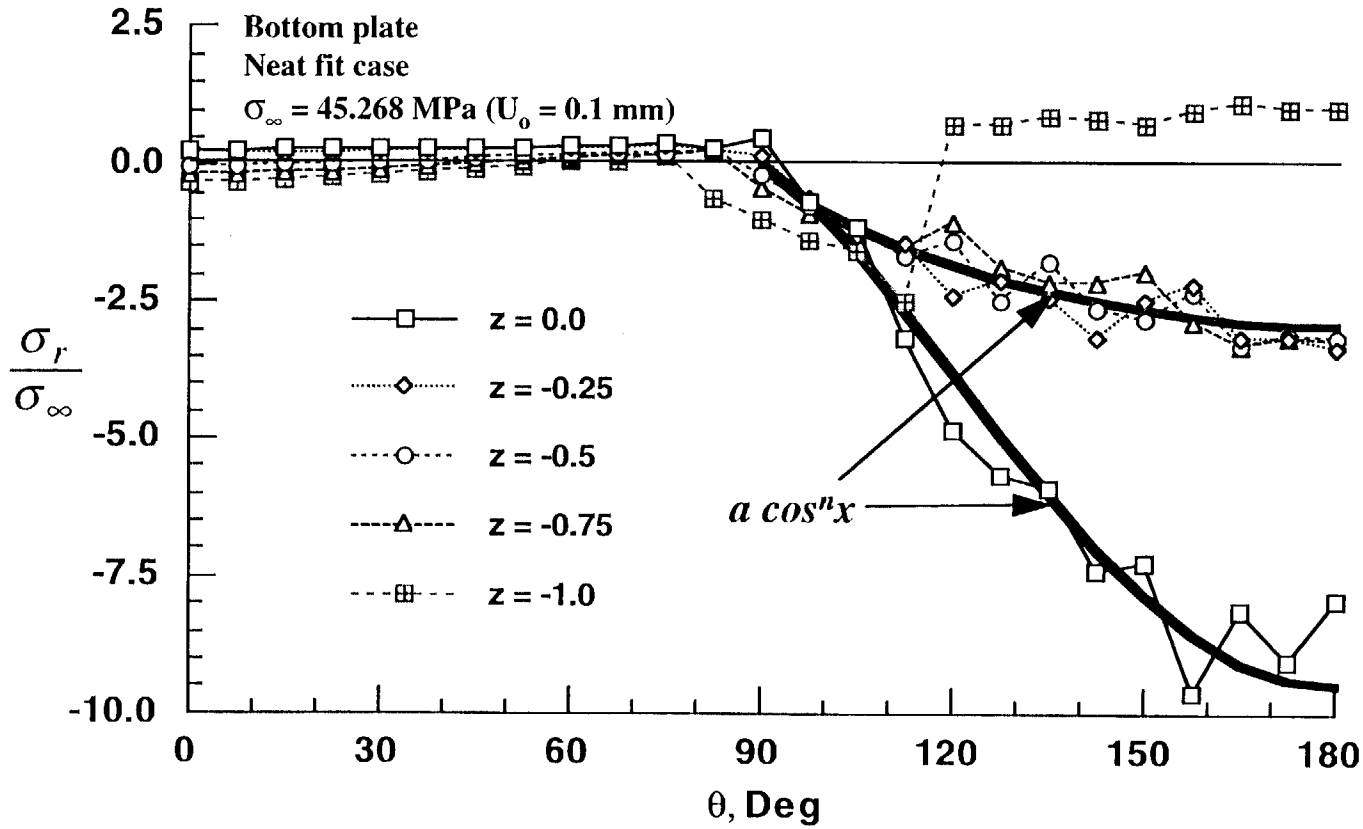

Figure 4.13. Radial stress distribution around the hole boundary (s∞ = 45.27 Mpa).

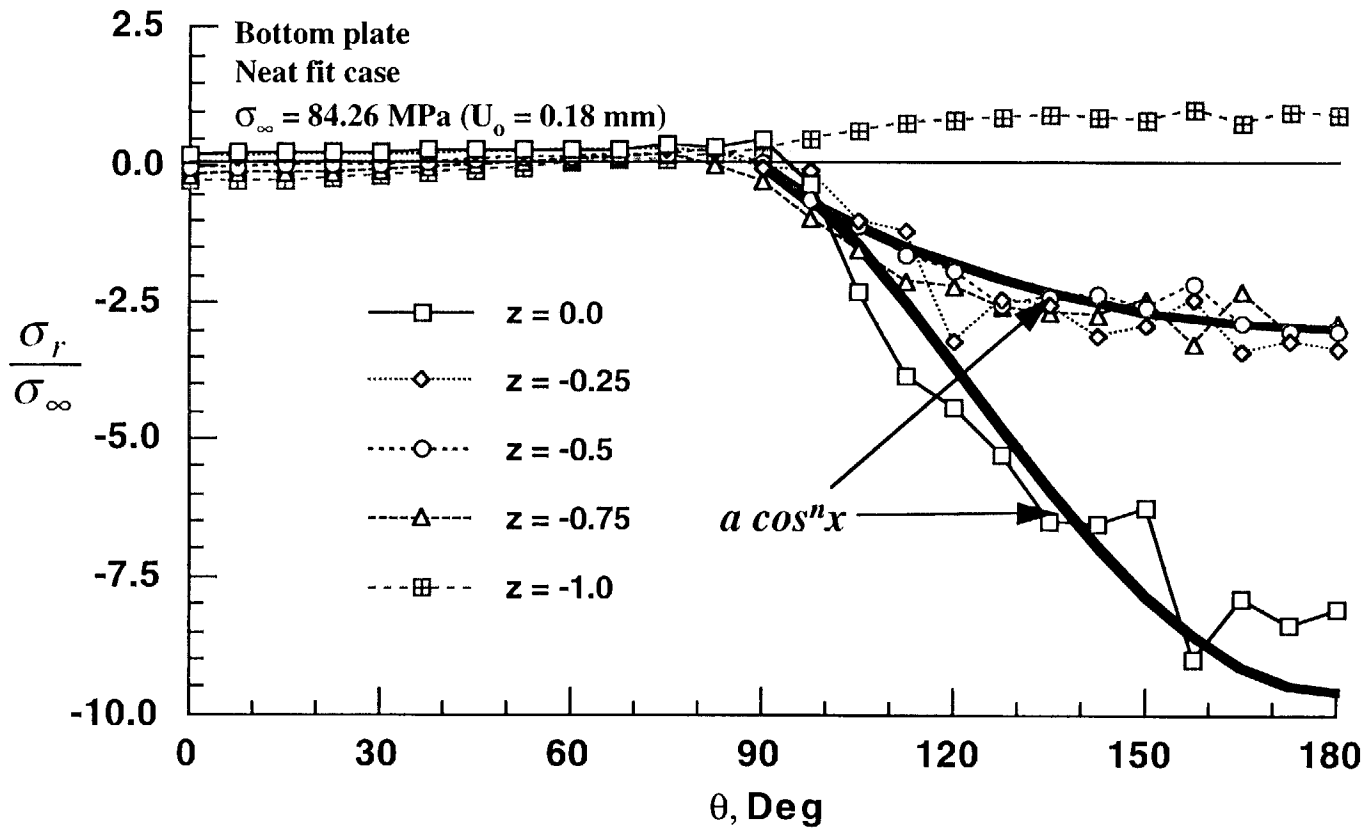

Figure 4.14. Radial stress distribution around the hole boundary (s∞ = 84.26 Mpa).

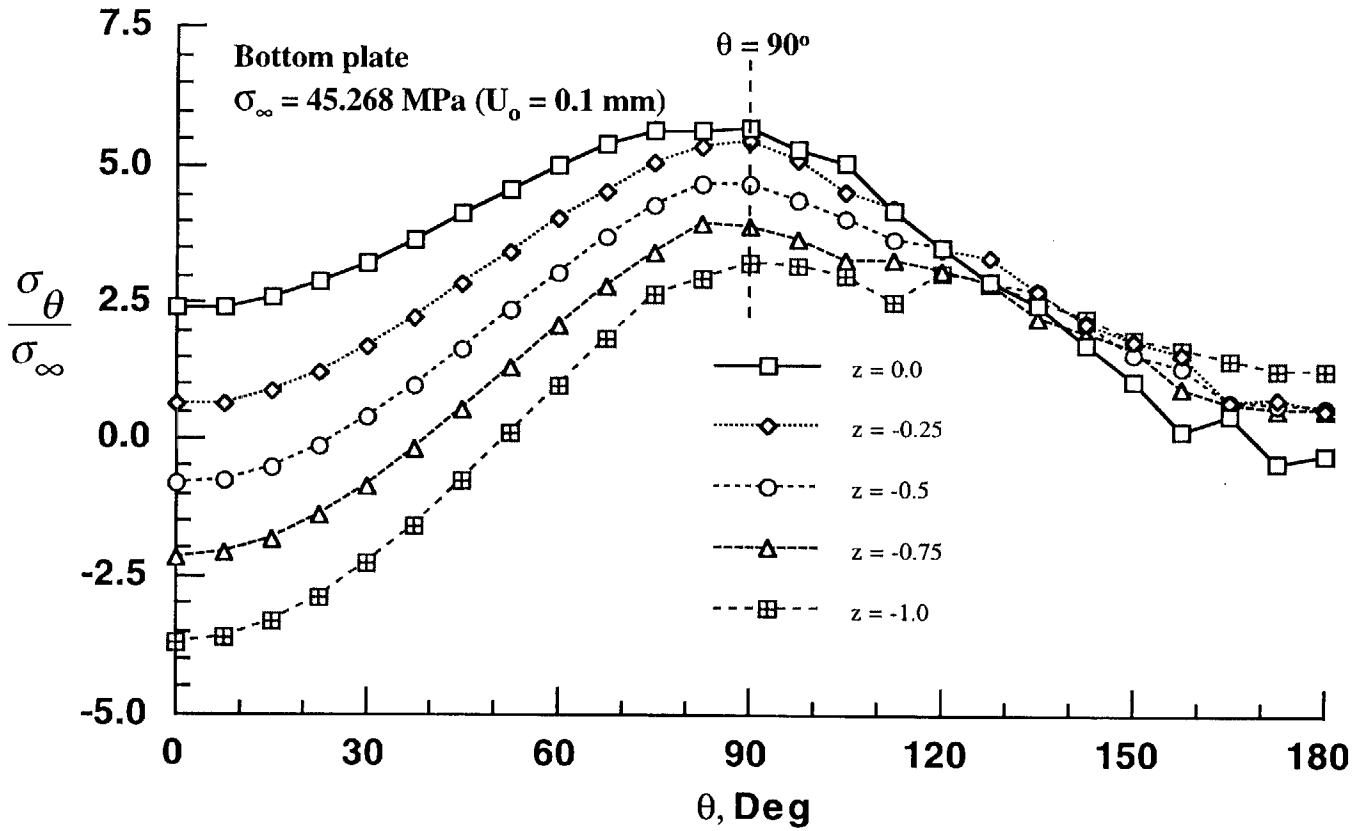

Figure 4.15. Hoop stress distribution around the hole boundary (σ_∞ = 45.27 MPa).

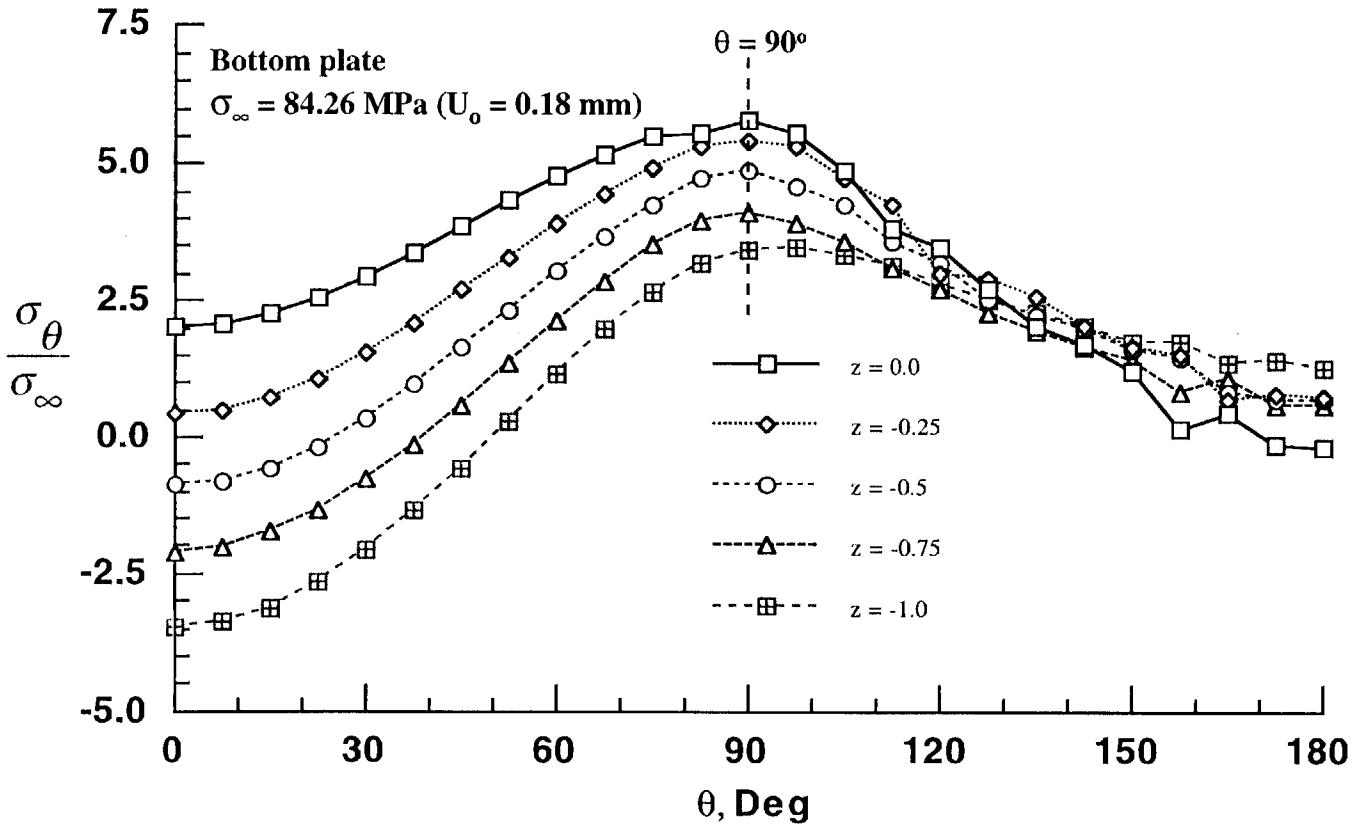

Figure 4.16. Hoop stress distribution around the hole boundary (σ_∞ = 84.26 Mpa).

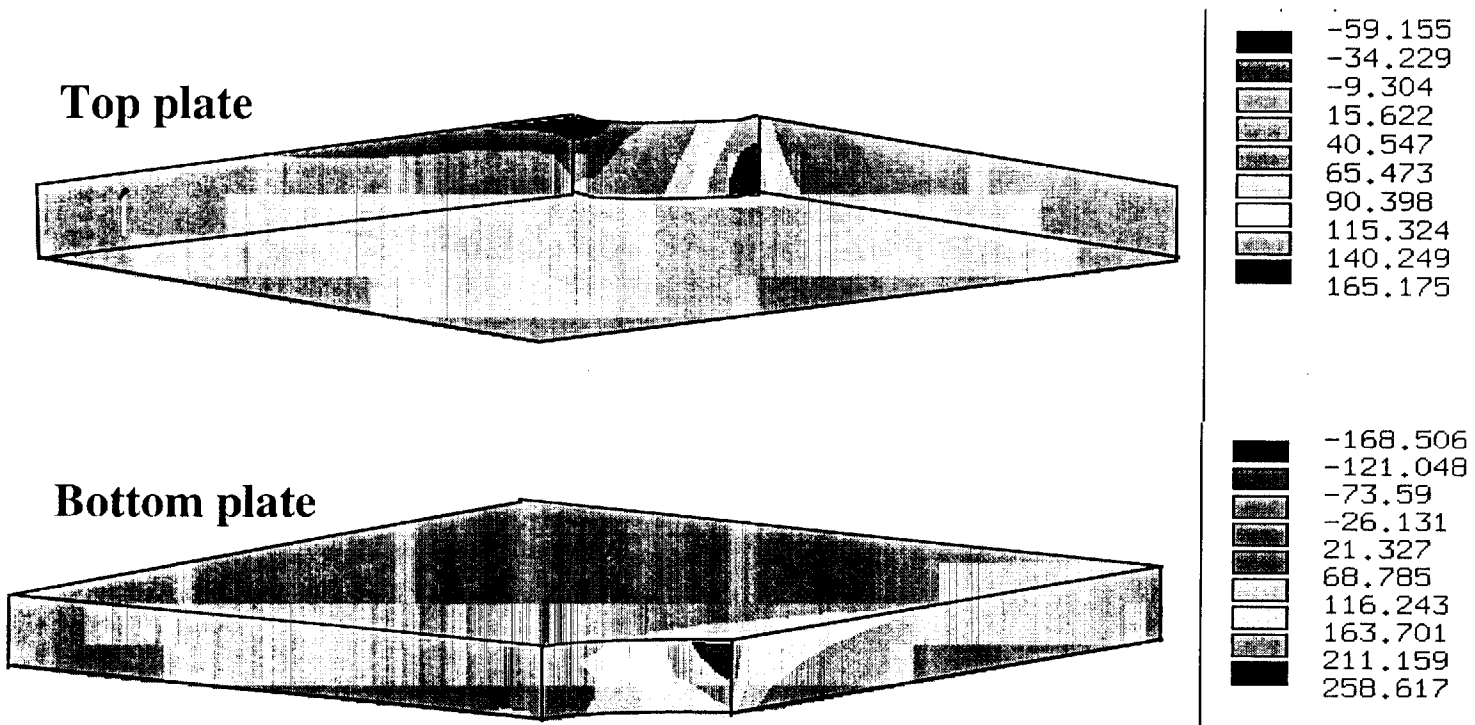

Figure 4.17. Hoop stress contour for a section at $\theta = 90^{o}$

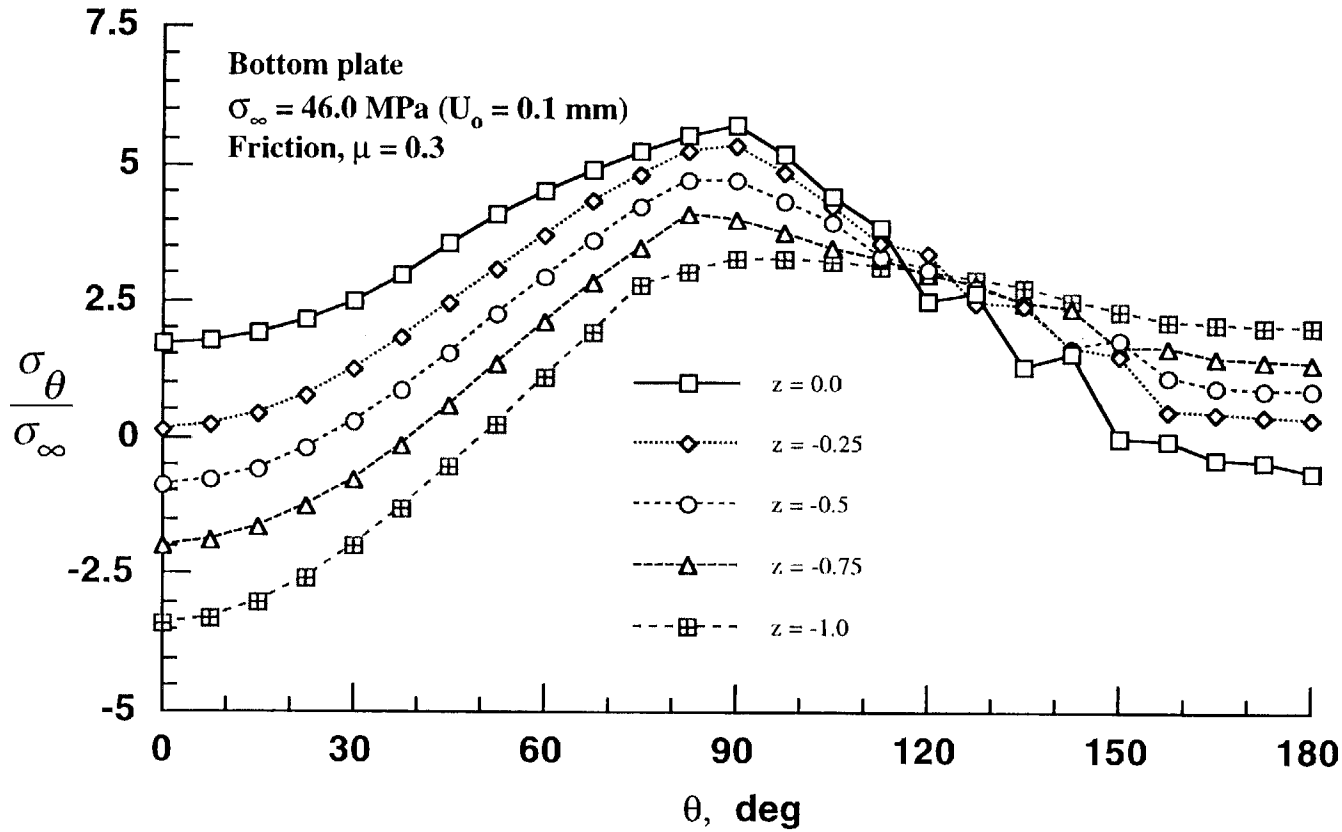

Figure 4.18. Hoop stress distribution at hole boundary (μ = 0.3).

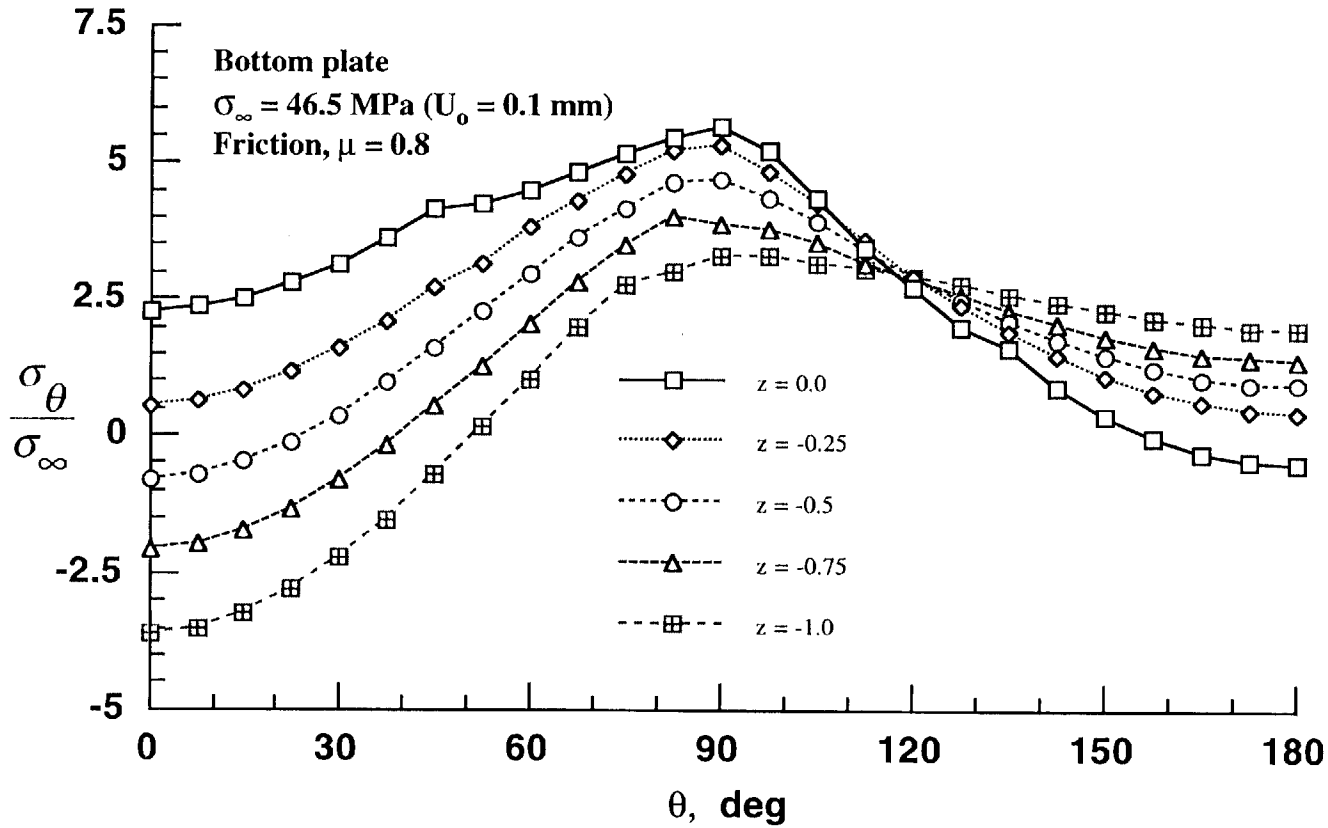

Figure 4.19. Hoop stress distribution at hole boundary (μ = 0.8).

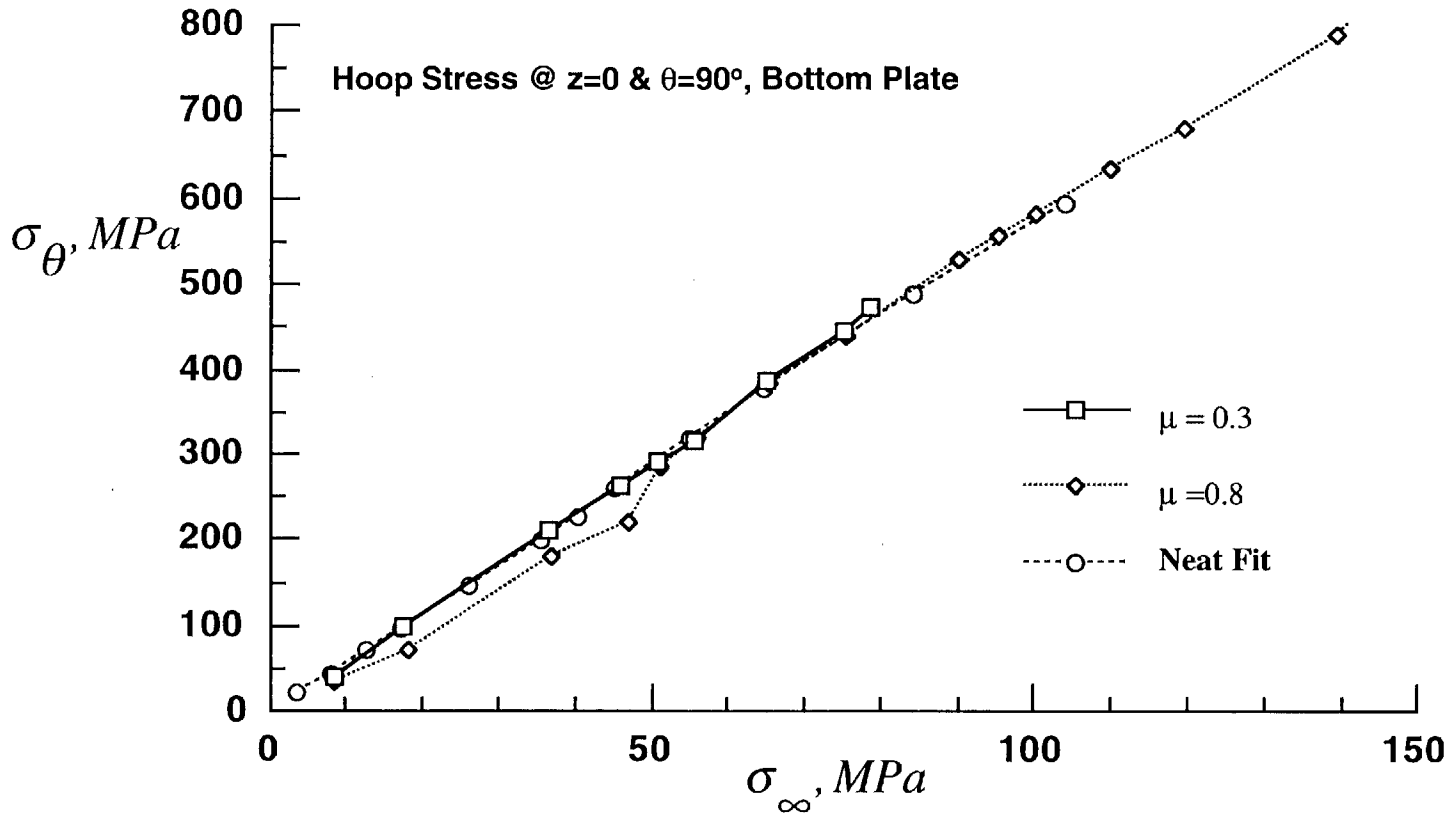

Figure 4.20. Hoop stress vs remote stress for various values of μ.

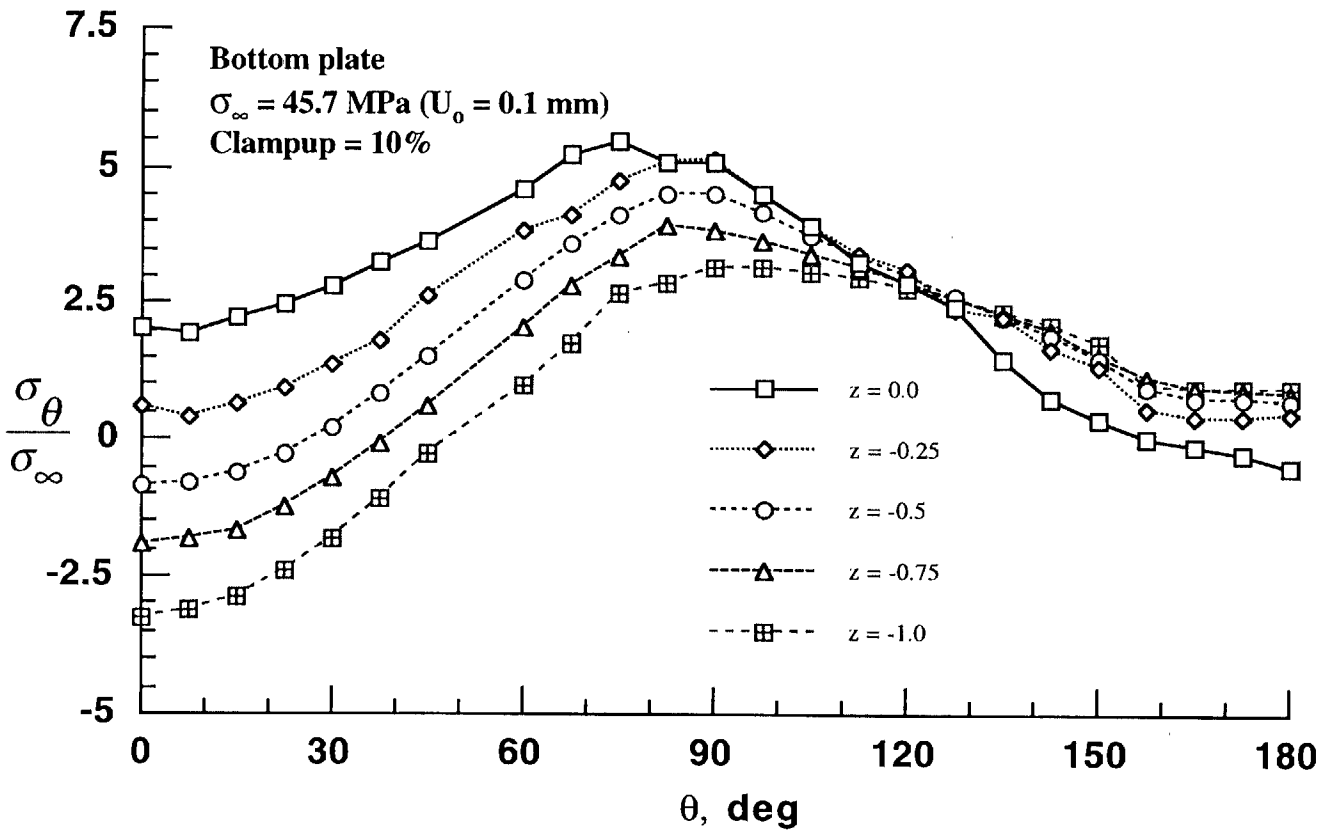

Figure 4.21. Hoop stress distribution around the hole boundary (σ_∞ = 45.7)

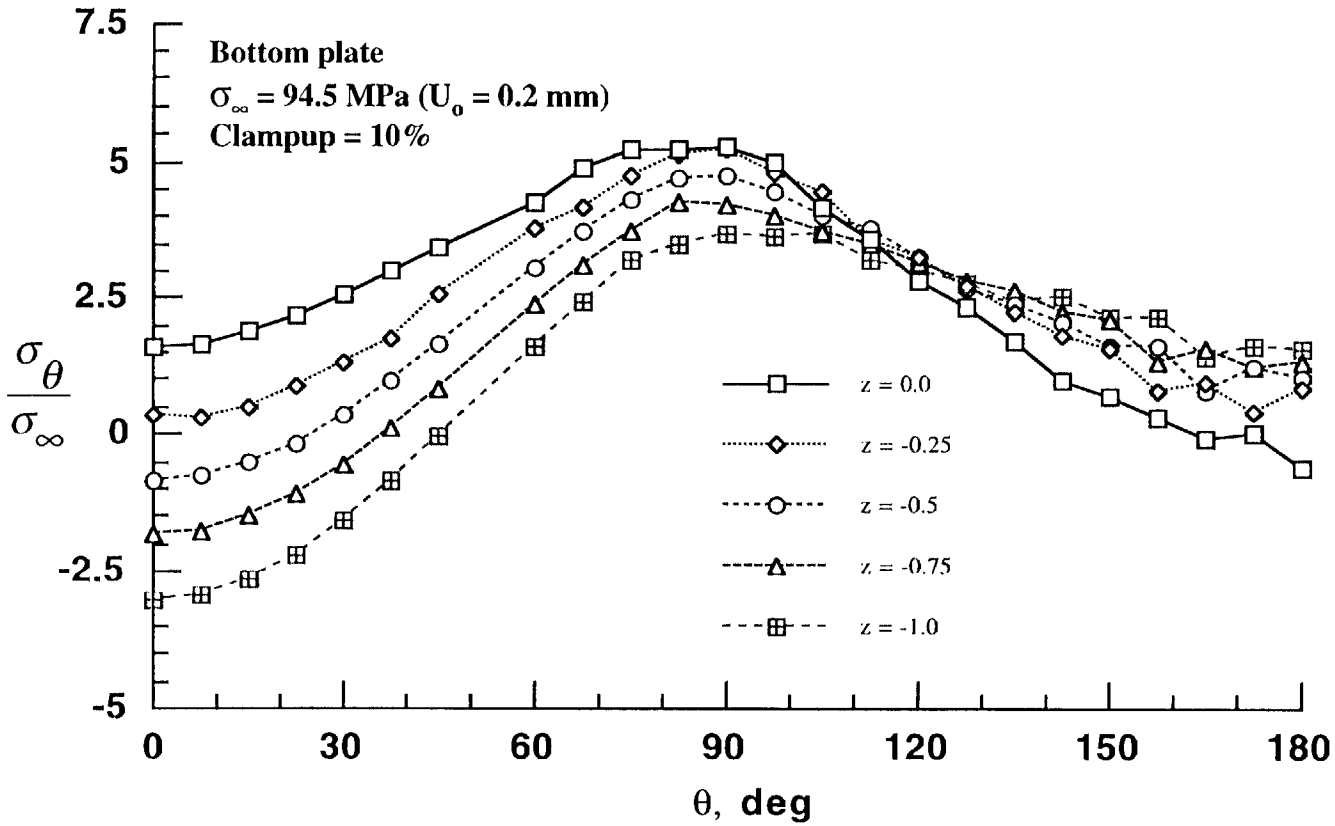

Figure 4.22. Hoop stress distribution around the hole boundary (σ_∞ = 94.5).

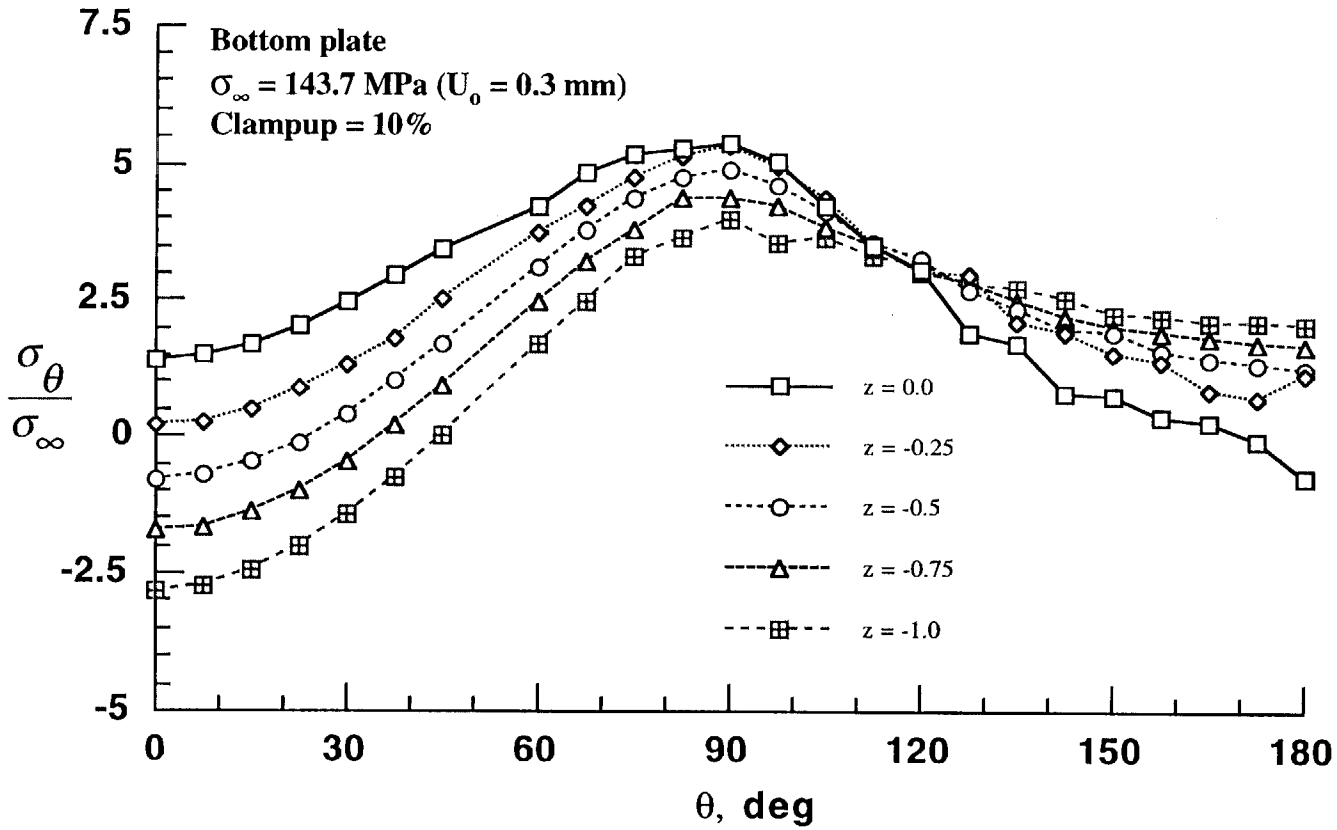

Figure 4.23. Hoop stress distribution around the hole boundary (σ_∞ = 143.7).

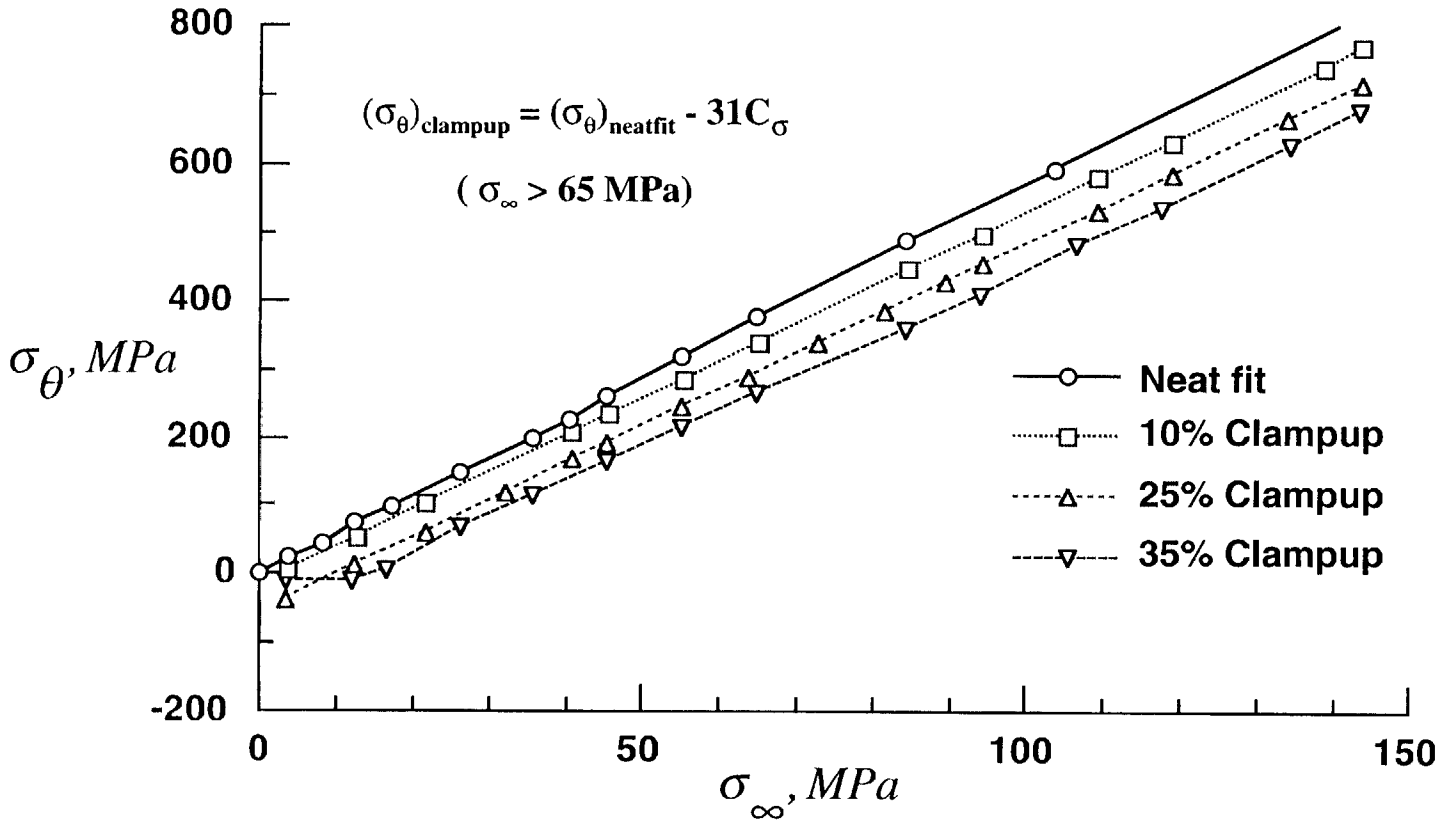

Figure 4.24. Hoop stress vs remote stress at z = 0 and θ = 90° for different clampup

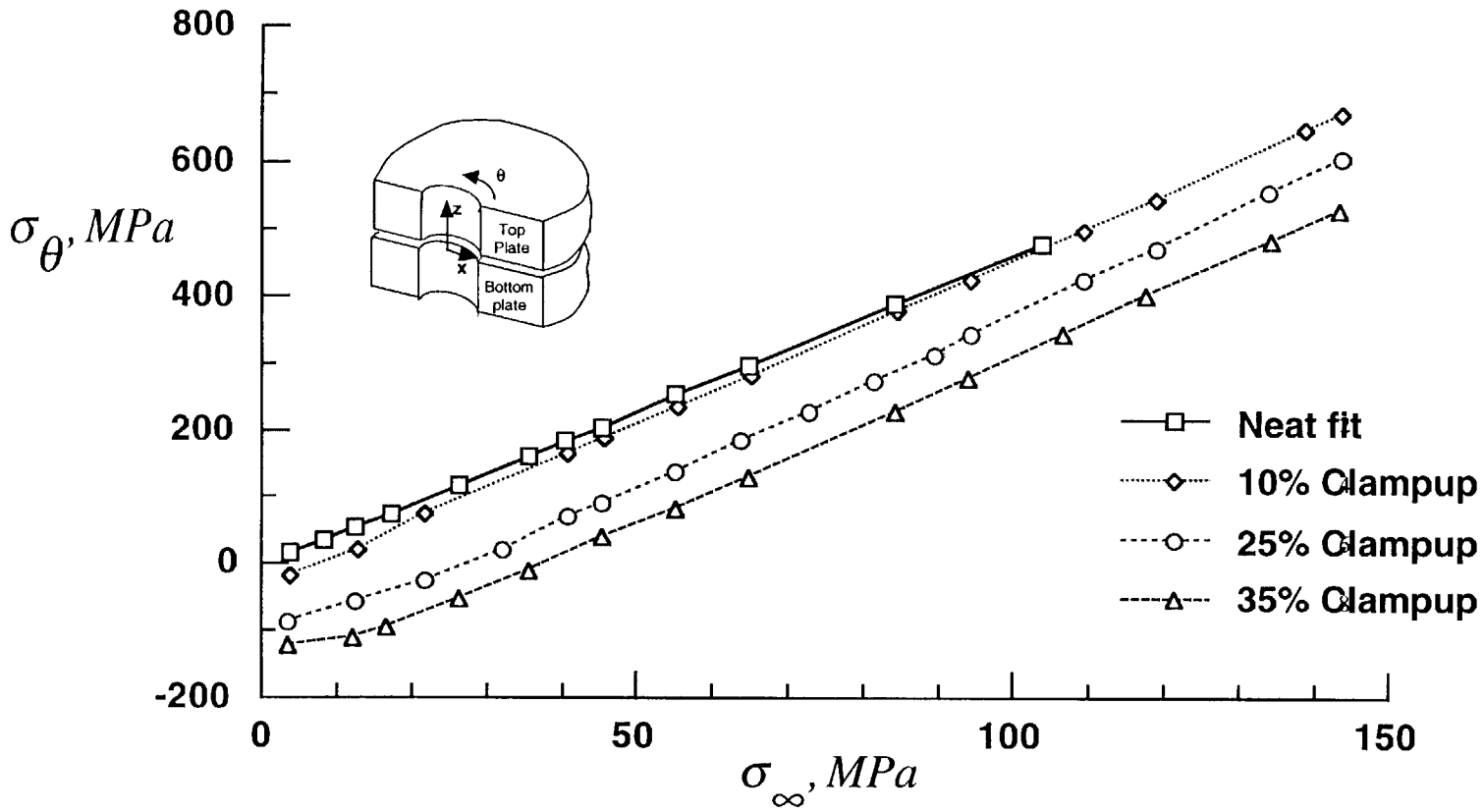

Figure 4.25. Membrane stress for bottom plate at θ = 90°.

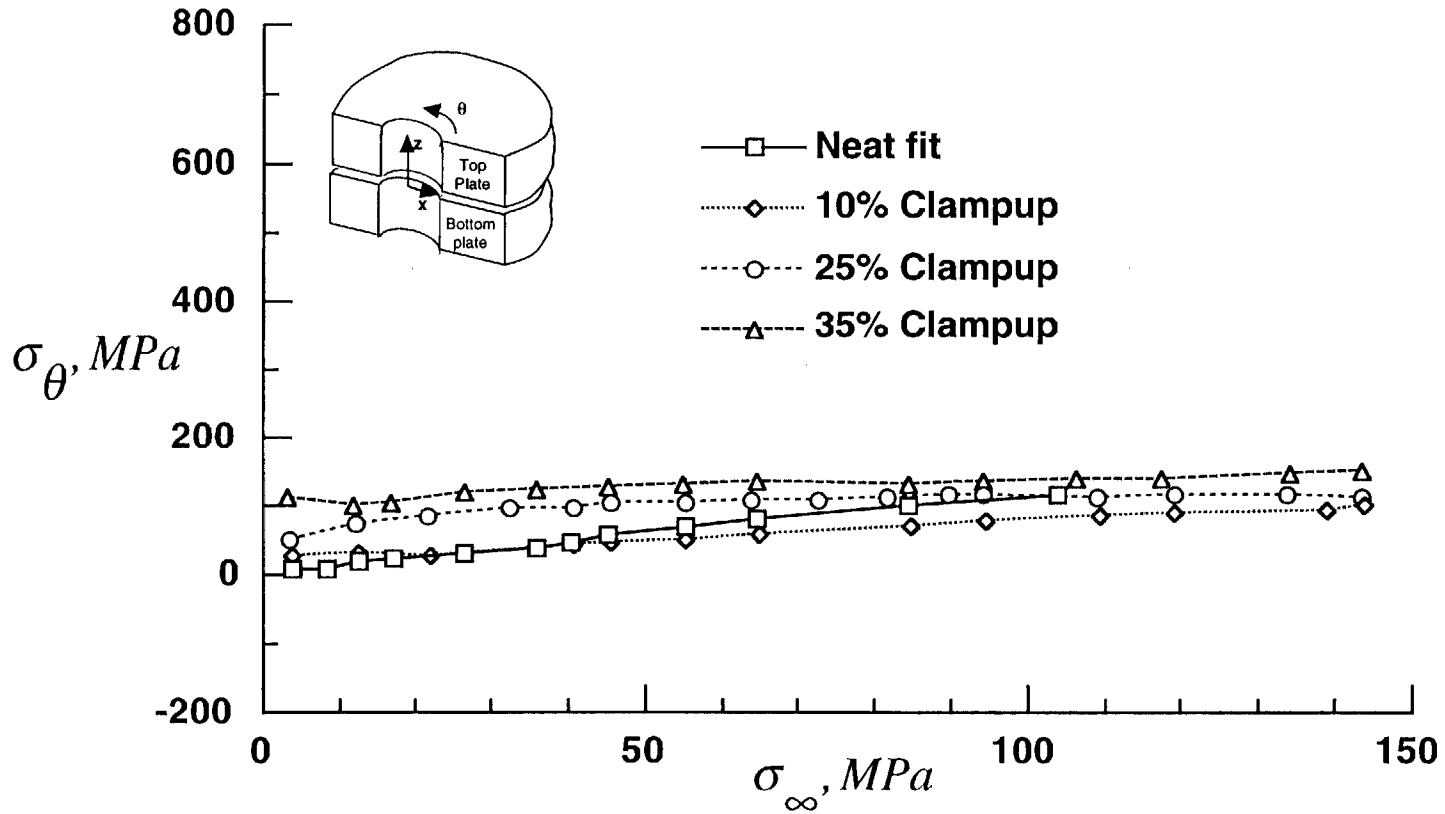

Figure 4.26. Bending stress for bottom plate at θ = 90°.

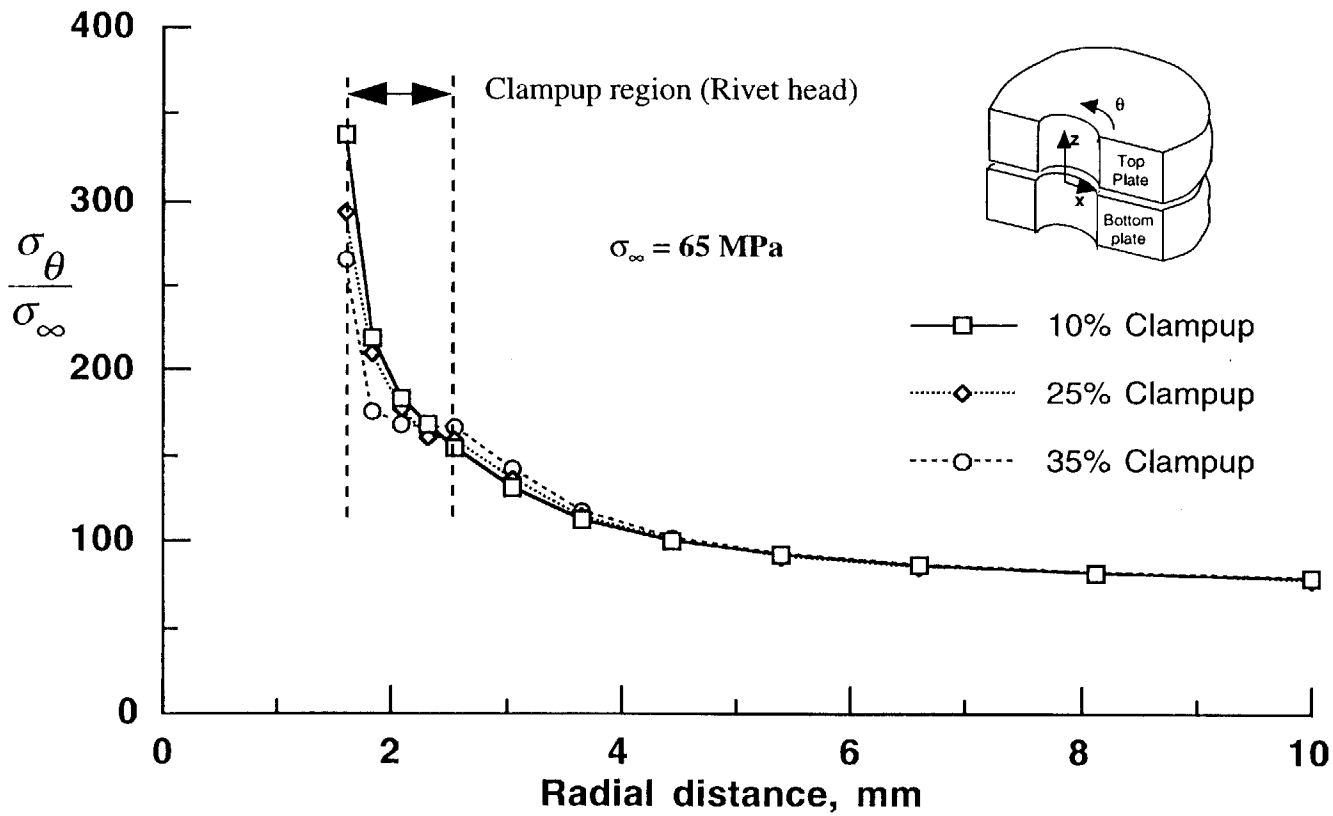

Figure 4.27(a). Variation of hoop stress in radial direction at θ = 90° and z = 0.

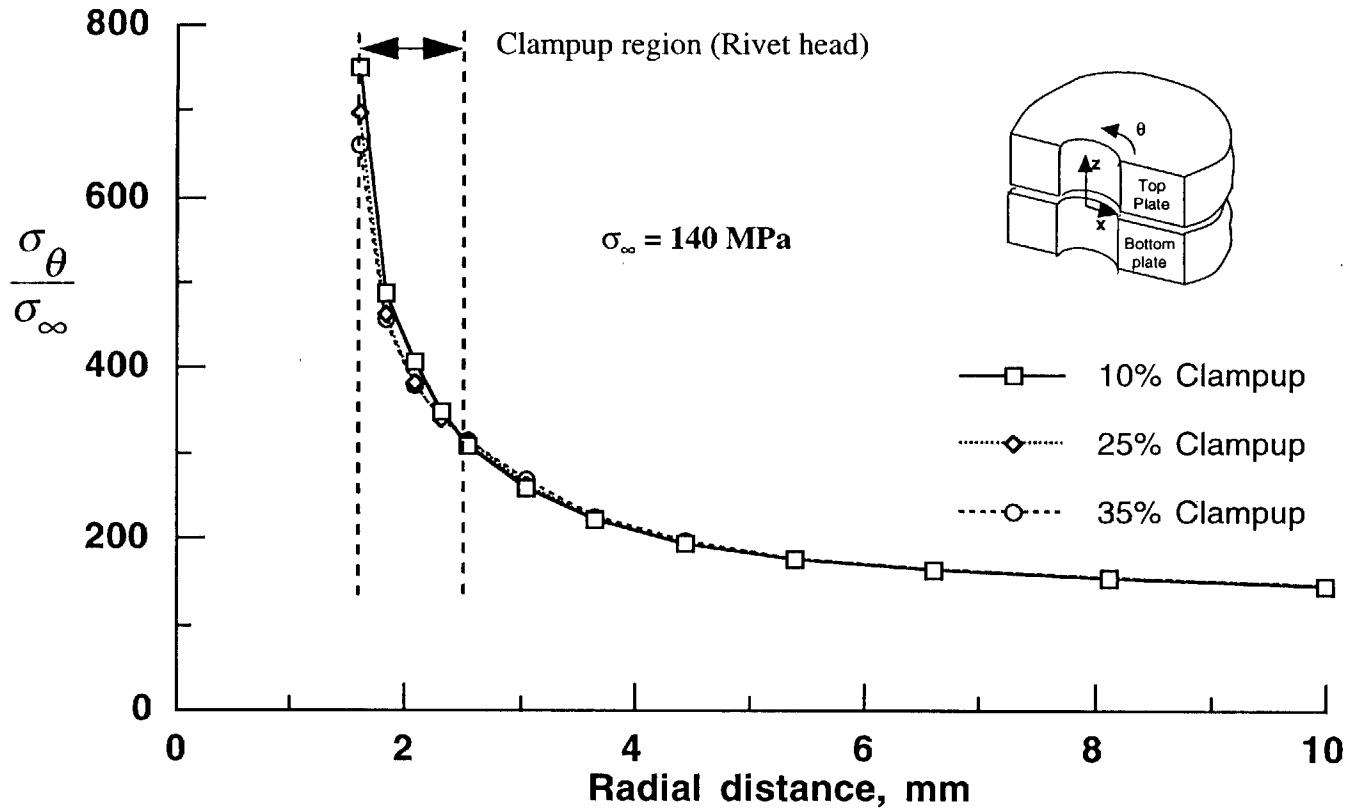

Figure 4.27(b). Variation of hoop stress in radial direction at θ = 90° and z = 0.

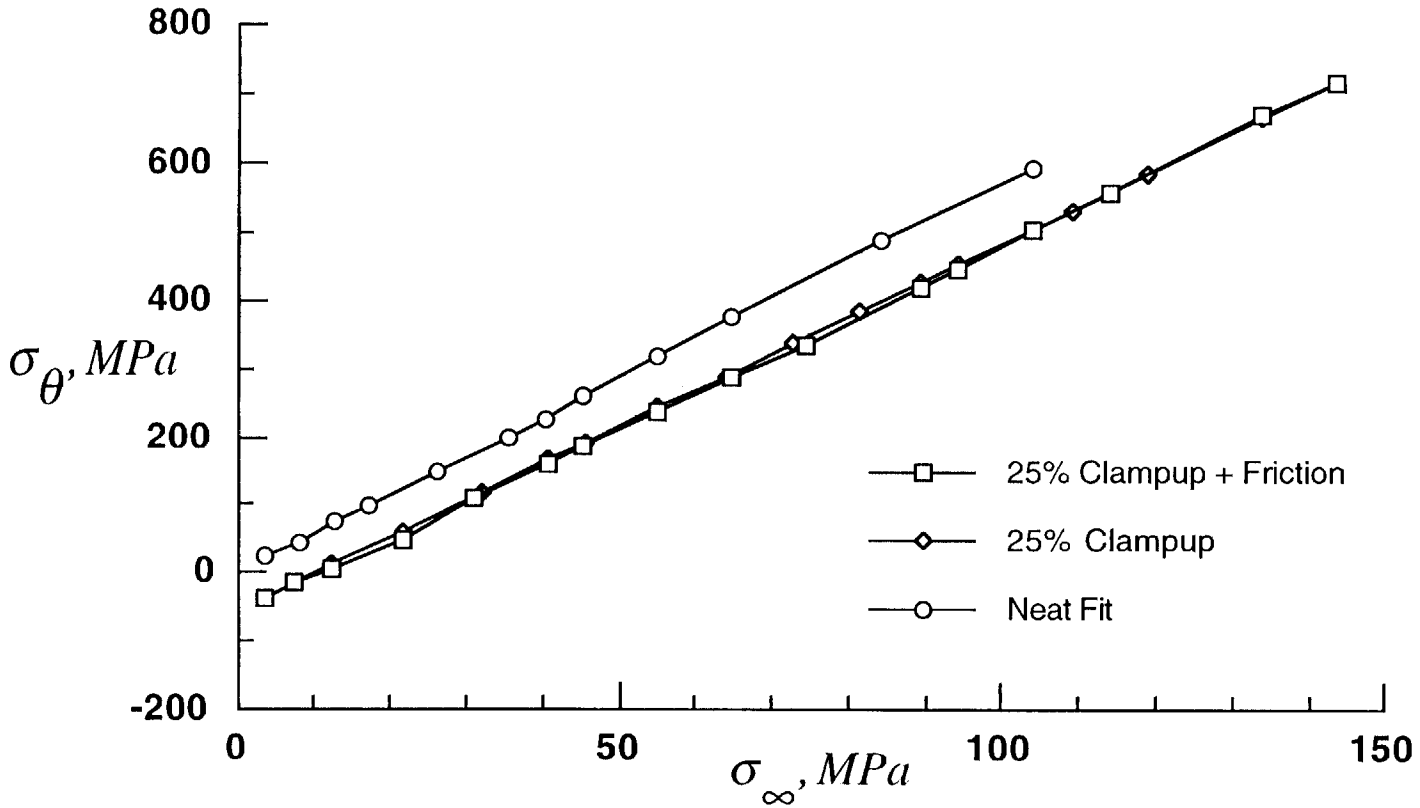

Figure 4.28. Clampup + friction @ θ = 90 and z = 0 of bottom plate.

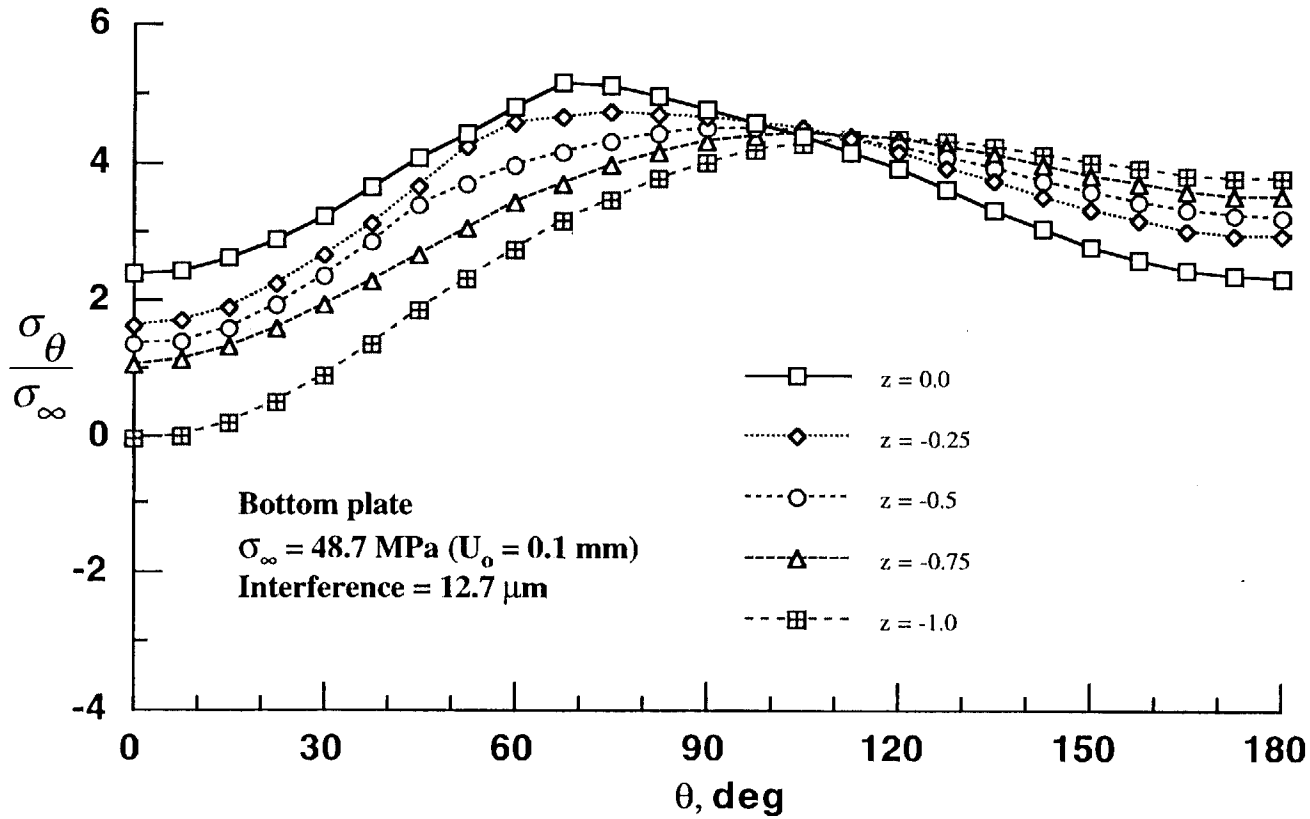

Figure 4.29. Hoop stress distribution around the hole boundary (σ_∞ = 48.7 MPa).

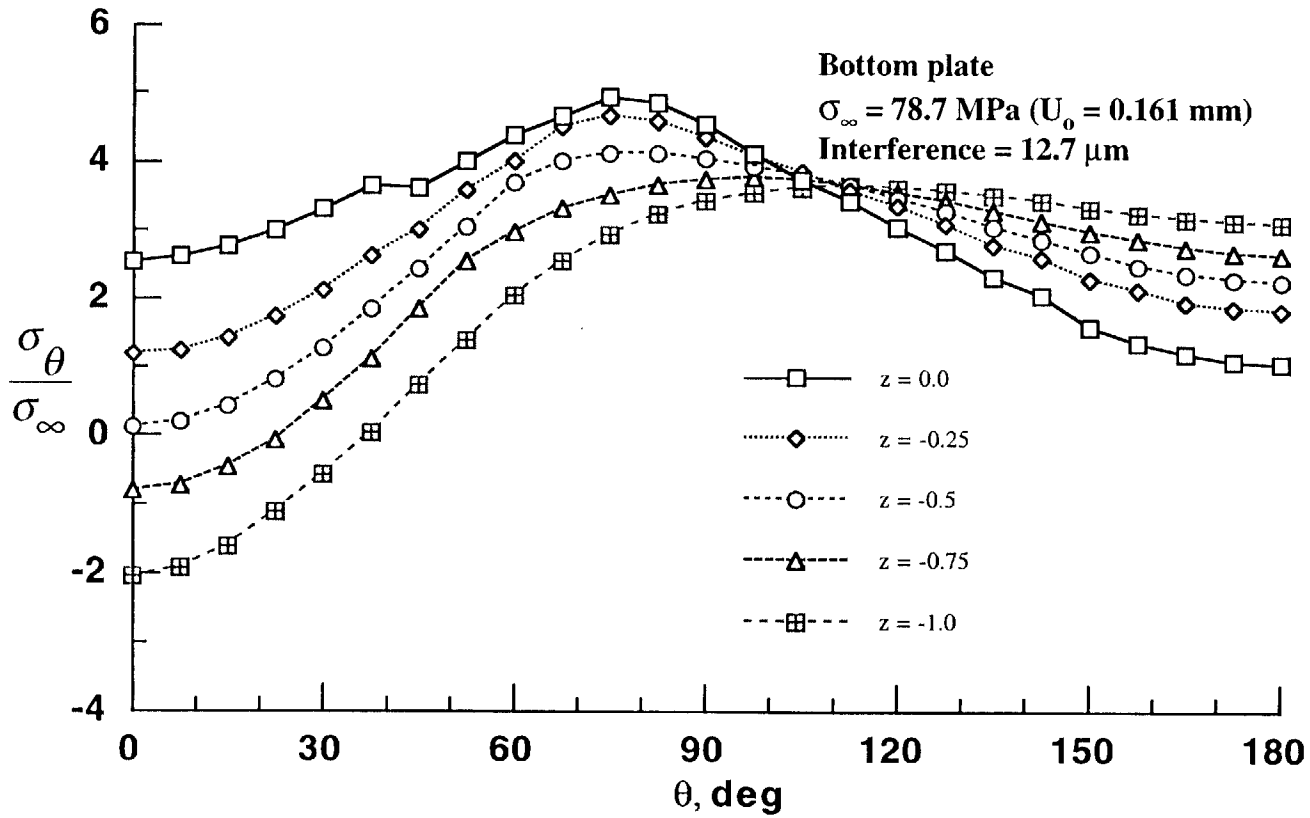

Figure 4.30. Hoop stress distribution around the hole boundary (σ_∞ = 78.7 MPa).

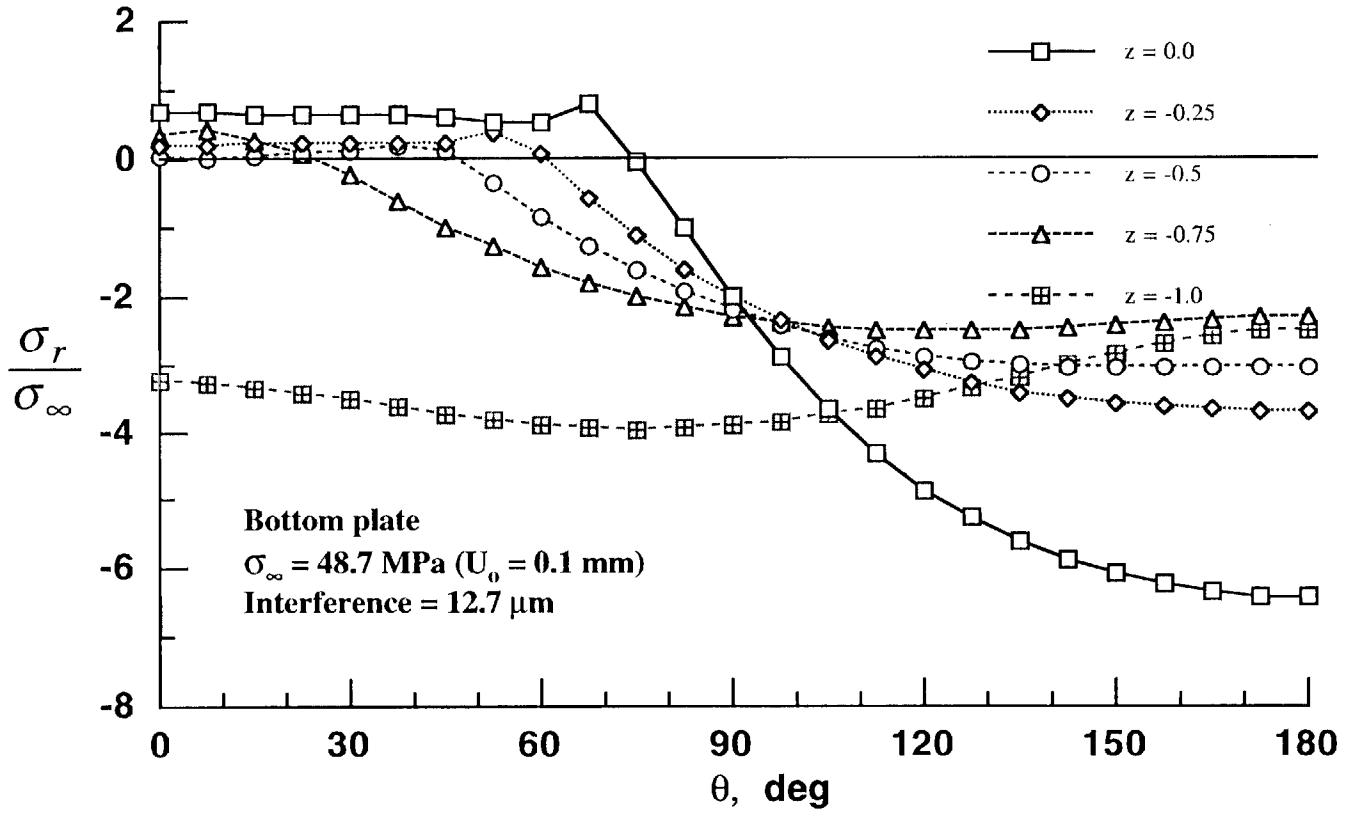

Figure 4.31. Radial stress distribution around the hole boundary (σ_∞ = 48.7 MPa).

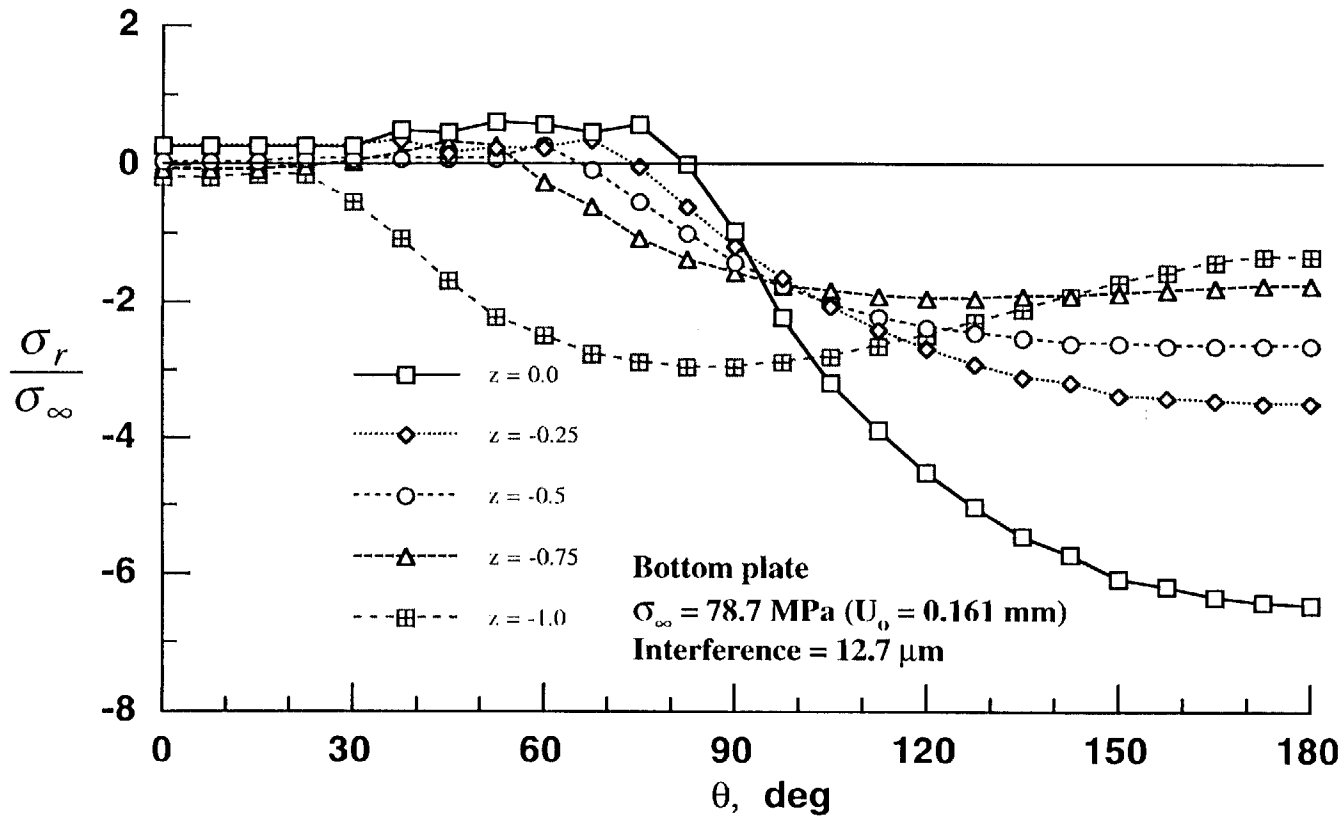

Figure 4.32. Radial stress distribution around the hole boundary (σ_∞ = 78.7 MPa).

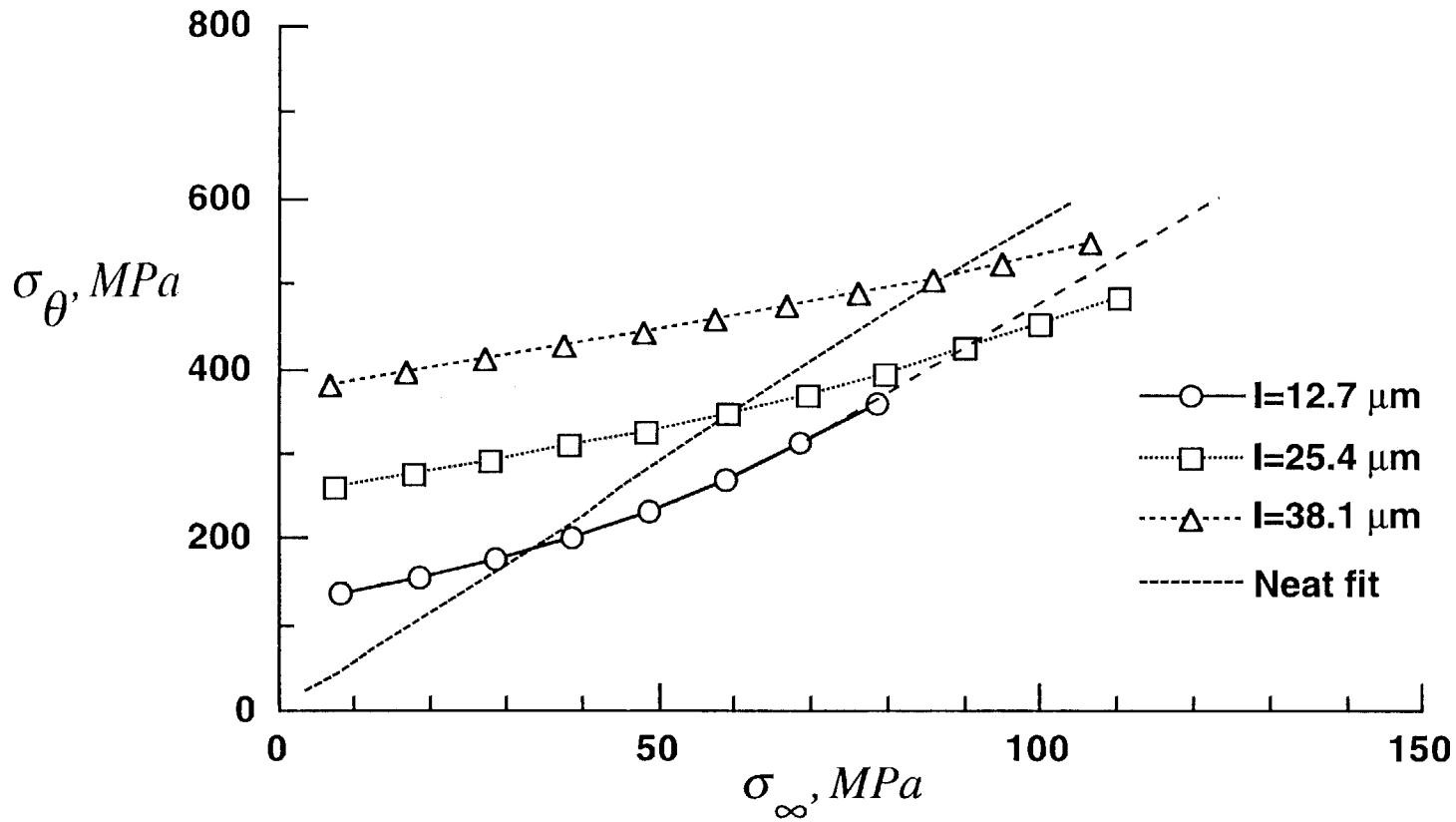

Figure 4.33. Hoop stress vs remote stress at z= 0 and θ = 90°.

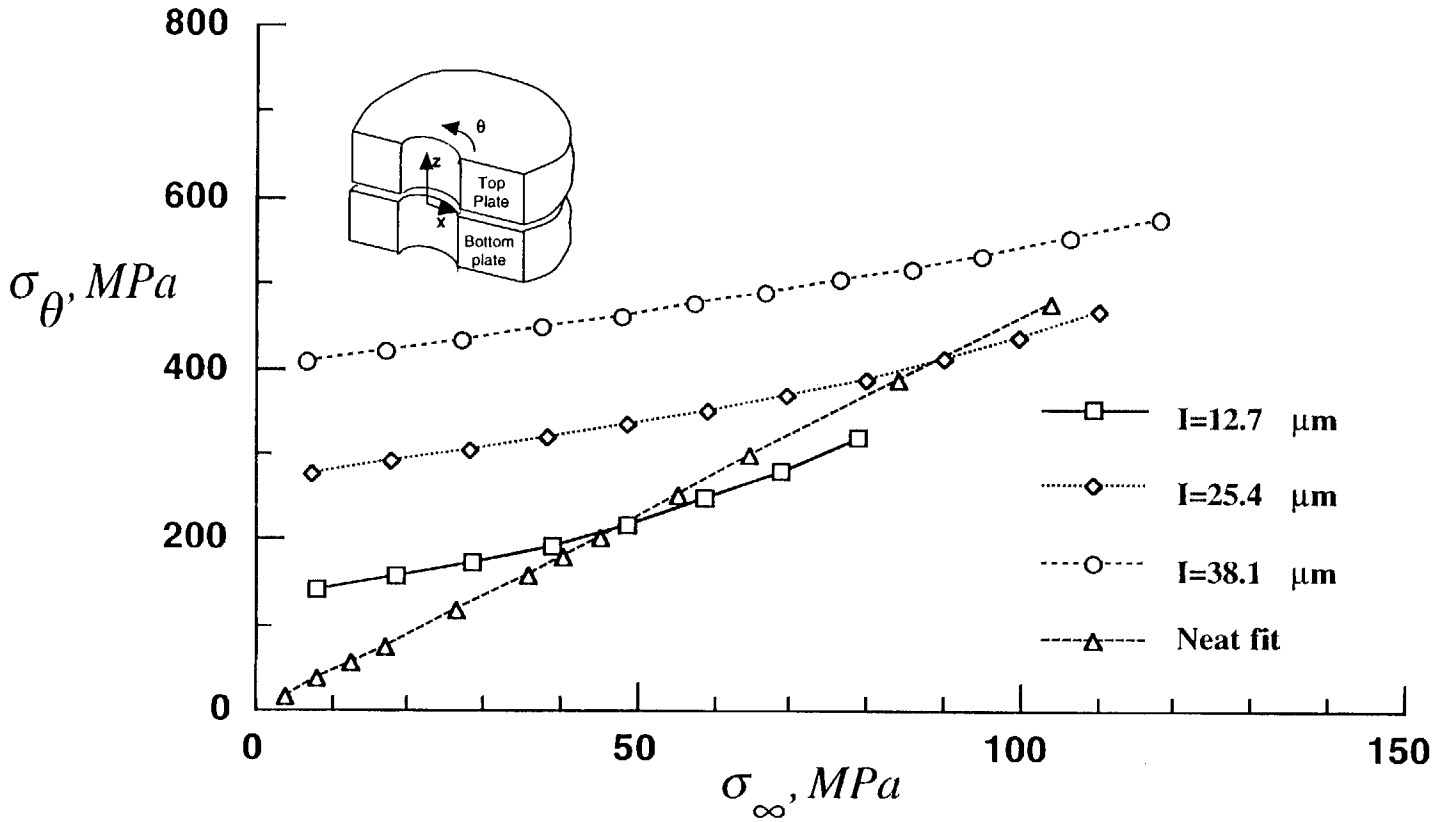

Figure 4.34. Membrane stress vs remote stress at θ = 90°.

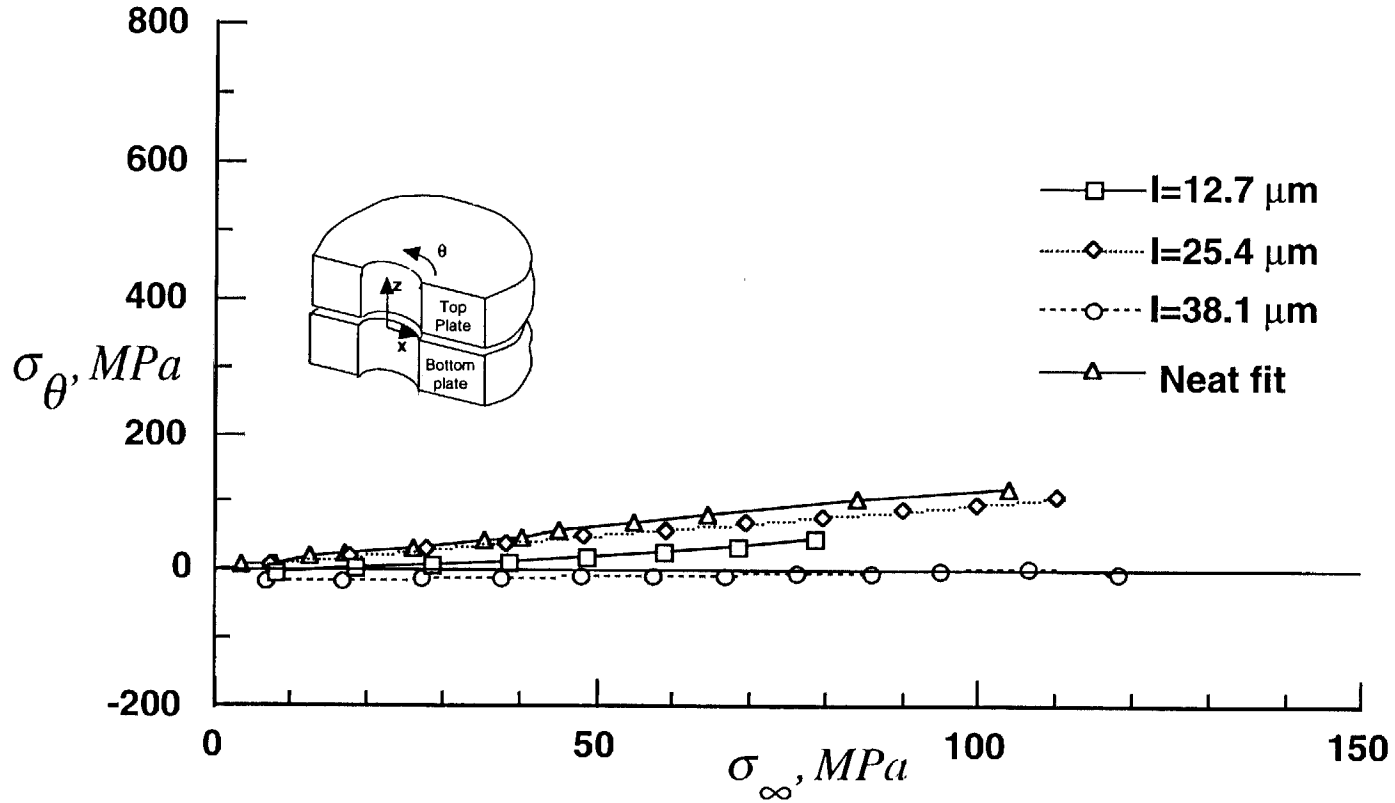

Figure 4.35. Bending stress vs remote stress at θ = 90°.

5. ELASTIC - PLASTIC ANALYSIS OF TWO - RIVET SINGLE LAP JOINT

5.1 Introduction

In the previous section, elastic analysis of the two - rivet joint was conducted. The local stresses at the rivet hole have exceeded the material yield stress. To investigate the redistribution of stresses due to plastic deformation, an elastic plastic analysis of the neat fit case was conducted. In this section results of this analysis are presented. The material was modeled as multi-linear stress - strain response, with an yield strength of 270 MPa and ultimate strength of 425 MPa. The joint configuration shown in Figure 1.2 and finite element mesh used is shown in Figure 4.5.

5.2 Material modeling

In this analysis the rivet material was assumed to be elastic and the plate material to be elastic - plastic, because the plastic deformation of the plate is of interest. The multilinear isotropic hardening stress - strain response was used to model the plate material. The stress - strain curve is shown in Figure 5.1. The von Mises yield criteria and incremental plasticity theory based on the associated flow rule was used in the analysis. The von Mises criteria for a three dimensional stress state in terms of the six Cartesian stress components is given by

$$\sigma_{eff} = \frac{1}{\sqrt{2}}\sqrt{\left(\sigma_x - \sigma_y\right)^2 + \left(\sigma_y - \sigma_z\right)^2 + \left(\sigma_z - \sigma_x\right)^2 + 6\left(\tau_{xy}^{\ 2} + \tau_{yz}^{\ 2} + \tau_{zx}^{\ 2}\right)}$$

Yielding would occur when,

$\sigma_{eff} \geq \sigma_{ys}$

where, σ_{eff} is the effective (von Mises) stress and σ_{ys} is the current uniaxial yield stress of the material. Initially, σ_{ys} is the material yield stress (270 MPa) and as the material plastically deforms, the yield stress changes for isotropic hardening. In isotropic hardening, the yield surface expands in size as the plastic strains develop as shown in Figure 5.2.

5.3 Analysis

The plate was loaded incrementally by remote axial displacement u_o (see Figure 4.2). To follow the effective stress - strain response as closely as possible, small load increments were chosen. The initial displacement increment was 0.01 mm (3.92 MPa) and the subsequent displacement increments varied between 0.01 and 0.02 mm. The analysis was carried to a maximum remote displacement of about 0.22 mm. The force convergence criteria was used. That is the maximum out of balance residual force is about 1 to 10% the total incremental load for that load step.

The analysis was conducted using a commercial finite element code ANSYS. The full Newton-Raphson method with updated tangent stiffness matrix and adaptive descent was used to solve this non-linear problem. Each analysis case took 9 CPU hours on DEC Alpha 255 computer.

5.4 Results and Discussions

The analysis was conducted for only one case. that is the neat fit (no friction, no clampup and no interference) joint subjected to remote tensile loading. Only important results are presented here.

Figure 5.3 show the progressive development of the plastic zone with remote loading on the hole boundary of the bottom plate. As can be seen yielding first occurs at $\theta = 180^o$, where the rivet bears against the hole and then it progresses towards $\theta = 90^o$. The

plate material starts to yield at around σ_∞ = 45.5 MPa (ux = 0.1) at z = 0 and θ = 180°. This yielding is due to the high compressive bearing stresses developed between the rivet and the plate. However compressive stresses are not critical in causing crack initiation or propagation. By the time remote loading reached 55.1 MPa, nearly half the rivet hole had yielded and at σ_∞ = 97.7 MPa, nearly 75% of the hole had yielded. At θ = 90°, the yielding was due to high tensile stresses. Hence, the crack initiation and propagation is highly probable at θ = 90°.

Figures 5.4 through 5.6 show the variation of hoop stress around the hole boundary for three values of σ_∞.. All stresses were normalized by the remote stress (σ_∞.). With increasing load levels the stress concentration drops, for example from 5.4 (elastic) to around 3.45 (plastic) for σ_∞. = 97.7 MPa. Also, the peak tensile stresses are more evenly spreadout. Table 5.1 lists the maximum hoop stress and its location and comparison of maximum hoop stress with σ_θ at θ = 90° and z = 0. In the elastic region the maximum stress location was at θ = 90° and z = 0. After the material yields the maximum hoop stress location shifts to 75°. The difference between maximum hoop stress and σ_θ at θ = 90° and z = 0 is less than 1.5 % except at σ_∞. = 50.2 MPa. Therefore, we can conclude that σ_θ at θ = 90° and z = 0 are same the maximum hoop stress.

Figure 5.7 shows the plot of σ_θ at θ = 90° and z = 0 versus the remote stress (σ_∞) for elastic and elastic-plastic cases. The two results are almost same till σ_∞ = 45 MPa, and then they start diverging. The plastic analysis yields lower values of σ_θ than the elastic analysis and σ_θ reaches a plateau at about 320 MPa (to almost $\sigma_{ys} + (\sigma_{ult} - \sigma_{ys})/3$). The variation of membrane and bending components of hoop stress at θ = 90° and z = 0 are shown in Figure 5.8. Both elastic and elastic-plastic solutions are presented. As stated previously, the elastic and elastic plastic analysis results starts diverging at σ_∞ = 45 MPa.

The plastic membrane stress continue to increase and reaches a plateau. Whereas the stress decreases with σ_∞ and finally reaches almost a zero value. Therefore, we can conclude that the local bending stresses can be neglected at large remote stress.

5.5 Summary

Elastic-plastic analysis of neat fit two-rivet lap joint was conducted. The material was assumed to be multi-linear stress-strain response, Von Mises yielding and isotropic hardening. The incremental elastic-plastic analysis was used. The analysis was carried out to a remote stress of about 100 MPa. Hoop stresses at the critical hole at the joint was examined. The results showed that plastic deformation reduces stress concentration factor from 5.4 to 3.45, the hoop stress at $\theta = 90^\circ$ and $z = 0$ is nearly same as the maximum hoop stress and the bending stress reduce to nearly zero at large plastic deformation at the joint.

Table 5.1. Location of maximum hoop stress in the bottom plate

Remote Stress	Maximum	Coordinates			Stress	%difference
MPa	Hoop stress	r	θ	z	At z=0,θ=90	
3.9	21.4	1.6	90.0	0.0	21.4	0.0
8.3	43.6	1.6	90.0	0.0	43.6	0.0
17.4	90.7	1.6	90.0	0.0	90.7	0.0
26.6	143.8	1.6	90.0	0.0	143.8	0.0
36.1	199.4	1.6	90.0	0.0	199.4	0.0
45.5	252.5	1.6	90.0	0.0	252.5	0.0
50.2	267.6	1.6	75.0	0.0	257.1	4.1
55.1	273.0	1.6	67.5	0.0	271.3	0.7
59.8	279.4	1.6	90.0	0.0	279.4	0.0
64.7	286.7	1.6	75.0	0.0	285.1	0.6
74.3	302.5	1.6	75.0	0.0	300.4	0.7
84.0	318.1	1.6	75.0	0.0	315.5	0.8
90.5	378.6	1.6	90.0	0.0	378.6	0.0
93.3	329.1	1.6	75.0	0.0	325.2	1.2
97.7	330.4	1.6	75.0	0.0	325.7	1.4

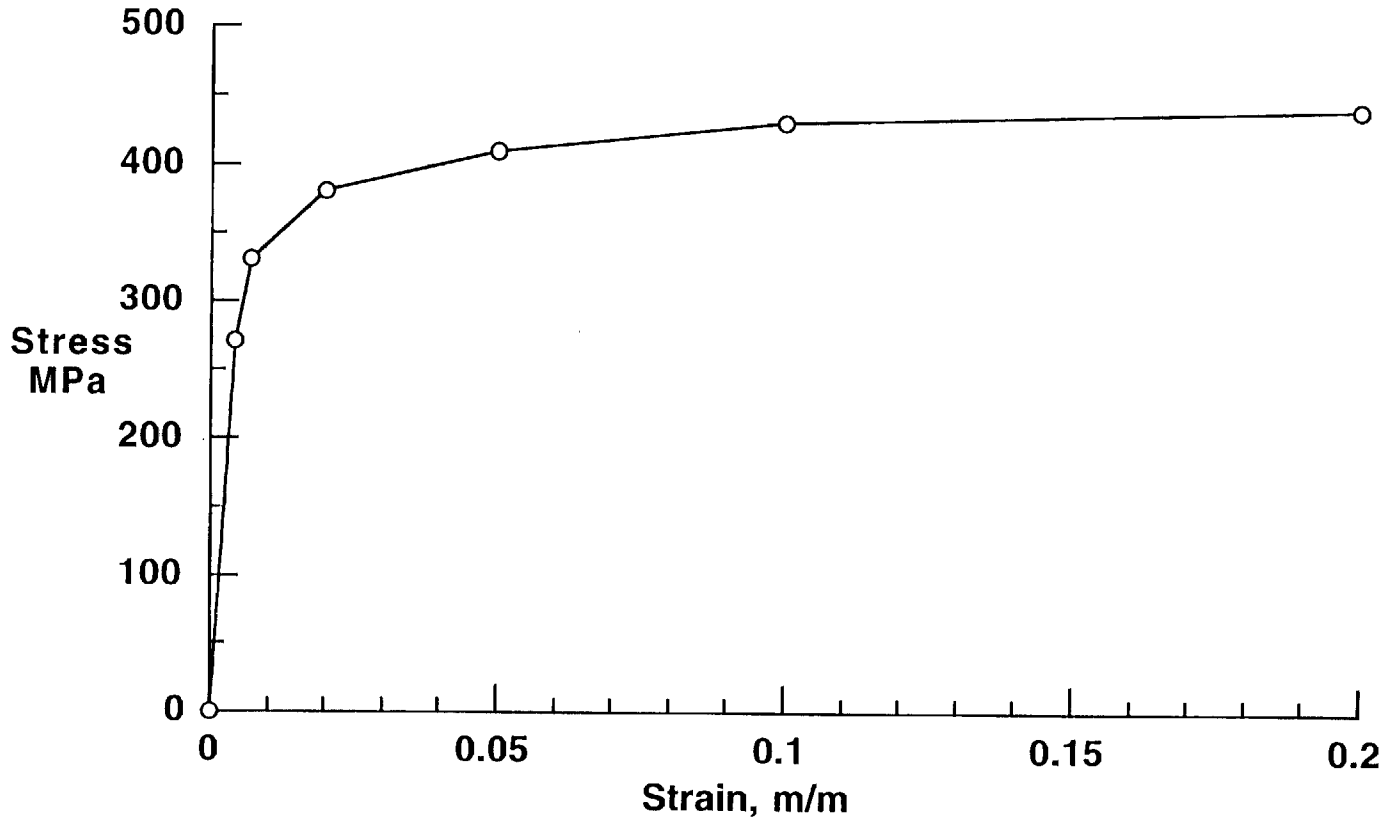

Figure 5.1. Uniaxial stress - strain response of 2024-T3 Alclad aluminum alloy

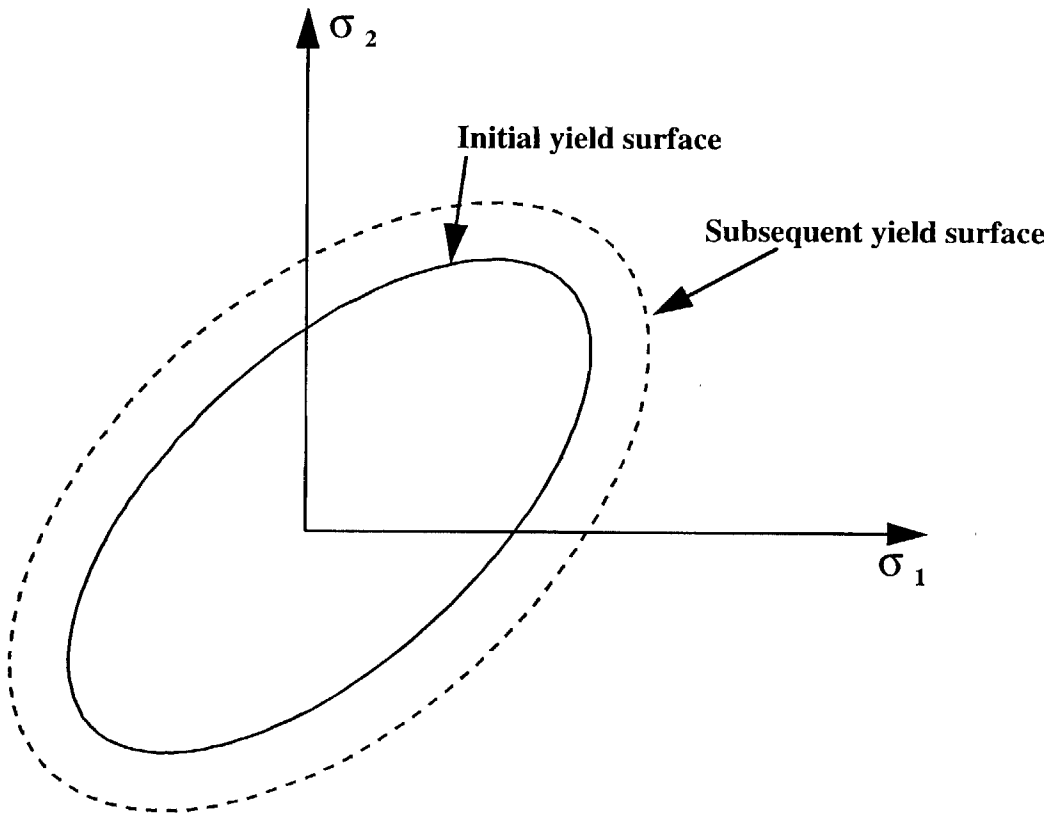

Figure 5.2. Initial and subsequent yield surface for isotropic hardening

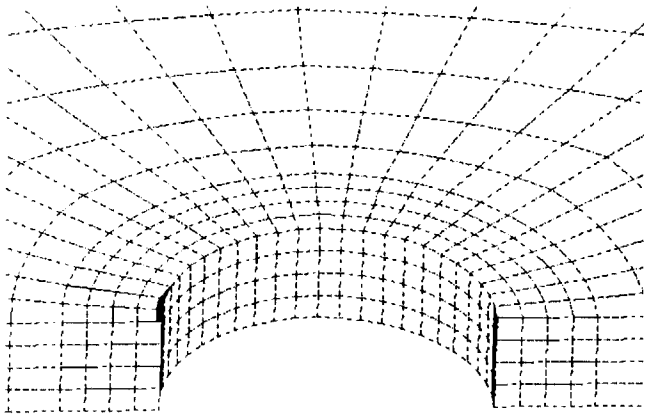

a) UX = 0.1 (45.5 MPa)

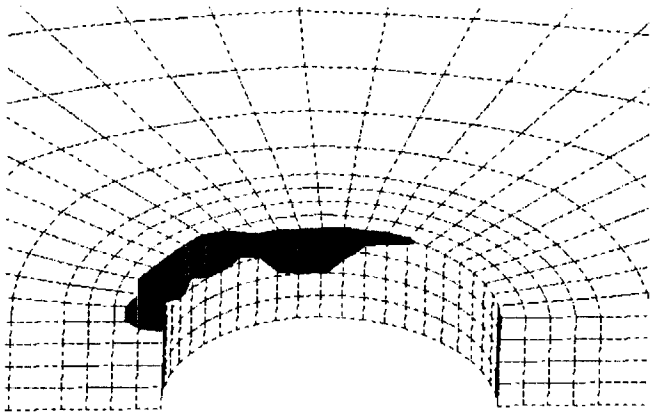

b) UX = 0.12 (55.1 MPa)

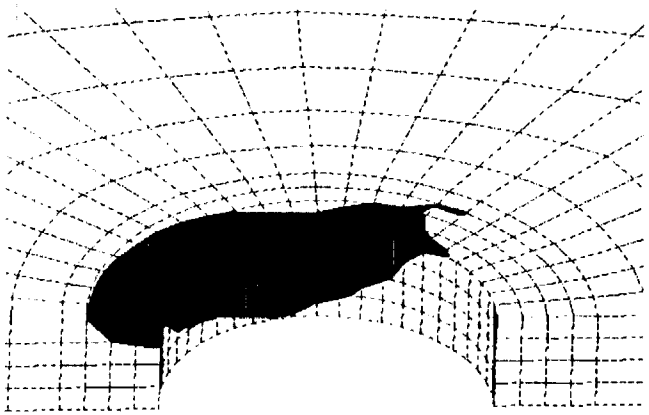

c) UX = 0.16 (74.3 MPa)

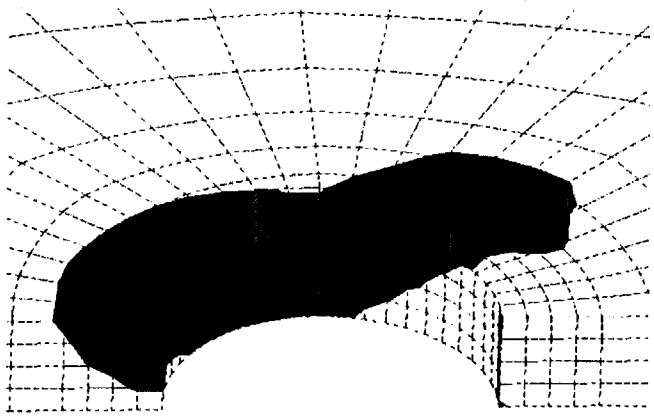

d) UX = 0.21 (97.7 MPa)

Figure 5.3. Progressive plastic - zone with loading in the bottom plate of the joint

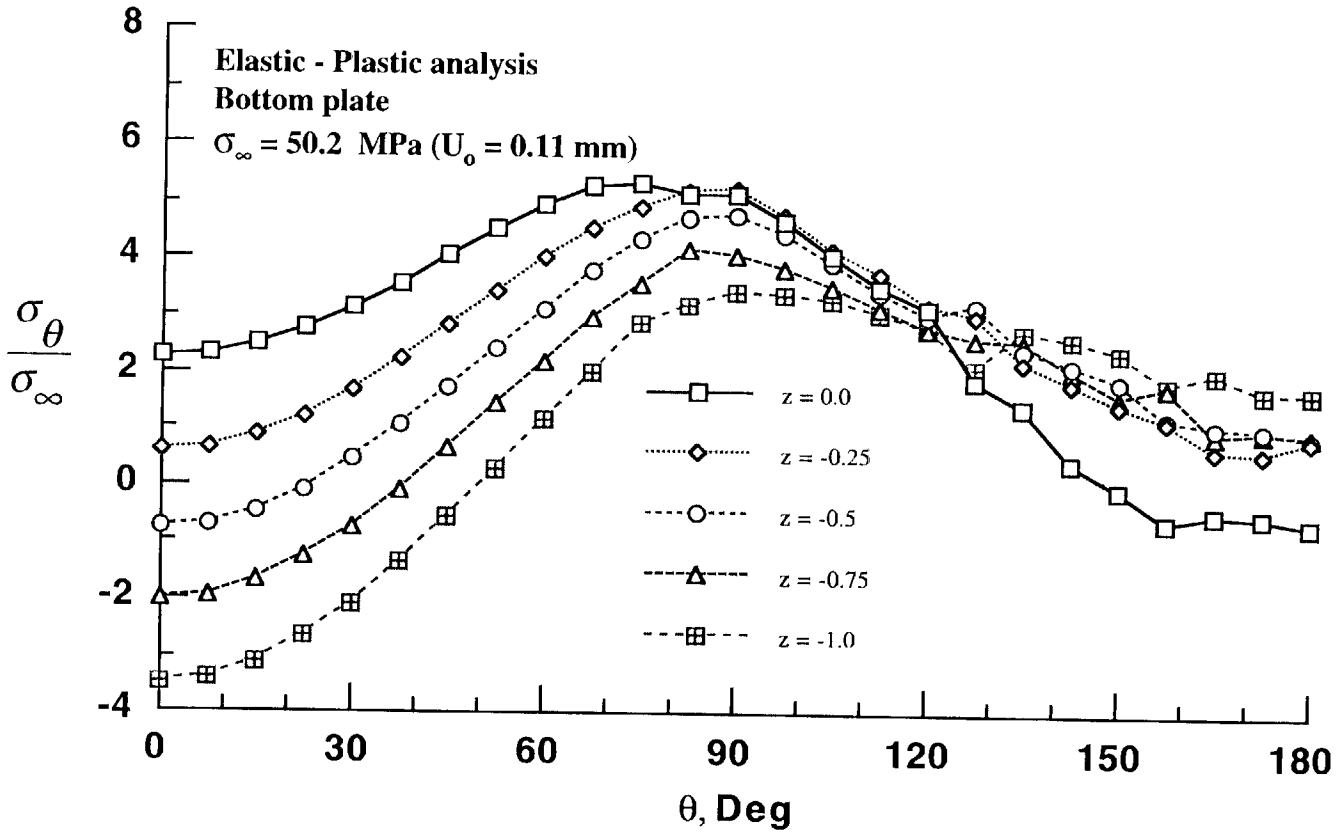

Figure 5.4. Variation of hoop stress along θ in the bottom plate at σ_∞ = 50.2 MPa

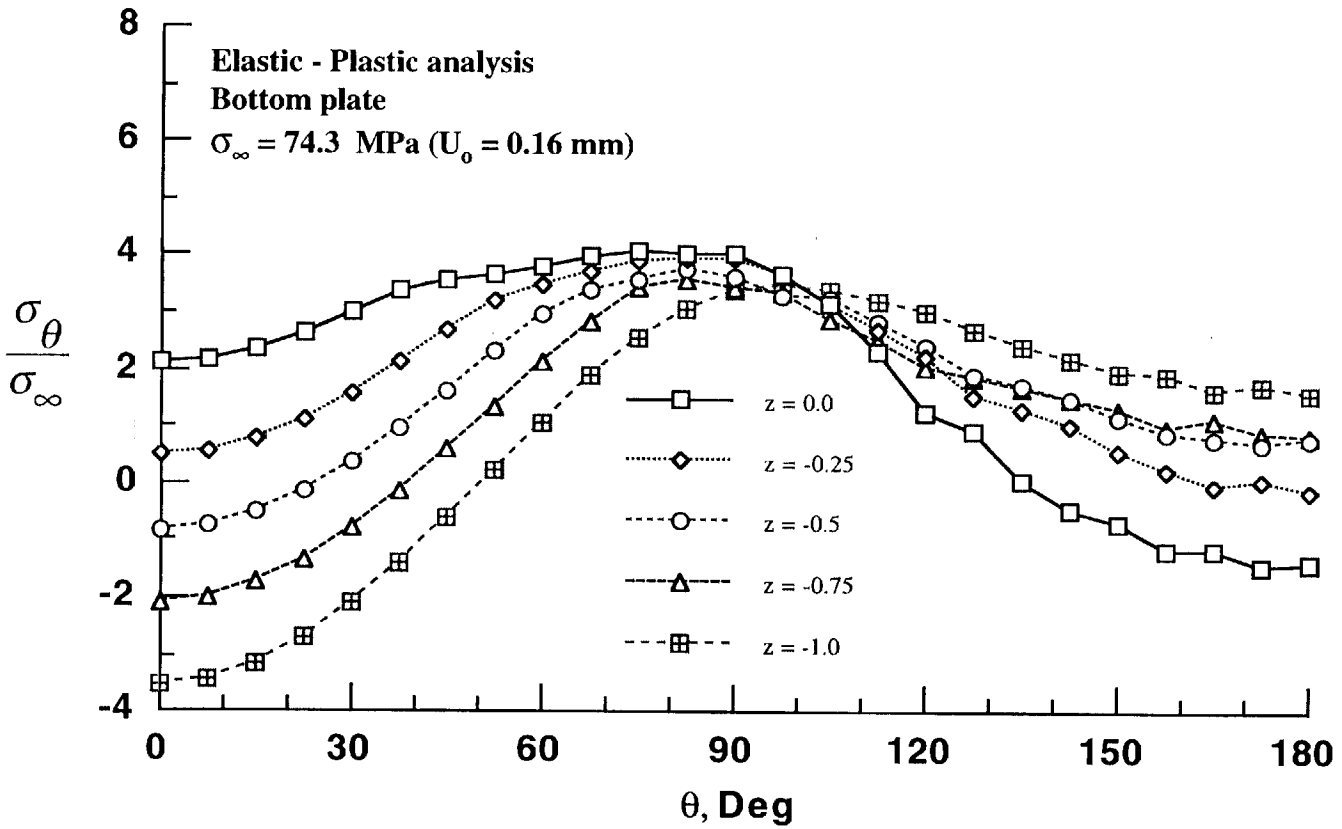

Figure 5.5. Variation of hoop stress along θ in the bottom plate at σ_∞ = 74.3 MPa

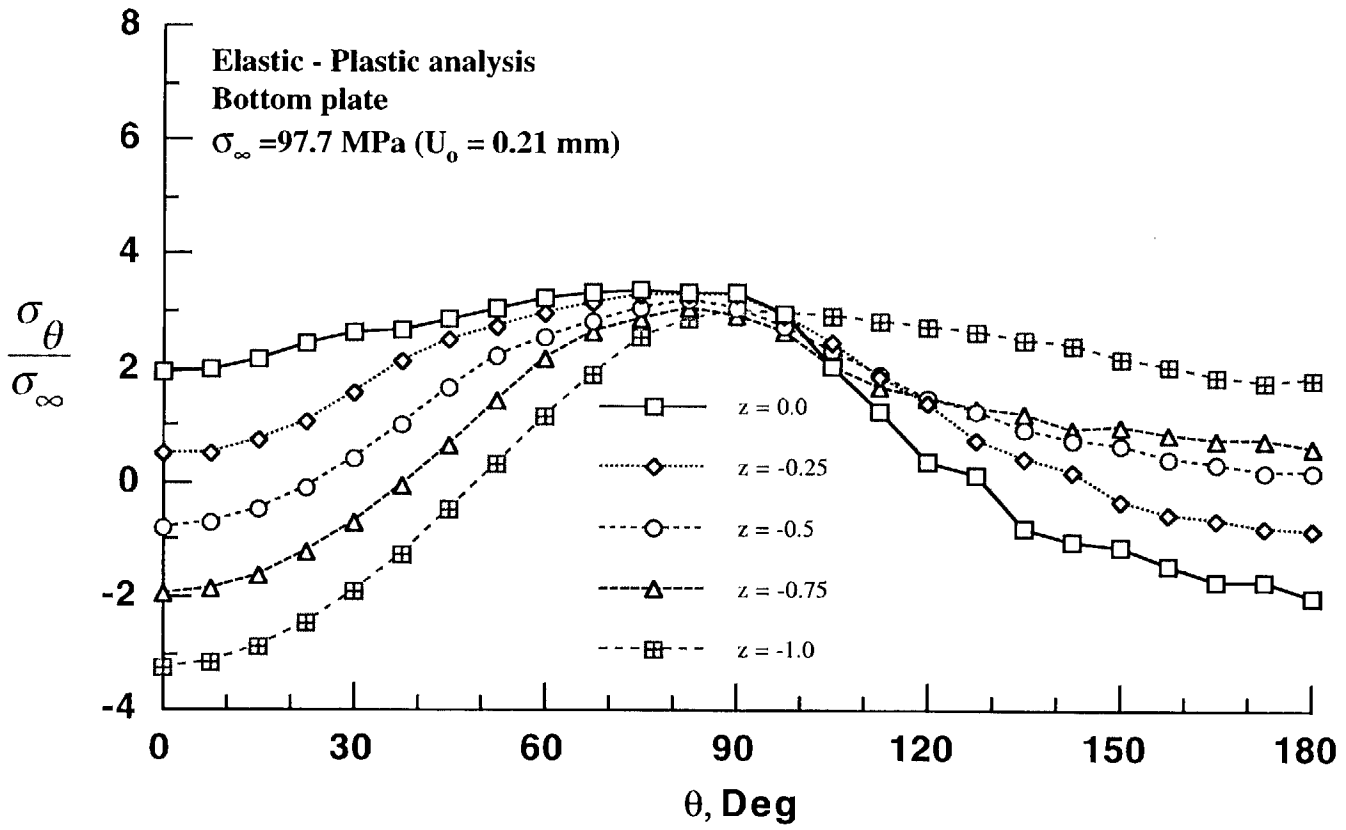

Figure 5.6. Variation of hoop stress along θ in the bottom plate at σ_∞ = 97.7 MPa

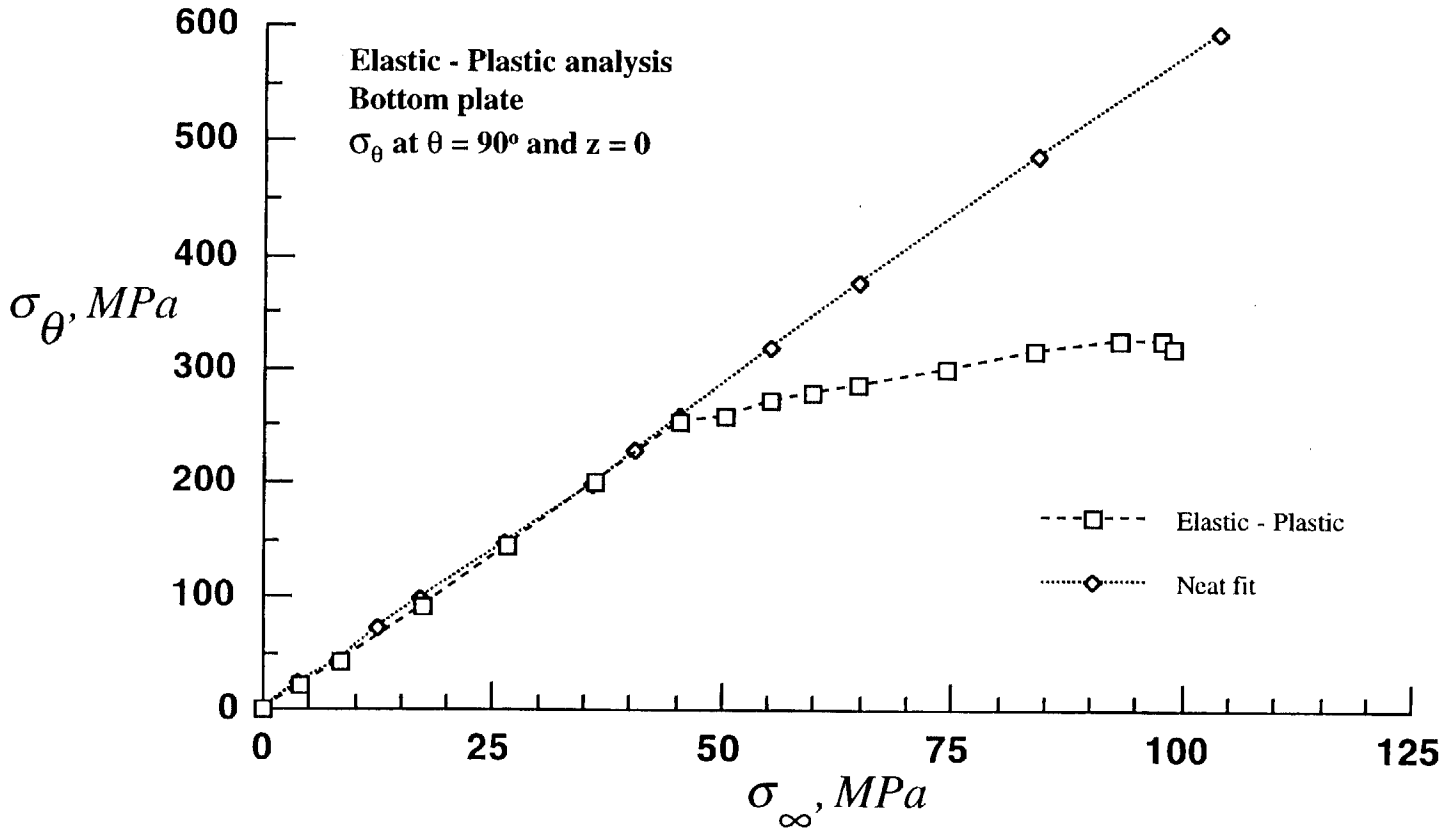

Figure 5.7. Variation of hoop stress at $\theta = 90^o$ with σ_∞

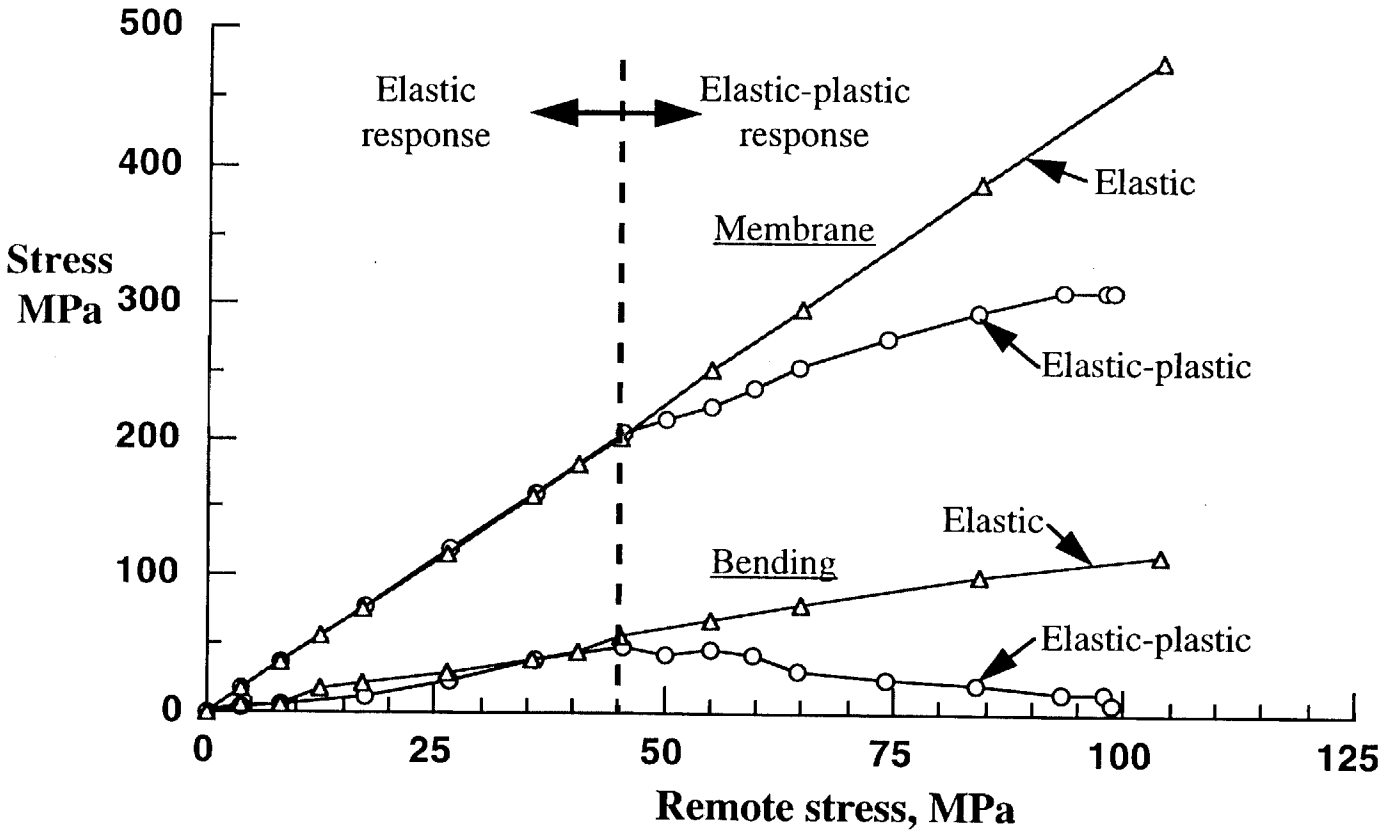

Figure 5.8. Variation of membrane and bending component stresses with remote stress (at $\theta = 90^{o}$ and $z = 0$) in the bottom plate

6. CONCLUDING REMARKS

Conducted a detailed stress analysis of pin joint and two-rivet single lap joint. These joint configurations are representative of lap-splice joints used in aircraft. The lap joint includes the load eccentricity effect where as the pin joint does not include this effect. The analysis included the effect of plate-rivet surface-to-surface friction, rivet clampup, and rivet interference effects. The analysis was conducted using 3-D, 8-noded isoparametric finite elements. The contact was modeled by 5-noded surface-to-surface contact elements. This element had capability of developing contact and separation between predetermined surfaces. Simple rivet contraction and expansion models were developed and used to simulate rivet clampup and interference. The range of clampup force used was 0 to 35% rivet yield load; rivet interference used was 12.5 to 38.1 μm and the friction varied from 0.0 to 0.8. A commercial finite element code was used for the analysis of the joints. Elastic analysis was conducted on the pin joint and elastic and elastic-plastic analysis were conducted on two-rivet single lap joint. The primary focus of results analysis was on hoop and radial contact stresses at the hole boundary. Results of this study yielded following conclusions.

Elastic Analysis of Two-Rivet Joint

Pin Joint

(1) Maximum stress was the hoop stress on the hole boundary and occurred at 90° to the load axis. The hoop stress was maximum at mid-thickness of the plate.

(2) The contact angle was found to be nearly 180^0.

(3) Elastic friction had negligible effect on local stresses (hoop) and hence it can be ignored.

(4) Clampup effect was dominant at low applied loads. Clampup decreases the local hoop stresses. But at high applied loads, clampup effect is small.

(5) Interference was a major factor that impacted the local stresses (hoop stress) around the rivet hole. Interference introduces local tensile hoop stress at the rivet hole. This initial stress reduces the rate of increase of local stresses with remote loads. This causes the local hoop stresses to be lower than the neat fit results at high load levels.

(6) Contact, friction and rivet clampup nonlinearities were confined to low axial loads. At high loads, the response is nearly linear.

Two-Rivet Lap Joint

(1) For the neat fit case hoop stress on the hole boundary was the highest and it occurred in the bottom plate at the interface between the top and bottom plates at 90° to the load axis. The maximum stress concentration factor was found to be 5.7. Contact nonlinearity was confined to low levels of applied load (σ_∞.< 30 MPa). At higher applied loads the response is almost linear. The radial stress distribution on the hole boundary can be represented by a cosine function of type $\frac{\sigma_r}{\sigma_\infty} = a\cos^n\theta$. Values of 'a' and 'n' depend on the through the thickness location on the hole boundary.

(3) Elastic friction has negligible effect on local stresses (hoop) and hence it can be ignored.

(4) For the clampup case, again the maximum stresses occurred on the hole boundary and in the bottom plate. The clampup force did decrease the

stresses at the critical location and its effect can be summarized in the form of a simple linear equation. For 10% clampup level, maximum hoop stress location changed from 75° at low load levels to 90° for high load levels. But for 25% and 35% clampup it remains at 75° for almost all load levels. The Clampup effect was confined to the region under the rivet head. Beyond the rivet head it's effects were significantly reduced.

(5) Interference is major factor that impacts the local stresses (hoop stress) around the rivet hole. Interference reduces the rate of increase of local stresses with remote loads. This causes the local (hoop) stresses to be lower than the neat fit results at high load levels.

Elastic-Plastic Analysis of Two-Rivet Joint

Elastic-plastic analysis of neat fit two-rivet lap joint was conducted. The material was assumed to be multi-linear stress-strain response, Von Mises yielding and isotropic hardening. The incremental elastic-plastic analysis was conducted to a remote stress of about 100 MPa. Hoop stresses at the critical hole at the joint was examined. The results showed that plastic deformation reduces stress concentration factor from 5.4 to 3.45, the hoop stress at $\theta = 90°$ and $z = 0$ is nearly same as the maximum hoop stress and the bending stress reduce to nearly zero at large plastic deformation at the joint.